THE UNIVERSITY *of* EDINBURGH

Modelling Uncertainties for Measurements of the $H \to \gamma\gamma$ Channel with the ATLAS Detector at the LHC

Matthew Peter Heath

Doctor of Philosophy
The University of Edinburgh
February 2022

Abstract

The Higgs boson to diphoton ($H \to \gamma\gamma$) branching ratio is only 0.227 %, but this final state has yielded some of the most precise measurements of the particle. As measurements of the Higgs boson become increasingly precise, greater import is placed on the factors that constitute the uncertainty. Reducing the effects of these uncertainties requires an understanding of their causes. The research presented in this thesis aims to illuminate how uncertainties on simulation modelling are determined and proffers novel techniques in deriving them.

The upgrade of the FastCaloSim tool is described, used for simulating events in the ATLAS calorimeter at a rate far exceeding the nominal detector simulation, Geant4. The integration of a method that allows the toolbox to emulate the accordion geometry of the liquid argon calorimeters is detailed. This tool allows for the production of larger samples while using significantly fewer computing resources.

A measurement of the total Higgs boson production cross-section multiplied by the diphoton branching ratio ($\sigma \times B_{\gamma\gamma}$) is presented, where this value was determined to be $(\sigma \times B_{\gamma\gamma})_{\text{obs}} = 127 \pm 7$ (stat.) ± 7 (syst.) fb, within agreement with the Standard Model prediction. The signal and background shape modelling is described, and the contribution of the background modelling uncertainty to the total uncertainty ranges from 18–2.4 %, depending on the Higgs boson production mechanism.

A method for estimating the number of events in a Monte Carlo background sample required to model the shape is detailed. It was found that the size of the nominal $\gamma\gamma$ background events sample required a multiplicative increase by a factor of 3.60 to adequately model the background with a confidence level of 68 %, or a factor of 7.20 for a confidence level of 95 %. Based on this estimate, 0.5 billion additional simulated events were produced, substantially reducing the

background modelling uncertainty.

A technique is detailed for emulating the effects of Monte Carlo event generator differences using multivariate reweighting. The technique is used to estimate the event generator uncertainty on the signal modelling of $tHqb$ events, improving the reliability of estimating the $tHqb$ production cross-section. Then this multivariate reweighting technique is used to estimate the generator modelling uncertainties on background $V\gamma\gamma$ samples for the first time. The estimated uncertainties were found to be covered by the currently assumed background modelling uncertainty.

Lay Summary

The best description of the fundamental interactions between matter and energy that we currently have is given by a theory called the Standard Model (SM). It can give extremely accurate predictions of nature on the subatomic scale by describing matter and forces as the exchange of different particles. Until 2012, all of the fundamental particles predicted by the SM had been proven to exist other than the Higgs boson; and with its discovery, the Standard Model is considered complete. However, there are known phenomena that the theory still cannot predict and searches are ongoing for measurements of Standard Model processes that fail to match the theory so that we can focus on where it does not hold up.

The Large Hadron Collider (LHC) is the largest particle accelerator ever created and was built for the purpose of probing Standard Model interactions. It collides protons at extremely high energies in a 27 km circumference tunnel, providing the conditions necessary to produce interactions and particles that cannot be found in the usual matter of the world around us. ATLAS is one of four main detectors that are used to observe the effects of these high energy particle collisions at the LHC, and it provides the information necessary to make measurements of their properties. It was from efforts made at ATLAS and another detector called CMS that conclusive evidence of the existence of the Higgs boson was obtained.

The Higgs boson is an important part of the search for failing predictions by the SM, or what is often called 'new physics'. As a recently discovered particle, it has offered many opportunities to measure its properties and assess their agreement with the Standard Model. The Higgs boson has a short lifetime and is studied by the particles into which it decays, allowing us to reconstruct it from these longer lifetime particles that we can detect. One of the cleanest signatures of Higgs decay products that ATLAS can observe is when it decays into two photons, the particles that govern the behaviour of light. In the time since 2012, the precision of Higgs boson measurements via this decay process has become very high but

no diversions from the SM predictions have been observed. This thesis focusses on how the precision can be improved even further, and how we might better understand what causes the uncertainties on these measurements.

To create a representation of how we expect measurements of the Standard Model Higgs boson should look when it decays to two photons, computers are used to simulate how the particle collisions that produce such events would occur in the ATLAS detector. These simulated samples are crucial in testing any differences, and require enough events to match the real data that is produced by the LHC for testing. The first contribution described by this research is in the development of techniques that allow for the faster production of simulated events to keep up with the increasing rate at which the LHC creates data.

A new method is then demonstrated that estimates how many simulated events would be required to create adequate models of Standard Model processes for Higgs bosons decaying to two photons. It is important to obtain a reliable estimate of how many events are needed since it requires a lot of computing resources to produce large amounts of simulation. Based on the results of this method, an extra 500 million events were produced, which substantially reduced the measurement uncertainty.

Finally a technique is presented that allows the effects of different simulation production methods on the measurement to be determined. As the Standard Model is mathematically complex, there are no explicit solutions that can calculate the exact nature of some processes. Different simulation methods use different ways to best approximate these that must all be regarded as true. Additionally, there is increasing stress on computing resources to generate simulated samples that can match the amount of real data that the LHC produces. This means that significant sets of simulation events using the alternate methods cannot be made sometimes, making it hard to judge how much the different simulation methods can affect the end result. The new technique allows one sample of simulation to be made to look like a different one, and does not require the production of extra samples. The technique is used to look at the difference in simulation production for two different aspects of the Higgs to two photons measurement, but does not find any effects that are not accounted for by the current measurement errors. However, as these current errors will improve in the future, the importance of those effects will come to the forefront.

Declaration

The data presented in this thesis were obtained in an experiment carried out by the ATLAS Collaboration at CERN in Geneva, Switzerland. I played a major role in the preparation and execution of the experiment, and the data analysis and interpretation are entirely my own work. Any contributions from colleagues in the collaboration, such as diagrams or calibrations, are explicitly referenced in the text.

I am aware of and understand the university's policy on plagiarism and I certify that this thesis is my own work, except where indicated by referencing. The work presented herein has not been submitted in support of another degree or qualification from this or any other institute of learning.

(*Matthew Peter Heath, February 2022*)

Acknowledgements

There are many people I would like to thank for their guidance and support over these last five years.

Firstly, I give thanks to the ATLAS and LHC groups for providing the data and simulation upon which this research was built. There are uncountably many scientists, innovators, and thinkers who came before me, and without them it would have been impossible to produce this work.

I would like to show my appreciation for my supervisor, Philip Clark, for all his encouragement over the course of my degree. He has taught me a great deal and has been extremely understanding, his faith in my abilities has kept me going throughout the years.

This thesis would not exist without the aid of Liza Mijović. Her explanations have been invaluable to me, and the amount of time and effort she has lent in helping to review my work has been staggering. I wish her all the best in her career, despite also distracting me with Monty Python sketches during writing.

I would like to thank Hasib Ahmed for introducing me to the FastCaloSim project and for getting me started on ATLAS research.

To all of the members of the Edinburgh PPE Group and those on LTA at CERN, thank you for making me feel welcome. The experience would not have been the same without you all. For the remaining PhD students, good luck with your degrees.

I wish to extend my special thanks to the Bridge Boys, the expertise of this group of young men on such a wide range of topics is astounding. I cherish the ridiculous discussions, advice, games, and support you have all provided me with.

To my parents and to Becky, thank you for everything. Words are not enough to express the opportunities I have had because of your help and encouragement. I hope I have made you proud.

Lastly, but not least, I want to thank Salomé. You have been so supportive of me over the last few years and I want you to know how much I appreciate you. I am looking forward to everything the future has in store for us.

In loving memory of
Sally, Noreen, Andrew, and Martin.
I miss you all dearly.

Contents

Chapter 1

Introduction

Measuring the properties of the Higgs boson discovered by the ATLAS and CMS experiments [1, 2] is not only critical for elucidating the mechanism of electroweak symmetry breaking [3–5] but also to provide constraints on physics beyond the Standard Model. Despite a small Higgs boson to diphoton ($H \to \gamma\gamma$) branching ratio of about 0.227 % [6], measurements in the diphoton final state have yielded some of the most precise determinations of Higgs boson properties due to the excellent performance of photon reconstruction and identification with the ATLAS detector.

The signature of the Higgs boson in the diphoton final state is a narrow resonance with a width characterised by the resolution of the detectors measuring the photon properties, rising above a smooth background in the diphoton invariant mass ($m_{\gamma\gamma}$) distribution. The mass and event rate of the Higgs boson signal can thus be extracted through fits of the $m_{\gamma\gamma}$ distribution. Properties of the Higgs boson have been studied extensively in the diphoton final state, and the Higgs boson production cross-section has been measured with an unprecedented precision of 8 %. No significant deviation from the Standard Model prediction has been observed.

As measurements of the Higgs boson become ever more precise, greater import is placed on contributions of different factors that constitute the uncertainty. Reducing the effects of systematic uncertainties for each measurement iteration requires a comprehensive understanding of their causes. For the $H \to \gamma\gamma$ channel, the modelling of signal and background shapes in the $m_{\gamma\gamma}$ spectrum is the source of some of the largest systematic uncertainties in the measurement. The research

presented in this thesis aims to illuminate how these shapes are modelled, how the uncertainties on the modelling are determined, and proffers novel techniques in deriving these uncertainties.

Chapter 2 will introduce the Standard Model of particle physics. Here, the fundamentals of the current most comprehensive theory describing interactions between matter and energy is presented. This sets the scene for the measurements described in this thesis, and introduces the various particles and forces that govern the physics models that they test.

In Chapter 3, a description is given of the infrastructure and hardware applied to obtain data used in this thesis. Namely, these are the Large Hadron Collider which accelerates the initial protons to the energies required for the study of their collision products, and the ATLAS detector which records the signatures that characterise the results of these collisions. Here it is explained how one may glean meaningful information from effects too miniscule to affect anything perceived at the human scale.

The generation of Monte Carlo simulated samples is critical to forming the background and signal distributions that must be modelled to perform the $H \to \gamma\gamma$ measurement. For these samples, the statistical significance plays a large role in how confidently the shape modelling can be performed. As a result, Chapter 4 explains how events are simulated at the ATLAS experiment, while Chapter 5 details an upgrade of FastCaloSim. This latter tool is implemented to simulate events in the ATLAS calorimeter at a rate far exceeding the nominal detector simulation, Geant4, allowing for production of larger samples while using significantly fewer computing resources. Here it is explained how the simplified calorimeter geometry employed by the toolkit to speed up simulation failed to reproduce effects caused by the complex accordion structure of the liquid argon detectors. A solution is presented and its integration with the FastCaloSim upgrade is illustrated.

The measurement of the total Higgs boson production cross-section multiplied by the diphoton branching ratio ($\sigma \times B_{\gamma\gamma}$) is presented in Chapter 6. The methods for modelling the signal and background shapes in the $m_{\gamma\gamma}$ spectrum are also described, and the contribution of the background modelling uncertainty is presented to provide context for the ensuing research contributions.

A new method for estimating the number of events comprising a Monte Carlo background sample required to adequately model the shape is detailed in

Chapter 7. Based on the results obtained with this method, the resources for the production of 0.5 billion additional simulated events were allocated, substantially reducing the background modelling uncertainty.

Finally, a technique is detailed in Chapter 8 for emulating the effects of Monte Carlo event generator differences using multivariate reweighting. Such emulation enables uncertainty estimates without the overhead of producing dedicated simulation samples. The technique is initially used in Chapter 9 to estimate the event generator uncertainty on the signal modelling of $tHqb$ events. The knowledge of this generator uncertainty improves the reliability of estimating the $tHqb$ production cross-section. Subsequently, this multivariate reweighting technique is used in Chapter 10 to estimate the generator modelling uncertainties on background $V\gamma\gamma$ events for the first time. Chapter 11 then summarises the main findings of this research and concludes the thesis.

References

[1] The ATLAS Collaboration. 'Observation of a new particle in the search for the Standard Model Higgs boson with the ATLAS detector at the LHC'. In: *Physics Letters B* 716.1 (Nov. 2012), pp. 1–29. ISSN: 0370-2693. DOI: 10.1016/j.physletb.2012.08.020.

[2] The CMS Collaboration. 'Observation of a new boson at a mass of 125 GeV with the CMS experiment at the LHC'. In: *Physics Letters B* 716.1 (Sept. 2012), pp. 30–61. ISSN: 0370-2693. DOI: 10.1016/j.physletb.2012.08.021.

[3] F. Englert and R. Brout. 'Broken Symmetry and the Mass of Gauge Vector Mesons'. In: *Phys. Rev. Lett.* 13 (9 Aug. 1964), pp. 321–323. DOI: 10.1103/PhysRevLett.13.321.

[4] Peter W. Higgs. 'Broken Symmetries and the Masses of Gauge Bosons'. In: *Phys. Rev. Lett.* 13 (16 Oct. 1964), pp. 508–509. DOI: 10.1103/PhysRevLett.13.508.

[5] G. S. Guralnik, C. R. Hagen and T. W. B. Kibble. 'Global Conservation Laws and Massless Particles'. In: *Phys. Rev. Lett.* 13 (20 Nov. 1964), pp. 585–587. DOI: 10.1103/PhysRevLett.13.585.

[6] D. de Florian et al. *Handbook of LHC Higgs Cross Sections: 4. Deciphering the Nature of the Higgs Sector*. CERN Yellow Reports: Monographs CERN-2017-002-M. Oct. 2016. DOI: 10.23731/CYRM-2017-002.

Part I

Motivation and Tools

Chapter 2

The Standard Model of Particle Physics

The *Standard Model* (SM) of particle physics is the best description we currently have for the fundamental interactions between matter and energy, incorporating three of the four known fundamental forces into a comprehensive *quantum field theory* (QFT). The model combines the QFT for strong interactions, *Quantum Chromodynamics* (QCD), with the *electroweak* (EW) force. This latter force is itself the unification of the QFTs for electromagnetic and weak interactions, known as *Quantum Electrodynamics* (QED) and *Quantum Flavourdynamics* (QFD) respectively.

Particles in a QFT are described by local fields, $\psi(x)$, valued over space-time, x. The dynamics of these fields are contained within the Lagrangian density of the system, $\mathcal{L}(\psi, \partial_\mu \psi)$. Each local continuous transformation of $\psi(x)$ forms a continuous group of QFT, providing the action,

$$S = \int d^4x \mathcal{L}(\psi, \partial_\mu \psi), \tag{2.1}$$

remains unchanged ($\delta S = 0$) under the transformation. These gauge groups are constructed to reflect the observed symmetries in nature. Due to each continuous symmetry of the SM Lagrangian density resulting in a conserved current of charge (as dictated by Noether's first theorem), the symmetries of nature are accounted for by symmetries of $\mathcal{L}$ under field transformation operators. As an example, the

conservation of electric charge current in all interactions can be represented by the invariance of $\mathcal{L}$ under unitary gauge transformation operator $(\mathrm{U}) : \psi(x) \rightarrow \mathrm{U}\psi(x)$. Such theories that are based on the concept of gauge invariance are called 'gauge theories', and are termed 'abelian' if the gauge transformations are commutative or 'non-abelian' if they are not.

As the combination of QCD and EW theory, the SM Lagrangian density can be expressed as the sum of the Lagrangian densities of these two QFTs,

$$\mathcal{L}_{\mathrm{SM}} = \mathcal{L}_{\mathrm{QCD}} + \mathcal{L}_{\mathrm{EW}}. \tag{2.2}$$

The conserved currents of interactions described by the Standard Model are represented by the local invariance of Equation 2.2 under gauge transformation operators belonging to the symmetry group

$$\mathrm{SU}(3) \otimes \mathrm{SU}(2) \otimes \mathrm{U}(1). \tag{2.3}$$

Here SU(3) is the third-degree special unitary group and the invariance to gauge transformations belonging to this group addresses the conservation of *colour* charge in QCD. SU(2) is the second-degree special unitary group referring to *weak isospin* charge conservation, and U(1) is the first-degree unitary group corresponding to the conservation of *weak hypercharge*. The invariance of the Standard Model Lagrangian density to gauge transformations belonging to the $\mathrm{SU}(2) \otimes \mathrm{U}(1)$ group arises from electroweak interactions.

2.1 Quantum Electrodynamics

Quantum Electrodynamics describes the interactions between matter and photons via the electromagnetic force and is represented as an abelian gauge theory. Matter is composed of spin-½ particles that obey the Pauli exclusion principle, known as fermions. These fermions are represented as a four-component spinor field, $\psi(x)$, with each component being a function of space-time, x. A free fermion has an equation of motion described by the Dirac equation,

$$(i\gamma^{\mu}\partial_{\mu} - m)\psi = 0, \tag{2.4}$$

where m is the mass of the fermion, and γ^μ are the Dirac matrices

$$\begin{aligned}\gamma^0 &= \begin{pmatrix} 1 & 0 & 0 & 0 \\ 0 & 1 & 0 & 0 \\ 0 & 0 & -1 & 0 \\ 0 & 0 & 0 & -1 \end{pmatrix}, \gamma^1 = \begin{pmatrix} 0 & 0 & 0 & 1 \\ 0 & 0 & 1 & 0 \\ 0 & -1 & 0 & 0 \\ -1 & 0 & 0 & 0 \end{pmatrix}, \\ \gamma^2 &= \begin{pmatrix} 0 & 0 & 0 & -i \\ 0 & 0 & i & 0 \\ 0 & i & 0 & 0 \\ -i & 0 & 0 & 0 \end{pmatrix}, \gamma^3 = \begin{pmatrix} 0 & 0 & 1 & 0 \\ 0 & 0 & 0 & -1 \\ -1 & 0 & 0 & 0 \\ 0 & 1 & 0 & 0 \end{pmatrix}.\end{aligned} \tag{2.5}$$

The Lagrangian density resulting in the free-particle Dirac equation as the equation of motion is given as

$$\mathcal{L} = i\bar{\psi}\gamma^\mu\partial_\mu\psi - m\bar{\psi}\psi \tag{2.6}$$

where $\bar{\psi}$ is the adjoint fermion spinor, defined by $\bar{\psi} = \psi^\dagger\gamma^0$.

The requirement of gauge invariance is used to describe interactions between particles. To be gauge invariant, the equation of motion should not change under local phase transformations of the field, and the Lagrangian density must not be modified by more than a total derivative. However, when applying a local phase transformation belonging to U(1) of $\psi \to \psi' = e^{i\theta(x)}\psi(x)$, where $\theta(x)$ is an arbitrary function of x, the first term of the Lagrangian density transforms as

$$\begin{aligned} i\bar{\psi}'\gamma^\mu\partial_\mu\psi' &= i\bar{\psi}e^{-i\theta}\gamma^\mu\partial_\mu[e^{i\theta}\psi] \\ &= i\bar{\psi}\gamma^\mu\partial_\mu\psi - i\bar{\psi}\gamma^\mu\psi[\partial_\mu\theta]. \end{aligned} \tag{2.7}$$

Here gauge invariance is not achieved due to the $[\partial_\mu\theta]$ term. To rectify this, a massless spin-1 vector boson field, $A_\mu(x)$, is introduced. This field transforms as $A_\mu \to A'_\mu = A_\mu(x) - \frac{1}{Q}\partial_\mu\theta(x)$ under the same transformations belonging to the U(1) symmetry group, where Q is a constant. This A_μ field transformation cancels with the $\partial_\mu\theta$ term from Equation 2.7 to achieve the required invariance. The gauge covariant derivative, $D_\mu(x)$, defined by

$$D_\mu \psi = [\partial_\mu + iQA_\mu]\psi \tag{2.8}$$

can now substitute for ∂_μ in the Lagrangian density to give

$$\begin{aligned} \mathcal{L} &= i\bar{\psi}\gamma^\mu D_\mu \psi - m\bar{\psi}\psi \\ &= i\bar{\psi}\gamma^\mu \partial_\mu \psi - q\bar{\psi}\gamma^\mu A_\mu \psi - m\bar{\psi}\psi. \end{aligned} \tag{2.9}$$

Finally, to complete the picture, the dynamics of A_μ are introduced by the addition of the kinetic term $-\frac{1}{4}F^{\mu\nu}F_{\mu\nu}$ to the Lagrangian density. $F_{\mu\nu}$ is the electromagnetic field strength tensor, defined as $F_{\mu\nu} = \partial_\mu A_\nu - \partial_\nu A_\mu$. The complete QED Lagrangian density is thus given by

$$\begin{aligned} \mathcal{L}_{\text{QED}} &= -\frac{1}{4}F^{\mu\nu}F_{\mu\nu} + \bar{\psi}(i\gamma^\mu D_\mu - m)\psi \\ &= -\frac{1}{4}F^{\mu\nu}F_{\mu\nu} + \bar{\psi}(i\gamma^\mu \partial_\mu - m)\psi - Q\bar{\psi}\gamma^\mu A_\mu \psi. \end{aligned} \tag{2.10}$$

Explicitly, the first term in Equation 2.10 represents the Lagrangian density for Maxwell's equations in the absence of any sources, while the second term represents a free fermion. The third term is what emerged from the requirement of gauge invariance and represents a fermion with an electric charge, Q, interacting with the electromagnetic potential, A_μ, via quanta of this massless spin-1 vector boson field known as photons. This recipe illustrates how invariance with respect to specific gauge transformations introduces interaction terms between fields that describe the associations of forces and matter.

2.2 Quantum Chromodynamics

The theory of Quantum Chromodynamics describes the strong interactions between quarks and gluons. It is a non-abelian gauge theory regarding spin-½ fermionic quarks represented by the quark field, $q_f(x)$, of flavour, f. In addition to electric charge allowing interactions via the electromagnetic force, quarks also possess a colour quantum number that serves as the conserved charge of the

strong interaction that arises from the requirement of gauge invariance for QCD. The possible values of this colour charge are nominally red (r), blue (b), and green (g), whilst antiquarks are coloured with corresponding anti-colours ($\bar{r}$, $\bar{b}$, and $\bar{g}$). The Lagrangian density of a free quark is given as

$$\mathcal{L} = \sum_f \bar{q}_f (i\gamma^\mu \partial_\mu - m_f) q_f. \tag{2.11}$$

As before, we then describe interactions by invoking the principles of gauge invariance under SU(3) symmetry in this case. This requires the introduction of a vector field, G^a_μ, representing spin-1 bosons called gluons, and results in the QCD Lagrangian density:

$$\mathcal{L}_{\text{QCD}} = \sum_f \bar{q}_f (i\gamma^\mu \partial_\mu - m_f) q_f - g_s G^\mu_a \sum_f \bar{q}^\alpha_f \gamma_\mu \left(\frac{\lambda^a}{2}\right)_{\alpha\beta} q^\beta_f - \frac{1}{4} G^{\mu\nu}_a G^a_{\mu\nu}. \tag{2.12}$$

$G^{\mu\nu}_a = \partial^\mu G^\nu_a - \partial^\nu G^\mu_a - g_s f^{abc} G^\mu_b G^\nu_c$ is the gluon field strength tensor with f^{abc} being the SU(3) structure constants, and g_s is the strength of the interaction that is universal for all quark flavours. Additionally, α and β label the quark colours, while λ^a represents the eight Gell-Mann matrix generators of SU(3) that result in eight gluon colour states.

The invariance of the Lagrangian density in Equation 2.12 is in respect to local SU(3) transformations of

$$\begin{aligned} q(x) \to \mathrm{U}(x) q(x) &= e^{-ig\alpha^a(x)\frac{\lambda^a}{2}} q(x), \\ G^a_\mu \to G'^a_\mu &= G^a_\mu - \frac{1}{g}\partial_\mu \alpha^a - f^{abc}\alpha^b G^c_\mu, \end{aligned} \tag{2.13}$$

where $\alpha^a(x)$ are arbitrary functions.

The first term of Equation 2.12 again represents the dynamics of free quark fields and the second term is interpreted as the interaction between quarks and the gluon field. The third term is the gluon kinetic term, which, unlike in QED, also gives rise to the gauge bosons self-interacting due to gluons also carrying colour charge. This self-interaction manifests as three- and four-gluon vertices.

Another feature of QCD is known as *asymptotic freedom*, a phenomenon where quarks interact relatively weakly at high energies or short distances, allowing perturbative calculations; but strongly at low energies and larger length scales, leading to quark confinement within composite hadronic bound states.

2.3 Electroweak Interactions

Weak interactions are defined by the emission and absorption of the weak bosons. These are either flavour-changing charged-current interactions that are mediated by $W^{\pm}$ bosons, or neutral-current interactions that are mediated by Z^0 bosons and do not allow changes of flavour at the tree level.

In the Standard Model, the weak and electromagnetic interactions are unified by a gauge theory characterised by symmetries under local phase transformations belonging to the $\mathrm{SU}(2)_L \otimes \mathrm{U}(1)_Y$ symmetry group. This unified electroweak theory results in two further quantum numbers associated with each fermion: weak isospin, T, is the resulting conserved Noether charge of the $\mathrm{SU}(2)_L$ group and hypercharge, Y, is introduced by the $\mathrm{U}(1)_Y$ symmetry group. Hypercharge is related to the electric charge, Q, and to the weak isospin of a particle by

$$Q = T_3 + \frac{Y}{2}, \tag{2.14}$$

where T_3 is the third component of weak isospin. Excepting gluons, all particles in the Standard Model possess a non-zero hypercharge and thus can experience the electroweak force.

Only left-handed chiral state fermions and right-handed chiral state anti-fermions can interact via the weak force. These left- and right-handed fermion fields (ψ_L and ψ_R respectively) are defined as

$$\begin{aligned} \psi_L &= P_L\psi = \frac{1-\gamma^5}{2}\psi, \\ \psi_R &= P_R\psi = \frac{1+\gamma^5}{2}\psi, \end{aligned} \tag{2.15}$$

where $P_{L,R}$ are the respective left- and right-handed projection operators, and

$\gamma^5 = i\gamma^0\gamma^1\gamma^2\gamma^3$ is the product of the four Dirac matrices. For massless particles and for fermions approaching the speed of light, the chirality corresponds to that particle's helicity, defined as the projection of its spin onto its direction of linear momentum. The helicity of a particle is right-handed if the direction of its spin is the same as the direction of its motion and left-handed if opposite.

The organisation of fundamental fermionic matter particles in the Standard Model is governed by their electroweak interactions. Left-handed fermions are paired as weak isospin doublets of $T = \frac{1}{2}$, while right-handed fermions are grouped as $T = 0$ singlets. The T_3 values of each upper member of the $T = \frac{1}{2}$ doublets are $T_3 = +\frac{1}{2}$, and $T_3 = -\frac{1}{2}$ for the lower members. Table 2.1 shows how the right- and left-handed chiral state fermions of the Standard Model are organised into three generations that possess identical quantum numbers, but differ in mass.

Table 2.1 *An overview of the fermions of the Standard Model and their associated quantum numbers. Stated quantum numbers are spin, s, weak isospin, T, the third component of weak isospin, T_3, electric charge, Q, hypercharge, Y, and the number of colour states available to that particular fermion, C.*

Quarks			s	T	T_3	Q	Y	C
$\begin{pmatrix} u \\ d' \end{pmatrix}_L$	$\begin{pmatrix} c \\ s' \end{pmatrix}_L$	$\begin{pmatrix} t \\ b' \end{pmatrix}_L$	$1/2$	$1/2$	$+1/2$	$+2/3$	$+1/3$	3
			$1/2$	$1/2$	$-1/2$	$-1/3$	$+1/3$	3
u_R	c_R	t_R	$1/2$	0	0	$+2/3$	$+4/3$	3
d_R	s_R	b_R	$1/2$	0	0	$-1/3$	$-2/3$	3

Leptons			s	T	T_3	Q	Y	C
$\begin{pmatrix} \nu_e \\ e^- \end{pmatrix}_L$	$\begin{pmatrix} \nu_\mu \\ \mu^- \end{pmatrix}_L$	$\begin{pmatrix} \nu_\tau \\ \tau^- \end{pmatrix}_L$	$1/2$	$1/2$	$+1/2$	0	-1	0
			$1/2$	$1/2$	$-1/2$	-1	-1	0
e^-_R	μ^-_R	τ^-_R	$1/2$	0	0	-1	-2	0

The quarks of the Standard Model carry colour charge that allows them to interact via the strong force as described in Section 2.2. The three colour states available are labelled as red, blue, and green. The quarks also carry a fractional electric charge: up (u), charm (c), and top (t) carry a positive charge of $Q = +\frac{2}{3}$; down (d), strange (s), and bottom (b) carry negative $Q = -\frac{1}{3}$. The leptons do not carry colour charge and consist of the electron (e), muon (μ), and tau particles (τ) with their associated neutrinos (ν_e, ν_μ, and ν_τ). The neutrinos are electrically neutral while the electron, muon, and tau carry a negative electric charge of $Q = -1$.

To produce the gauge invariance of particle interactions under electroweak symmetry transformations, four vector fields, B_μ and W^a_μ (where $a = 1, 2, 3$), are required for the $\mathrm{U}(1)_Y$ and $\mathrm{SU}(2)_L$ groups respectively. For instance, when

the fermionic fields of the first generation of quarks are represented as

$$\psi_1(x) = \begin{pmatrix} u \\ d' \end{pmatrix}_L, \qquad \psi_2(x) = u_R, \qquad \psi_3(x) = d_R, \tag{2.16}$$

the corresponding electroweak Lagrangian density is given as

$$\mathcal{L} = \sum_{j=1}^{3} i\bar{\psi}_j \gamma^\mu D_\mu \psi_j - \frac{1}{4} W^a_{\mu\nu} W_a^{\mu\nu} - \frac{1}{4} B^{\mu\nu} B_{\mu\nu}, \tag{2.17}$$

where the sum over j is the sum over the fermion generation and D_μ is the covariant derivative,

$$D_\mu = \partial_\mu - ig\frac{\sigma_a}{2} W^a_\mu - ig'\frac{Y}{2} B_\mu, \tag{2.18}$$

in which σ_a are the Pauli matrices. The third term of this covariant derivative results from the $\mathrm{U}(1)_Y$ group symmetry and acts on both left- and right-handed chiral state fermions with coupling strength g'. The second term results from $\mathrm{SU}(2)_L$ and acts only on the left-handed chiral state fermions and right-handed anti-fermions with coupling g.

The kinetic terms of Equation 2.17 for each vector field are defined by

$$\begin{aligned} B_{\mu\nu} &= \partial_\mu B_\nu + \partial_\nu B_\mu, \\ W^a_{\mu\nu} &= \partial_\mu W^a_\nu - \partial_\nu W^a_\mu + g\epsilon^{abc} W^b_\mu W^c_\nu. \end{aligned} \tag{2.19}$$

The physical charged $W^\pm_\mu$ vector gauge boson fields are thus obtained via the linear combination of the first two components of W^a_μ,

$$W^\pm_\mu = \frac{1}{\sqrt{2}}(W^1_\mu \mp i W^2_\mu). \tag{2.20}$$

The third component of W^a_μ mixes with the B_μ field to form the electrically neutral vector boson fields for the photon and weak Z^0 boson, A_μ and Z_μ respectively,

$$\begin{aligned} A_\mu &= \cos\theta_W B_\mu + \sin\theta_W W_\mu^3, \\ Z_\mu &= \cos\theta_W W_\mu^3 - \sin\theta_W B_\mu, \end{aligned} \tag{2.21}$$

where θ_W is the weak mixing angle. This angle also relates the couplings g and g' via

$$\sin\theta_W = \frac{g'}{\sqrt{g^2+g'^2}}, \qquad \cos\theta_W = \frac{g}{\sqrt{g^2+g'^2}}. \tag{2.22}$$

The generalisation of the electroweak Lagrangian density for all fermion fields, $f(x)$, can be expressed as

$$\mathcal{L}_{\mathrm{EW}} = \sum_f i\bar{f}\gamma^\mu D_\mu f - \frac{1}{4}W^a_{\mu\nu}W_a^{\mu\nu} - \frac{1}{4}B^{\mu\nu}B_{\mu\nu}, \tag{2.23}$$

where the covariant derivative is now $D_\mu = \partial_\mu - ig_V(\lambda^a V^a)_\mu$. This g_V is a generic coupling constant of the fermion field to gauge boson fields, V. The corresponding generators of the symmetry group associated with the V fields are given by λ^a, and V^a is the field vector. This Lagrangian density is invariant under local transformations belonging to the $\mathrm{U}(1)_Y$ group as

$$\psi_{L,R} \to e^{i\alpha(x)\frac{Y}{2}}\psi_{L,R}, \tag{2.24}$$

affecting both chirality handednesses, while invariance under local $SU(2)_L$ transformations of

$$\psi_L \to e^{i\beta^a(x)\frac{\sigma^a}{2}}\psi_L, \tag{2.25}$$

only involves the left-handed chiral doublets. Here, $\alpha(x)$ and $\beta(x)$ are arbitrary functions of x.

2.4 The Brout-Englert-Higgs Mechanism

When regarding Equation 2.23 in the previous section, this Lagrangian density describes the electroweak interactions of Standard Model particles, but its gauge symmetry forbids the definition of a mass term for the gauge bosons. Additionally, if introduced, fermionic masses would communicate the left-handed and right-handed chiral fields (both possessing different transformation properties) and would also result in breaking the gauge symmetry. However, the $W^{\pm}$ and Z^0 bosons, and the fermions of the SM are experimentally observed to have mass, thus a mechanism that preserves gauge invariance while also prescribing masses to these particles is required for our mathematical picture.

Such a mechanism to explain the generation of mass for these particles without breaking gauge symmetry was published in three separate papers in 1964 by three independent teams: Robert Brout and François Englert [3]; Peter Higgs [4]; and Gerald Guralnik, C. Richard Hagen, and Tom Kibble [5]. Henceforth, it will be referred to as the *Brout-Englert-Higgs* (BEH) mechanism.

The BEH mechanism introduces an $\mathrm{SU}(2)_L$ doublet of complex scalar fields

$$\phi = \begin{pmatrix} \phi^+ \\ \phi^0 \end{pmatrix} = \frac{1}{\sqrt{2}} \begin{pmatrix} \phi_1 + i\phi_2 \\ \phi_3 + i\phi_4 \end{pmatrix}, \tag{2.26}$$

with the corresponding Lagrangian density

$$\mathcal{L}_{\mathrm{BEH}} = (D_\mu \phi)^\dagger (D_\mu \phi) - V(\phi), \tag{2.27}$$

where the potential, $V(\phi)$, being expressed as

$$V(\phi) = \mu^2 \phi^\dagger \phi + \lambda (\phi^\dagger \phi)^2. \tag{2.28}$$

This potential must be bounded from below to observe vacuum stability, requiring λ to be greater than 0. The shape of $V(\phi)$ is then dependent on the sign of μ^2. If $\mu^2 > 0$ then the potential will have one global minimum value when $|\phi|^2 = 0$, else if $\mu^2 < 0$ then the shape of the potential will have a continuous set of minima on the surface of the ϕ fields that satisfy

$$\phi^\dagger\phi = \frac{1}{2}(\phi_1^2 + \phi_2^2 + \phi_3^2 + \phi_4^2) = -\frac{\mu^2}{2\lambda} = \frac{v^2}{2}, \tag{2.29}$$

where v is the vacuum expectation value. These two cases for the minimum values of the potential for a complex scalar field with two degrees of freedom are illustrated in Figure 2.1.

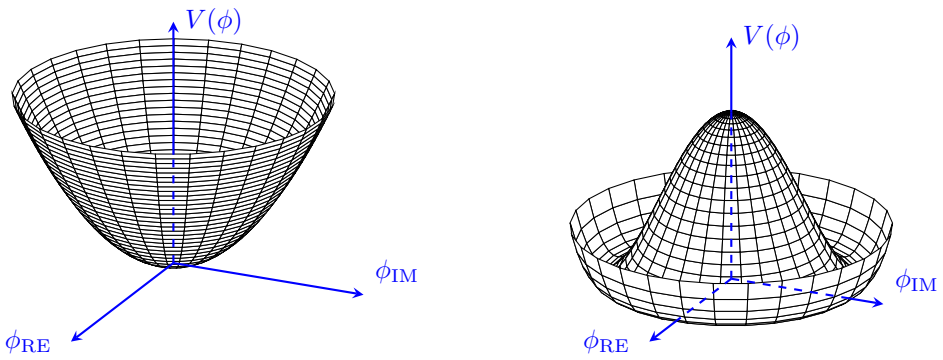

Figure 2.1 *An illustration of the BEH potential, $V(\phi)$, where $\lambda > 0$. The plot on the left depicts the case where $\mu^2 > 0$, while the right plot shows the case where $\mu^2 < 0$.*

The Lagrangian density in Equation 2.27 is invariant under local transformations belonging to $\mathrm{SU}(2)_L \otimes \mathrm{U}(1)_Y$, but this symmetry is spontaneously broken in the case where $\mu^2 < 0$. This is done by choosing a particular minimum for $V(\phi)$, which is usually chosen so that $\phi_1 = \phi_2 = \phi_4 = 0$ and $\phi_3 = v$. With this choice, the vacuum state for Equation 2.26 becomes

$$\langle\phi\rangle_0 = \langle 0|\phi|0\rangle = \begin{pmatrix} 0 \\ v/\sqrt{2} \end{pmatrix}, \qquad \left\{ v : v = \sqrt{-\frac{\mu^2}{\lambda}} \right\}. \tag{2.30}$$

As electric charge must be conserved, only an electrically neutral field may possess a vacuum expectation value. Subsequently, for the choice made in Equation 2.30, $\phi^0 = \frac{1}{\sqrt{2}}(\phi_3 + i\phi_4)$ is interpreted as the neutral field and electromagnetism remains unbroken with the vacuum state not carrying any electric charge.

Choosing a perturbation of the field about the minimum as taken in Equation 2.30 and substituting it into the Lagrangian density in Equation 2.27 results in two particles associated with the complex scalar field, ϕ. These two particles are a massless field interpreted as the Goldstone boson, and another field interpreted as a massive scalar boson.

This is problematic, however, as there is no observable massless scalar boson. To account for this, a unitary gauge is chosen; a viable course of action due to the invariance of the Standard Model Lagrangian density under local gauge transformations. The unitary gauge is chosen to set the Goldstone boson components of ϕ to zero and minimise the manifesting number of scalar degrees of freedom. It is selected such that

$$\phi(x) = \frac{1}{\sqrt{2}} \begin{pmatrix} 0 \\ H(x) + v \end{pmatrix}. \tag{2.31}$$

With the disappearance of the unphysical Goldstone boson components of ϕ, the Standard Model Lagrangian density is reinterpreted as a theory with a real massive scalar boson and with massive gauge bosons. This real scalar boson is famously known as the Higgs boson and is represented by the physical Higgs scalar field $H(x)$.

2.4.1 Bosons

The Lagrangian density in Equation 2.27 is evaluated in the unitary gauge, using the definition for the covariant derivative in Equation 2.18, as

$$\begin{aligned} \mathcal{L}_{\text{BEH}} =& \frac{1}{2}\partial_\mu H \partial^\mu H + \frac{1}{8}(v+H)^2 \left(g^2 |W_\mu^1 + iW_\mu^2|^2 + |gW_\mu^3 - g' B_\mu|^2\right) \\ & - \frac{\mu^2}{2}(v+H)^2 - \frac{\lambda}{4}(v+H)^4 \\ =& \frac{1}{2}\partial_\mu H \partial^\mu H + \frac{1}{4}(v+H)^2 \left(g^2 W_\mu^+ W^{-\mu} + \frac{g^2 + g'^2}{2} Z_\mu Z^\mu\right) \\ & - \lambda v^2 H^2 - \lambda v H^3 - \frac{\lambda}{4} H^4. \end{aligned} \tag{2.32}$$

Here, the previously massless weak $W^\pm$ and Z^0 bosons have attained mass terms that are identified as terms in Equation 2.32 containing vector boson fields, but no H field,

$$\frac{1}{2}\left(\frac{vg}{2}\right)^2 \left(2W_\mu^+ W^{-\mu} + \frac{g^2 + g'^2}{g^2} Z_\mu Z^\mu\right). \tag{2.33}$$

Then using $\cos\theta_W = \frac{g}{\sqrt{g^2+g'^2}}$ from Equation 2.22, the electroweak boson masses are given as

$$\begin{aligned} m_W &= \frac{vg}{2}; \\ m_Z &= \frac{v\sqrt{g^2+g'^2}}{2} = \frac{vg}{2\cos\theta_W} = \frac{m_W}{\cos\theta_W}; \\ m_\gamma &= 0. \end{aligned} \tag{2.34}$$

The doublet of complex scalar fields introduced by the BEH mechanism has resulted in four degrees of freedom: three of which are absorbed by the weak gauge bosons, whilst the last manifests as the Higgs boson. The mass of which can be extracted from the terms in Equation 2.32 that are quadratic in H^2 without the electroweak vector boson fields,

$$-\lambda v^2 H^2 \qquad \Rightarrow \qquad m_H = \sqrt{2|-\lambda v^2|} = \sqrt{2\lambda v^2}. \tag{2.35}$$

Terms in Equation 2.32 containing both gauge boson fields and the Higgs field describe interactions between the Higgs boson and the $W^\pm$ and Z^0 bosons, showing the existence of VVH and $VVHH$ couplings. The coupling strength of these interactions are proportional to m_V^2.

The remaining terms in Equation 2.32 describe the Higgs boson self-interactions. The terms that are proportional to H^3 describe the triple Higgs self-coupling with a strength of $\lambda_{HHH} = \frac{m_H^2}{2v}$, while the H^4 terms describe the quartic self-coupling with a strength of $\lambda_{HHHH} = \frac{m_H^2}{8v^2}$.

The mass of the Higgs boson has been measured precisely since its discovery and is still an active area of measurement at the experiments of the Large Hadron Collider. On the other hand, the vacuum expectation value of the Higgs field can be obtained from the Fermi constant as,

$$G_F = \frac{g^2\sqrt{2}}{8m_W^2} = \frac{1}{v^2\sqrt{2}} \qquad \Rightarrow \qquad v = 246\,\text{GeV}. \tag{2.36}$$

This value has been corroborated in precision measurements of the ratio of the $W^\pm$ and Z^0 boson masses and shows the energy scale at which the electromagnetic

and weak force couplings recombine into the unified electroweak interaction.

2.4.2 Fermions

Mass terms for the fermions are not a direct result of the BEH mechanism but can now be introduced without violating gauge invariance under $\mathrm{SU}(2)_L \otimes \mathrm{U}(1)_Y$ group transformations. This is done by adding Yukawa terms to the Standard Model Lagrangian density. The proposed term for a fermion is

$$\mathcal{L}_{f\phi} = -y_f \left(\bar{\psi}_L \phi \psi_R + \bar{\psi}_R \phi^\dagger \psi_L \right), \tag{2.37}$$

where y_f is the Yukawa coupling to fermion, f, ψ_L is the left-handed chiral doublet of fermion fields, and ψ_R is the right-handed chiral singlet. As an example, the electron Yukawa term with ϕ in the unitary gauge is

$$\begin{aligned} \mathcal{L}_{e\phi} &= -y_e \frac{1}{\sqrt{2}} \left(\begin{pmatrix} \bar{\nu}_e & \bar{e} \end{pmatrix}_L \begin{pmatrix} 0 \\ v+H \end{pmatrix} e_R + \bar{e}_R \begin{pmatrix} 0 & v+H \end{pmatrix} \begin{pmatrix} \nu_e \\ e \end{pmatrix}_L \right) \\ &= -\frac{y_e v}{\sqrt{2}} \bar{e}e - \frac{y_e}{\sqrt{2}} H \bar{e}e. \end{aligned} \tag{2.38}$$

The electron mass term can be identified as that without terms in H, and gives

$$m_e = \frac{y_e v}{\sqrt{2}}, \tag{2.39}$$

where this expression can be extended to all the fundamental fermions of the Standard Model. The coupling strength of the Higgs boson to any fermion is thus

$$y_f = \frac{m_f \sqrt{2}}{v}, \tag{2.40}$$

proportional to the mass of the fermion. In the unitary gauge, the mass and interaction terms for any fermion, f, with the Higgs boson are described by the Lagrangian density

$$\mathcal{L}_{f\phi} = -m_f \bar{f} f \left(1 + \frac{H}{v}\right). \tag{2.41}$$

2.5 Higgs Physics at the LHC

In the Standard Model, the Higgs boson couples to fermions with a strength proportional to the particle's mass, and to gauge bosons with a strength proportional to the square of that particle's mass. Subsequently, the production and decay modes of the Higgs boson involve the most massive fundamental particles of the Standard Model. Although it would be preferable to utilise all production mechanisms and final states for measurements, this is not feasible in practice at the Large Hadron Collider. Factors such as trigger requirements and dominant QCD background processes make statistically significant measurements in such channels difficult. Efficient triggering at the LHC requires modes that include photons, charged leptons, high transverse missing energy, or high jet transverse momentum.

2.5.1 Higgs Production

Due to the aforementioned trigger requirements, in addition to the proton-proton initial state and energy regime of the accelerator, there are four principal Higgs boson production processes at the LHC. These are depicted in Figure 2.2 and detailed in this section.

Gluon-Gluon Fusion (ggF)

This mechanism is the dominant mode for Higgs boson production at the LHC due to gluons comprising the majority of a proton's parton density function at the high energies attributed by the accelerator. The process is shown in Figure 2.2a and is given as

$$pp \to gg \to H,$$

where the Higgs boson interaction with the massless gluons is allowed via the mediation by a quark loop. Top quarks are the dominant contribution to this loop as they have the highest mass of any quark in the Standard Model, thus having

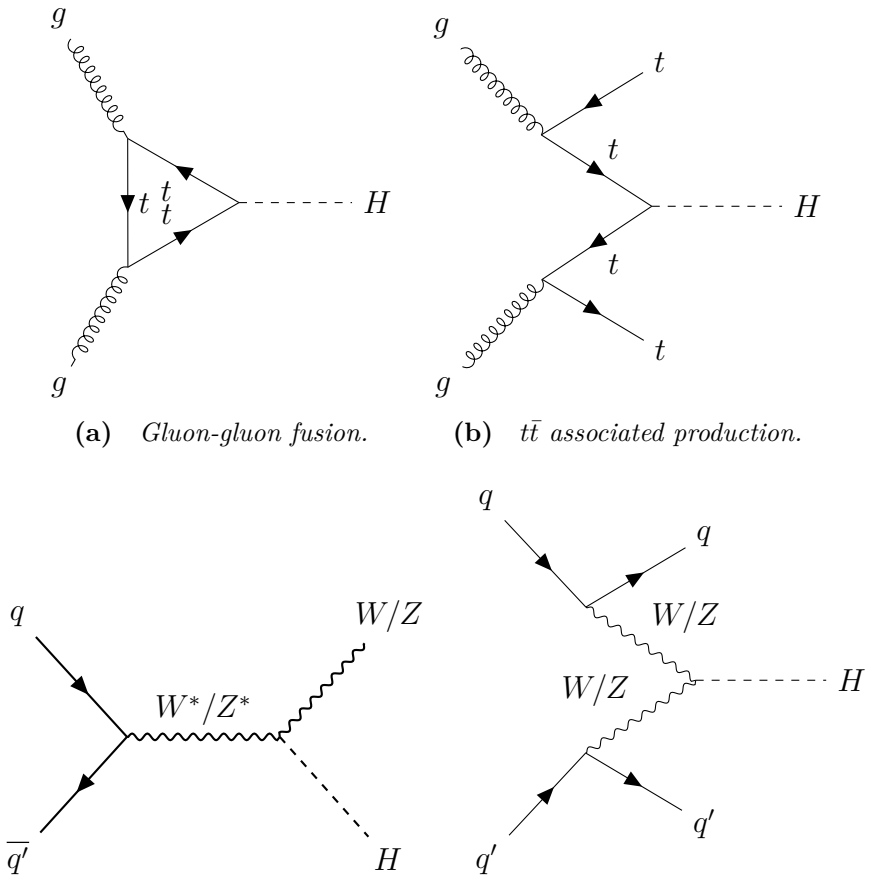

(a) *Gluon-gluon fusion.* **(b)** *$t\bar{t}$ associated production.*

(c) *W/Z associated production.* **(d)** *Vector boson fusion.*

Figure 2.2 *Feynman diagrams for leading-order processes of the four dominant Higgs boson production mechanisms at the LHC.*

the strongest coupling with the Higgs boson. Gluon-gluon fusion is responsible for approximately 88 % of total Higgs production.

Vector Boson Fusion (VBF)

This production mode is shown in Figure 2.2d and is the second largest contributing mechanism for the production of Higgs bosons at the LHC. The process is given by

$$pp \to qq' \to qq'V^*V^* \to qq'H,$$

where either $q = q'$ and $V = Z$; or $q \neq q'$ and $V = W$. This process is characterised with a well defined signal in the ATLAS detector with two highly energetic jets in the very forward regions, nearly collinear with the beam line. This is due to VBF being a purely electroweak process at leading order with

no colour exchange between the initial quarks: resulting in minimal jet activity in the pseudorapidity region between the aforementioned two forward jets. The vector boson fusion process contributes approximately 7 % to total Higgs boson production.

Vector Boson Associated Production (VH)

This process is the associated production of a Higgs boson with either a W or Z vector boson and is initiated by a quark-antiquark pair. The mechanism is illustrated in Figure 2.2c and can be written as

$$pp \to q\bar{q}' \to V^* \to VH,$$

where either $q = q'$ and $V = Z$; or $q \neq q'$ and $V = W$. This production mode also has a clean signature within the ATLAS detector, being characterised by the decay of two massive particles that can be reconstructed and identified by their decay products. When the W or Z decays leptonically then the signature is especially useful as a trigger to reduce QCD backgrounds. This process constitutes around 4 % of total Higgs boson production.

Top Quarks Associated Production ($t\bar{t}H$)

In this mechanism, the Higgs boson is produced in association with a top quark-antiquark pair. The process is shown in Figure 2.2b and is given by

$$pp \to gg \to t\bar{t}t\bar{t} \to t\bar{t}H.$$

This $t\bar{t}H$ production mode allows for the direct measurement of the Yukawa coupling of the Higgs boson to the top quark, of particular note for being the most massive fermion in the Standard Model. Top quarks are also unique as the only SM quark to have a lifetime shorter than the hadronisation timescale, meaning it decays (almost always by $t \to Wb$) before forming jets in the detector. Thus, the signature of a $t\bar{t}H$ event in the ATLAS experiment requires the reconstruction of the two top quarks from b-jets and W bosons, in addition to the reconstruction of the Higgs itself. This process produces less than 1 % of total Higgs bosons at the LHC.

Each of these four dominant Higgs production mechanisms have been observed by

the ATLAS Collaboration with significance greater than 5σ [1, 7–9], allowing for more focus on less dominant production modes in measurements. Of particular note, there are *bottom quarks associated production* and *single top associated production*.

Bottom Quarks Associated Production ($b\bar{b}H$)

This process is similar to the $t\bar{t}H$ production mechanism, but all top quarks in the Feynman diagram in Figure 2.2b are replaced with bottom quarks. However, the jets originating from lower mass b-quarks rather than t-quarks leads them to typify a lower transverse momentum and causes them to fail p_T thresholds put in place to suppress spurious jets. Consequently, $b\bar{b}H$ is less dominant in LHC measurements even though $t\bar{t}H$ has a similar cross section at the accelerator energy regime (see Figure 2.3).

Single Top Associated Production (tH)

For this mechanism, the Higgs boson is produced in association with a singular top quark, and either a W boson (tHW) or a quark (tHq). These particular processes are of interest as they allow for measurement of the sign of the top Yukawa coupling (either positive or negative). This is due to an almost totally destructive interference between two large contributions: one where the Higgs boson couples to a space-like W boson, and the other where it couples to the top quark. The tH cross section is approximately 14 % of that for $t\bar{t}H$ processes and they can be difficult to differentiate from each other.

The total theoretical cross section for all Higgs boson production mechanisms at the LHC is given in Figure 2.3 for a $m_H = 125\,\text{GeV}$ Standard Model Higgs and is shown at different centre-of-mass energies over the LHC energy regime. The cross section for each individual production process described in this chapter are also displayed.

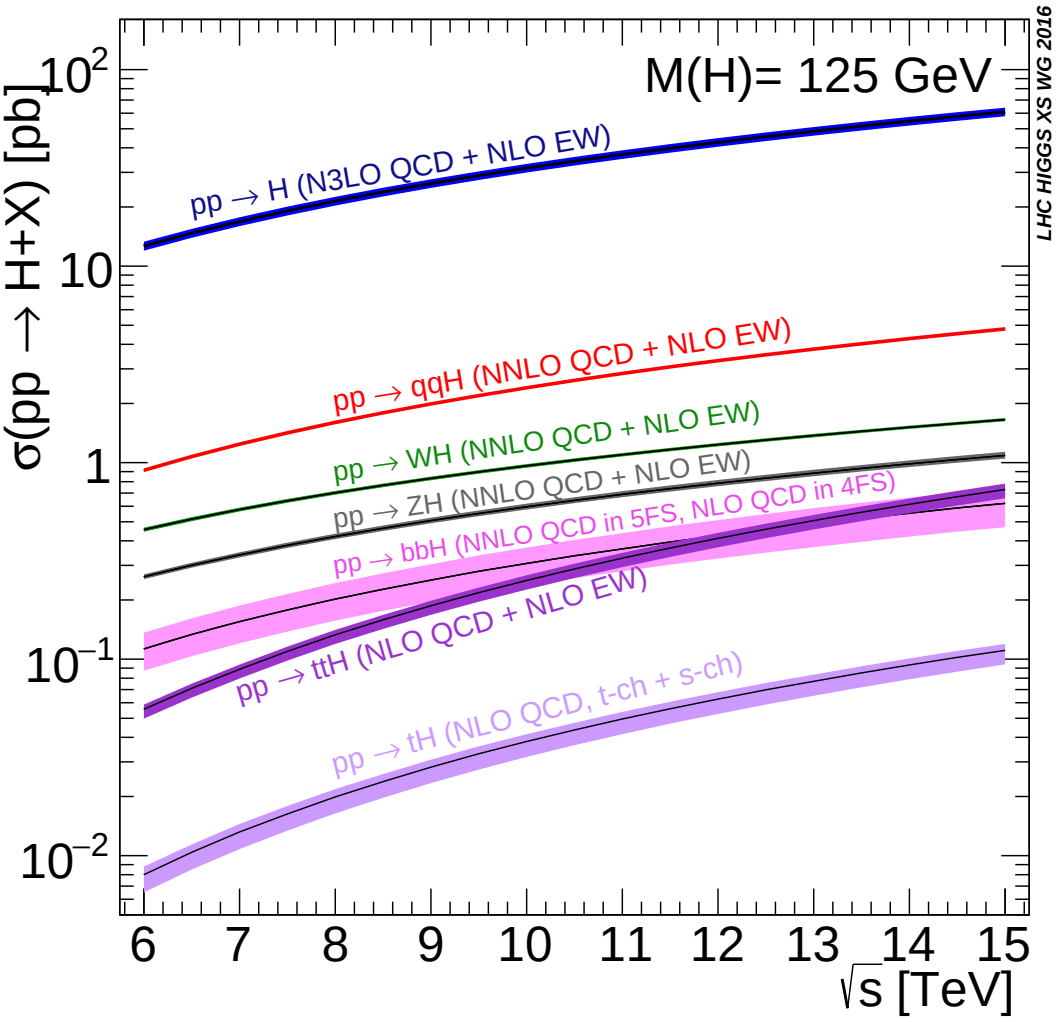

Figure 2.3 *Standard Model theoretical Higgs boson production cross sections as a function of centre-of-mass energy for a Higgs with mass $m_H = 125$ GeV. The tH production cross section only accounts for t-channel and s-channel processes (i.e. not including the tWH production mode). The width of a coloured band indicates the uncertainty for that process [6].*

2.5.2 Higgs Decay

Measurement of Higgs boson production processes are not straightforward at the Large Hadron Collider due to the short life-time of the Higgs. As such, its presence and properties can only be inferred from its decay products, ultimately resulting in measurements being of the rate of a particular production process multiplied by the probability that the Higgs decays in a particular way. Higgs boson decay modes are just as important to characterise as the production mechanisms.

The branching ratios of the Higgs boson for different decay channels are given

Table 2.2 *The Standard Model theoretical branching ratios and relative uncertainties for the dominant decay modes of a $m_H = 125$ GeV Higgs boson, in descending order [6].*

Decay Mode	Branching Ratio	Relative Uncertainty (%)
$H \to b\bar{b}$	5.824×10^{-1}	$^{+1.2}_{-1.3}$
$H \to WW^*$	2.137×10^{-1}	± 1.5
$H \to gg$	8.187×10^{-2}	± 5.1
$H \to \tau^+\tau^-$	6.272×10^{-2}	± 1.6
$H \to c\bar{c}$	2.891×10^{-2}	$^{+5.5}_{-2.0}$
$H \to ZZ^*$	2.619×10^{-2}	± 1.5
$H \to \gamma\gamma$	2.270×10^{-3}	± 2.1
$H \to Z\gamma$	1.533×10^{-3}	± 5.8
$H \to \mu^+\mu^-$	2.176×10^{-4}	± 1.7

in Table 2.2. It can be seen that they are roughly ordered by mass of the decay products, since the Higgs boson couples more strongly to more massive particles. The $H \to b\bar{b}$ channel is the most frequent decay as the top quark is too massive for the Higgs to pair produce. However, the decay to WW^* and ZZ^* are allowed even though $2m_W > m_H$ and $2m_Z > m_H$ as one of the gauge bosons in the pair is produced off-mass-shell. Also allowed are the Higgs decays to massless particles, as such decays are mediated by loops of virtual particles (the most dominant being top quark and W boson loops for $H \to \gamma\gamma$, or top and bottom quark loops for $H \to gg$).

For a given Higgs event, the sensitivity to measuring a particular decay mode is dependent on the reconstructed Higgs mass resolution, the selection efficiency of particles involved in the decay, and the level of background in the final state. The Higgs boson observed by the ATLAS and CMS experiments is measured in five important decay channels at the LHC. The $H \to \gamma\gamma$ and $H \to ZZ^* \to 4\ell$ channels allow for precise identification and measurement of all final state particles, giving excellent reconstructed Higgs mass resolution at ATLAS (typically 1–2 %). The $H \to WW^* \to \ell^+\nu_\ell\ell'^-\bar{\nu}_{\ell'}$ channel has a low reconstructed m_H resolution (around 20 %) due to the presence of neutrinos in the final state, relying on missing transverse energy to reconstruct the Higgs. Finally, the $H \to b\bar{b}$ and $H \to \tau^+\tau^-$ channel measurements are impacted by large backgrounds and result in an intermediate Higgs mass resolution of approximately 10 % and 15 % respectively. These dominant decay modes have all been observed by the ATLAS Collaboration with a significance of greater than 5σ and are currently being explored for the aforementioned production mechanisms.

$H \to \gamma\gamma$

In the $H \to \gamma\gamma$ channel, a search for a narrow peak is performed over a smoothly falling background in the invariant mass spectrum of two high transverse momentum photons. Background in this channel originates from prompt $\gamma\gamma$ processes for the irreducible backgrounds, and from the γ+jet and dijet processes for the irreducible backgrounds where one jet typically fragments into a leading π^0. ATLAS splits events into mutually exclusive categories based on Higgs production modes to optimise the search sensitivity. Categories with a better reconstructed m_H resolution and a larger signal-to-background ratio contribute the most to the sensitivity of the search.

In each category, parametric models are fitted to simulated signal line-shapes to provide a functional form for that signal. Additionally, monotonic functional forms of the background shape in each category (typically exponential, power law, or Bernstein polynomial functions) are created by a fit to the diphoton invariant mass distribution of simulated background events or data side-bands. All categories are simultaneously subjected to a signal-plus-background fit to data to determine the signal yield in each category.

This chapter outlined the Standard Model and how it expresses the fundamental interactions between matter and energy as a comprehensive QFT. The role of the Higgs boson within the SM was derived, and it was explained how its properties are measured at the LHC. The $H \to \gamma\gamma$ channel was introduced and an overview of the analysis of this decay was given. Chapter 3 will introduce the infrastructure of the LHC and the ATLAS detector, describing how the hardware is used to produce data for measurements of the $H \to \gamma\gamma$ channel.

References

[1] The ATLAS Collaboration. 'Observation of a new particle in the search for the Standard Model Higgs boson with the ATLAS detector at the LHC'. In: *Physics Letters B* 716.1 (Nov. 2012), pp. 1–29. ISSN: 0370-2693. DOI: 10.1016/j.physletb.2012.08.020.

[3] F. Englert and R. Brout. 'Broken Symmetry and the Mass of Gauge Vector Mesons'. In: *Phys. Rev. Lett.* 13 (9 Aug. 1964), pp. 321–323. DOI: 10.1103/PhysRevLett.13.321.

[4] Peter W. Higgs. 'Broken Symmetries and the Masses of Gauge Bosons'. In: *Phys. Rev. Lett.* 13 (16 Oct. 1964), pp. 508–509. DOI: 10.1103/PhysRevLett.13.508.

[5] G. S. Guralnik, C. R. Hagen and T. W. B. Kibble. 'Global Conservation Laws and Massless Particles'. In: *Phys. Rev. Lett.* 13 (20 Nov. 1964), pp. 585–587. DOI: 10.1103/PhysRevLett.13.585.

[6] D. de Florian et al. *Handbook of LHC Higgs Cross Sections: 4. Deciphering the Nature of the Higgs Sector*. CERN Yellow Reports: Monographs CERN-2017-002-M. Oct. 2016. DOI: 10.23731/CYRM-2017-002.

[7] The ATLAS Collaboration. *Observation of $H \to b\bar{b}$ decays and VH production with the ATLAS detector*. Tech. rep. ATLAS-CONF-2018-036. Geneva: CERN, July 2018. URL: https://cds.cern.ch/record/2630338.

[8] The ATLAS Collaboration. 'Combined measurements of Higgs boson production and decay using up to 80 fb^{-1} of proton-proton collision data at $\sqrt{s} = 13$ TeV collected with the ATLAS experiment'. In: *Phys. Rev. D* 101.arXiv:1909.02845 (Sept. 2019), 012002. 48 p. DOI: 10.1103/PhysRevD.101.012002.

[9] The ATLAS Collaboration. 'Observation of Higgs boson production in association with a top quark pair at the LHC with the ATLAS detector'. In: *Phys. Lett. B* 784.arXiv:1806.00425 (June 2018), 173–191. 19 p. DOI: 10.1016/j.physletb.2018.07.035.

Chapter 3

The ATLAS Detector and the LHC

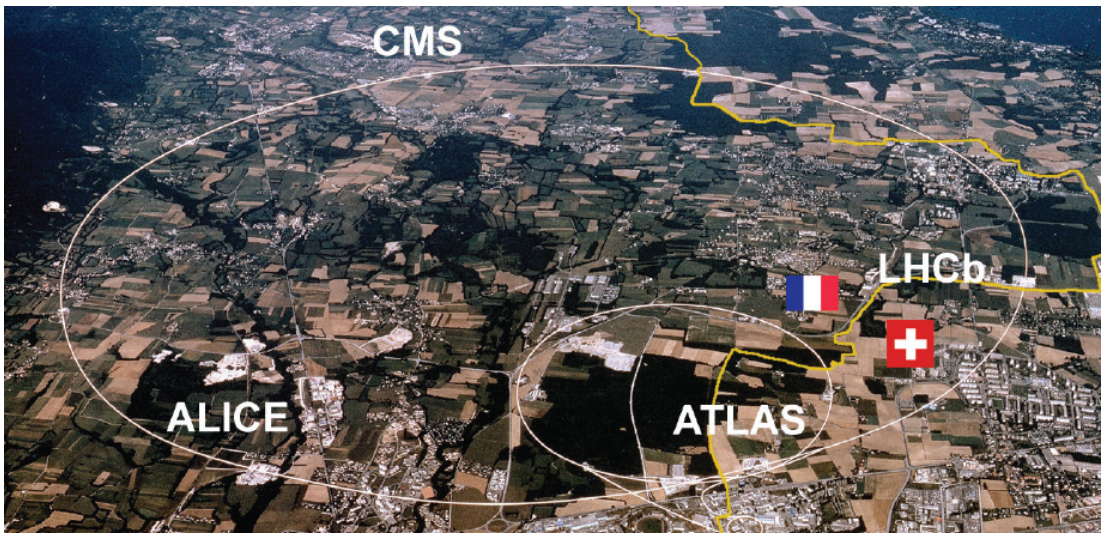

Figure 3.1 *Location of the LHC tunnel (white line) and the four main detectors across France and Switzerland, with the border shown in yellow [10].*

To collect data at the high energy frontiers required for the study of Standard Model physics and beyond, particle accelerators are used to impart energy to charged particles before colliding them and interpreting the information from the resulting signatures in particle detectors. This thesis makes use of data produced with the *Large Hadron Collider* (LHC) [11] at the *European Organization for Nuclear Research* (CERN), a circular particle collider with a circumference of 27 km located beneath the Franco-Swiss border by the city of Geneva, Switzerland. The LHC accelerates protons in two beams travelling in opposite directions before colliding them at four main interaction points about the ring. At each of these four points lies a particle detector run by the four largest

experiments at the LHC, the locations of which can been seen in Figure 3.1. ***A T**oroidal **L**HC **A**pparatu**S*** (ATLAS) [12] is one of such experiments and functions as an all-purpose hermetic detector, recording any and all data possible to be applied in a range of physics analyses.

3.1 The Large Hadron Collider

The LHC is the largest purpose-built particle accelerator in the world, capable of accelerating protons in two counter-rotating beams to centre-of-mass energies of up to $\sqrt{s} = 14\,\text{TeV}$. This is the highest energy that current research machines can impart to subatomic particles, and places the LHC at the frontier of novel high energy physics research. The 27 km circumference tunnel that houses the LHC is found underground at depths between 45 m and 170 m, where superconducting magnets guide the accelerated proton beams to collide with instantaneous luminosity exceeding $\mathcal{L} = 2\times10^{34}\,\text{cm}^{-2}\,\text{s}^{-1}$ (over twice the nominal value predicted at design).

To impart the required energy to the protons before collision, the LHC makes use of the CERN Accelerator Complex depicted in Figure 3.2. Hydrogen atoms are fed from a source at 100 keV into the LINAC2 linear accelerator where they gain energy and are stripped of their electrons, leaving the sole protons of the hydrogen nuclei, exiting LINAC2 with an energy of 50 MeV. They are subsequently injected into the Proton Synchrotron Booster (PSB), labelled as 'BOOSTER' in Figure 3.2, where they are accelerated to 1.4 GeV before entering the Proton Synchrotron (PS). Here they reach 26 GeV before being passed to the Super Proton Synchrotron (SPS) which finally inject the proton beams into the LHC with an initial energy of 450 GeV.

The proton beams in the LHC are accelerated in two beam pipes, one controlling a clockwise rotation about the ring and the other in an anticlockwise direction. Each full lap of the LHC imparts 485 keV to the protons via superconducting radio-frequency (RF) cavities until they reach their designated collision energy. Superconducting niobium-titanium dipole magnets with fields of over 8 T steer the beams in their circular trajectories, using superfluid helium to keep the temperature of the magnets below 1.9 K.

Upon reaching the desired energy, the beams are crossed in bunches of $\sim1.15\times10^{11}$

protons every 25 ns at the four designated collision points. Each collision point houses one of the four principal detectors of the LHC: *A Large Ion Collider Experiment* (ALICE) [13], designed to study the results of heavy-ion collisions; *LHC-Beauty* (LHCb) [14], focussing on *b*-physics; and the general purpose detectors, ATLAS and *Compact Muon Solenoid* (CMS) [15].

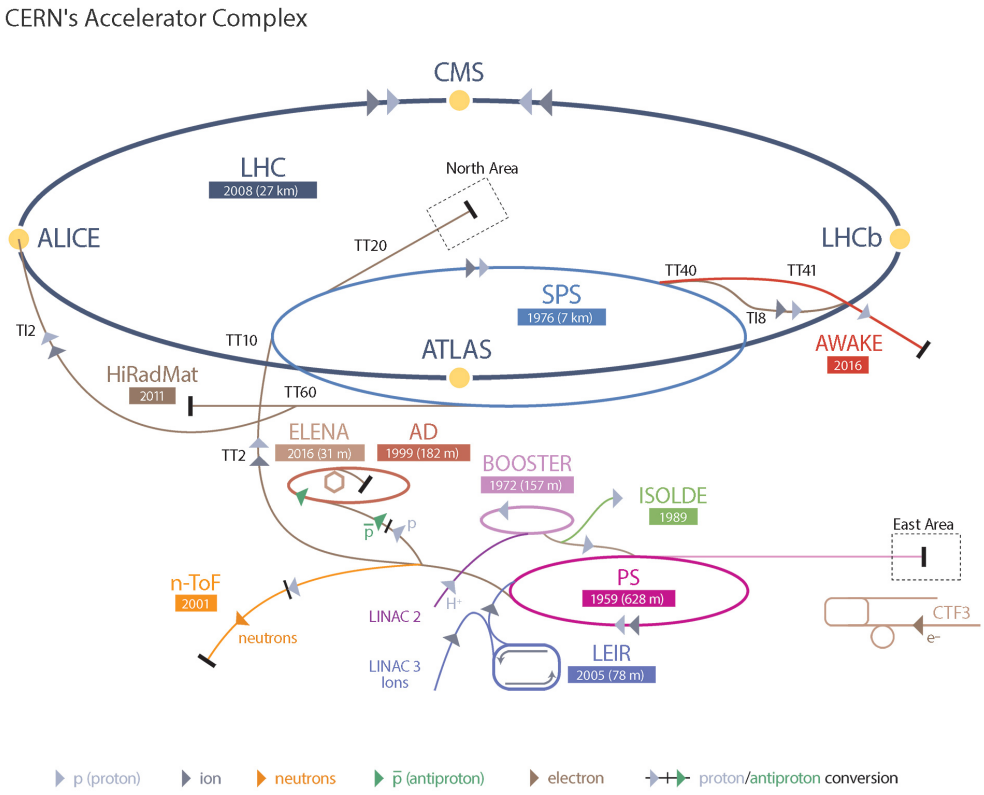

Figure 3.2 *The CERN particle accelerator complex with the LHC depicted in dark blue [16].*

3.1.1 Luminosity and Pileup

When colliding protons at the LHC, the total number of events produced via a certain process and detected by ATLAS is given by

$$N_{\text{process}} = \sigma_{\text{process}} \times \int_0^T \mathcal{L} dt, \tag{3.1}$$

where N_{process} is the number of events produced via the process in question, and σ_{process} is the *cross-section* of that process. $\int_0^T \mathcal{L} dt$ is the time integral of the *instantaneous luminosity* provided by the LHC over the total period that the

ATLAS detector has been recording and can also be referred to as the *integrated luminosity*, L. The cross-section contains all the physical effects of the probability of producing that process, while the luminosity represents the engineering and design factors involved in supplying the particle collisions. The instantaneous luminosity is given by

$$\mathcal{L} = \frac{N_b^2 n_b f_{rev} \gamma_r}{4\pi \varepsilon_n \beta^*} F, \tag{3.2}$$

where the parameters are characteristic of the supplied beams,

- N_b is the number of protons per bunch.
- n_b is the number of bunches contained per beam.
- f_{rev} is the frequency of revolution of the beam.
- γ_r is the relativistic Lorentz factor.
- ε_n is the normalised beam emittance in the transverse plane, which depends on how spread out the particles in the beam are.
- β^* is the beta focus function at the point of collision, depending on how tightly the beam is focussed by the magnets at the interaction point.
- F is a geometric term that describes how the instantaneous luminosity is reduced when the proton beams do not collide head-on. If θ_c represents the crossing angle of the beams, σ_z is the root-mean-squared (RMS) of the bunch length, and σ^* is the RMS of the transverse size of the bunch at the crossing point, then

$$F = \frac{1}{\sqrt{1 + (\frac{\theta_c \sigma_z}{2\sigma^*})^2}}. \tag{3.3}$$

Table 3.1 shows a comparison of how the different proton beam parameters for the LHC have improved over the years from 2012 to 2018 to produce a peak instantaneous luminosity exceeding twice that of the nominal design value in 2017. There were no proton beams from 2013 to 2015 due to the commencement of Long Shutdown 1 (LS1).

In Figure 3.3a, the cumulative instantaneous luminosity recorded by ATLAS for each year from 2011 to 2018 is shown.

Table 3.1 *LHC proton beam parameters for the years 2012, 2016, 2017, 2018, and the nominal values at design [17].*

LHC Parameter	2012	2016	2017	2018	Nominal
Beam Energy [TeV]	4.0	6.5	6.5	6.5	7.0
Bunch Spacing [ns]	50	25	25	25	25
n_b	1374	2220	2556	2556	2808
N_b $[1 \times 10^{11}]$	1.65	1.10	1.15	1.15	1.15
β^* [cm]	60	40	30	25	55
ε_n [µm]	2.50	2.20	2.20	2.00	3.75
Peak $\mathcal{L}$ $[1 \times 10^{34}\,\mathrm{cm}^{-2}\,\mathrm{s}^{-1}]$	0.75	1.40	2.05	2.01	1.00

An important consideration for increasing instantaneous luminosity is the mean number of inelastic interactions per bunch crossing, more often referred to as *pileup* $\langle\mu\rangle$. These inelastic collisions decrease the performance of vertex identification, track reconstruction, and the quality of reconstructed physics objects. In addition, the response time of some of the ATLAS sub-systems is slower than the designed 25 ns between each bunch crossing, possibly leaving the results of adjacent collisions superimposed with events of interest. This latter phenomenon is termed *out-of-time pileup*. Figure 3.3b depicts the mean pileup conditions as luminosity is delivered to ATLAS for the years 2015 to 2018.

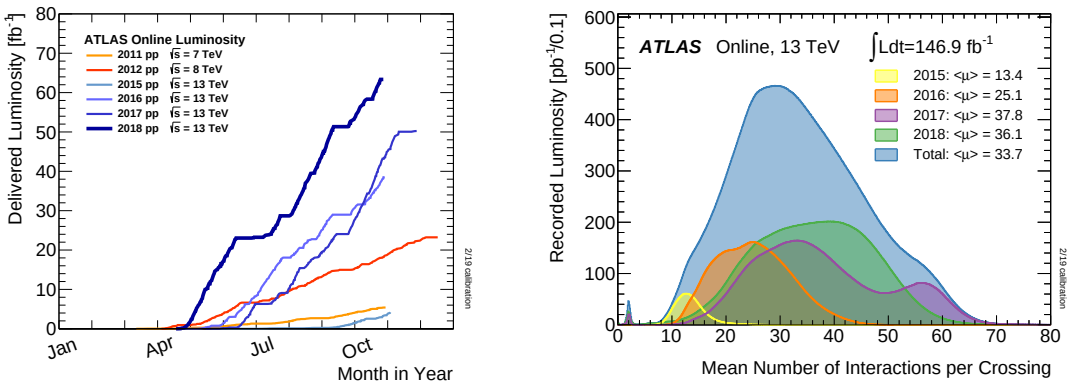

(a) **(b)**

Figure 3.3 *The integrated luminosity recorded annually by the ATLAS detector from 2015 - 2018 (a), and how the luminosity delivered was affected by pileup (b) [18].*

The first 2011 and 2012 period of proton-proton collision data taken by ATLAS is termed Run 1 and is comprised of $5.08\,\mathrm{fb}^{-1}$ of integrated luminosity at $\sqrt{s} = 7\,\mathrm{TeV}$, and $21.3\,\mathrm{fb}^{-1}$ at $\sqrt{s} = 8\,\mathrm{TeV}$. Subsequently, from 2015 to 2018, Run 2 is comprised of a physics data-set with $139\,\mathrm{fb}^{-1}$ ($\pm 1.7\,\%$) of proton-proton events at $\sqrt{s} = 13\,\mathrm{TeV}$.

3.2 The ATLAS Detector

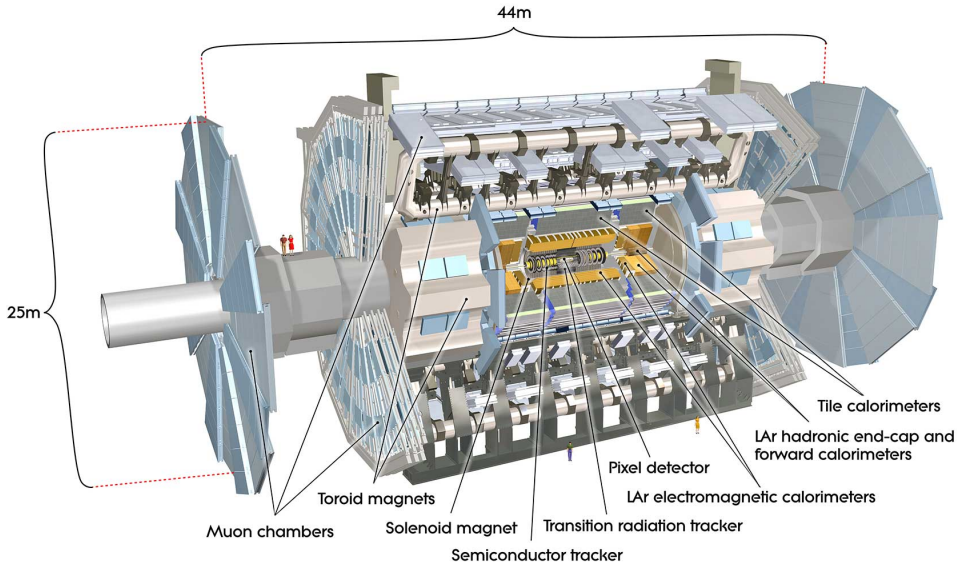

Figure 3.4 *The ATLAS detector with its main component layers labelled [12].*

The ATLAS detector, depicted in Figure 3.4, is one of two general purpose detectors at the LHC along with the CMS detector, built to record data from a large range of particle interactions as accurately as possible. It is the largest in physical size of all the detectors at the LHC and forms a roughly cylindrical shape, approximately 25 m in diameter, 44 m in length, and is located around 100 m below the surface at Point 1 of the LHC. As can be seen in Figure 3.4, it is composed of multiple detector layers to extract the maximum amount of information from an event.

The detector was designed to facilitate the discovery or exclusion of the Higgs boson whilst supplying the capability of detecting an expansive selection of events indicative of physics beyond the Standard Model. To this end, the ATLAS detector must be able to differentiate between electrons, photons, hadronic jets, and muons over a great range of energies, in addition to enabling the reconstruction of missing transverse energy for the inference of neutrinos. As such, the cylindrical shape of the detector was built with a forward-backward symmetry and almost complete coverage about the *interaction point* (IP). A succession of sub-detector layers are placed optimally about the IP to extract the information needed for the measurement and identification of the previously mentioned particles. The barrel-shaped *Inner Detector* (ID) lies

closest about the IP and tracks the trajectories of charged particles through its active volume. The ID is encompassed by the *Electromagnetic Calorimeter* (ECal) for the destructive measurement of the energy of particles that interact primarily via the electromagnetic interaction. This is in turn encompassed by the *Hadronic Calorimeter* (HCal) for the purpose of measuring the energy of strongly interacting particles. The design of the ECal and HCal is such that all particles other than muons and neutrinos are absorbed. For the purpose of measuring the properties of muons produced within the detector, the final layer of ATLAS is comprised of the *Muon Spectrometer* (MS). Neutrinos cannot be detected and are thus inferred by an overall imbalance in momentum throughout the entire event. The hermetic design of ATLAS for containing all the other products of events at the IP is therefore essential in order to measure the momentum imbalance as accurately as possible.

Specifications of the aforementioned sub-detectors are detailed in the subsequent sections of this chapter. A more complete description of all aspects and technical specifications of the detector can be found at [12].

3.2.1 Coordinate System

The coordinate system as used by ATLAS to describe the detector and the particles measured within its volume takes the physical centre of the detector as the origin. The positive x-axis of the coordinate system is defined as pointing from the interaction point to the centre of the LHC ring, while the positive y-axis is pointing upwards to the earth's surface. The z-axis is measured along the beam line with its positive direction being perpendicular to the x- and y-axes with a right-handed basis.

It is also useful to define the detector in ϕ and η coordinates due to the cylindrical geometry of ATLAS. The ϕ coordinate is the azimuthal angle that is measured in the x–y plane about the z-axis, taking values in the range $-\pi \leq \phi \leq \pi$. Defining θ as the polar angle between a desired point and the z-axis, the pseudorapidity, η, is defined as

$$\eta = -\ln\left(\tan\left(\frac{\theta}{2}\right)\right) \tag{3.4}$$

and can range from $-\infty < \eta < \infty$. Figure 3.5 summarises the ATLAS coordinate

system as described in this section.

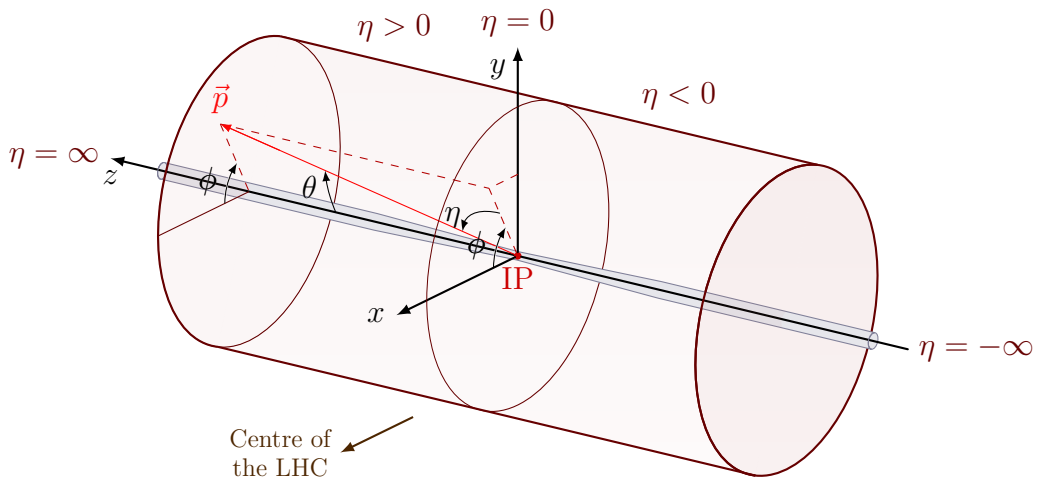

Figure 3.5 *The coordinate system as used by ATLAS. This graphic was produced by adapting code from the following citation [19].*

The η coordinate is often preferred over the polar angle as differences in pseudorapidity are Lorentz invariant in the highly relativistic case for particles under boosts along the z-axis. Transverse momentum, p_T, transverse energy, E_T, and missing transverse energy, E_T^{miss} or MET, are those quantities defined perpendicular to the beam axis (in the x–y plane). The angular separation, ΔR, in the pseudorapidity-azimuthal angle space is given by

$$\Delta R = \sqrt{(\Delta\eta)^2 + (\Delta\phi)^2}. \tag{3.5}$$

3.2.2 Magnetic Apparatus

To measure the momenta of charged particles produced at the IP, a strong magnetic field is required throughout the Inner Detector. This field is produced by a central solenoid with a strength of 2 T in the direction of the beam line (z-axis), bending charged particles in the transverse plane. Outside the calorimeters, a field is also supplied to facilitate the tracking and triggering of muons in the barrel and end-cap sections of the muon system. Here ATLAS utilises its eponymous toroidal magnets, providing 0.5 T within the barrel, and 1 T in the end-cap regions. The total volume of the magnetic field contained within ATLAS is 12 000 m^3.

The solenoid is physically thin while providing a high axial field strength, allowing it to provide tracking information in the ID but minimises the material that

particles must travel through before reaching the ECal. The solenoid is 5.8 m long and possesses an outer diameter of 2.56 m.

The 0.5 T toroidal magnet system is composed of eight coils: each being 25 m in length, 4.5 m tall, and cooled to a temperature of 4.5 K via its own cryostat. The 1 T toroidal system in each end-cap also contains eight coils, though each is shorter at a length of 5 m, and all use a common cryostat to maintain 4.5 K. The coils in the barrel and each end-cap are arranged radially with an eight-fold symmetry, with the end-cap systems rotated 22.5° with respect to those in the barrel. The relative arrangement of the magnetic apparatus within ATLAS is depicted in Figure 3.6.

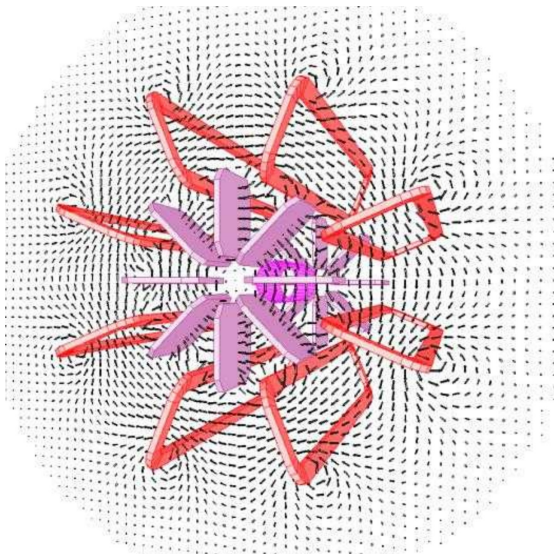

Figure 3.6 *The ATLAS magnetic apparatus showing the solenoid in magenta, the end-cap toroids in pink, and the barrel toroids in red. The toroidal field lines are depicted by the vector arrows, whilst the solenoidal field lines lie parallel to the central axis of the detector [20].*

3.2.3 Inner Detector

The Inner Detector is a system dedicated to the tracking of charged particles. It allows the reconstruction of their trajectories, primary and secondary vertices, and the measurement of their momenta and direction. It consists of three sub-detectors in three layers about the interaction point, each utilising a different tracking technology. The granularity of each subsequent layer in the ID is successively more coarse with radial distance from the IP. Closest to the IP lies the *Pixel Detector* with its high tracking resolution silicon pixel, augmented

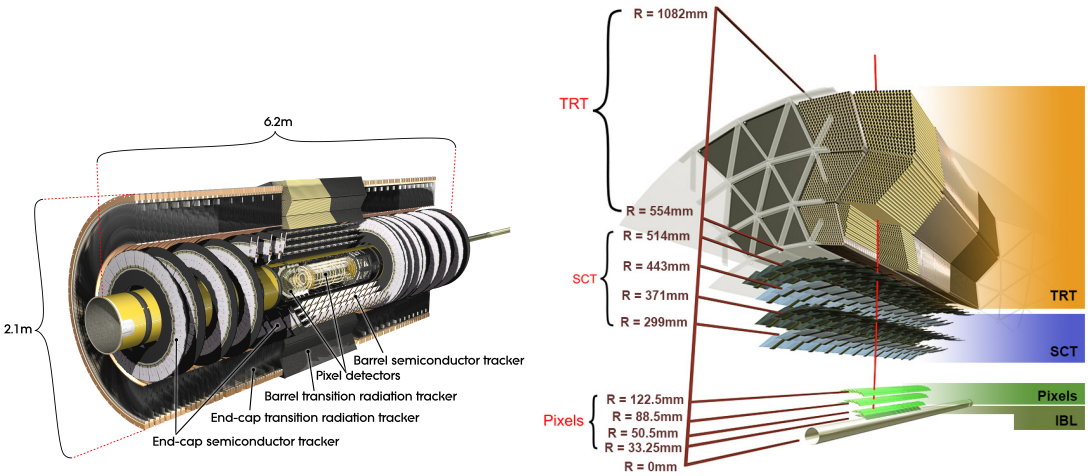

(a) (b)

Figure 3.7 *The ATLAS Inner Detector with its sub-detector systems labelled (a) [12], and the comprising layers of the Inner Detector systems in the barrel region and their radial distances from the beam axis (b) [21].*

by the *insertable b-layer* (IBL) added after the conclusion of Run 1 to increase impact parameter resolution and improve performance lost by radiation damage to the most central parts of the Pixel Detector. Next is the *Semi-Conductor Tracker* (SCT) with its silicon microstrips. The final sub-detector of the ID is the *Transition Radiation Tracker* (TRT) which utilises straw-tube proportional chambers. Each sub-detector layer is divided into three parts: a central barrel region, and two end-caps on each side; all enveloped in the 2 T axial magnetic field produced by the solenoid that sits outside the TRT, between the ID and ECal as described in Section 3.2.2. The entire Inner Detector, as shown in Figure 3.7a, occupies sufficient volume to provide tracking coverage of charged particles up to $|\eta| \leq 2.5$. Figure 3.7b depicts the radial distance of the composite layers of the ID sub-detectors from the beam axis.

Pixel Detector

The first layer of the Pixel Detector is just 50.5 mm from the IP. Due to this proximity, it is instrumental in the identification and reconstruction of primary vertices from particle collisions at the interaction point, and secondary vertices from b-hadrons. The barrel section of the Pixel Detector consists of three silicon layers arranged as concentric cylinders sharing an axis with the beam pipe, while each end-cap is composed of three silicon discs arranged on either side of the barrel and in the transverse plane, perpendicular to the beam-pipe. Each of the

silicon layers are comprised of $6\times2\,\mathrm{cm}^2$ rectangular pixel modules. There are 1456 modules in the barrel and 288 in the end-caps combined, each module is identical and contains 46 080 separate pixels measuring 50 µm in the azimuthal (r–ϕ) direction and 400 µm in the $z(r)$-direction for the barrel (end-caps). In total this results in 80.4 million individual silicon pixels, each a reverse bias diode, available in the sub-detector to register charged particles that pass through them. On average, three hits will be produced via a charged track passing through the three layers of the Pixel Detector, providing a position resolution of 10 µm in the r–ϕ plane and 115 µm in the $z(r)$-direction in the barrel (end-cap) region.

At the conclusion of Run 1, an additional barrel layer of pixel modules was installed between the beam pipe and the first Pixel Detector layer. Named the *insertable b-layer* (IBL), it lies at $r = 33.25\,\mathrm{mm}$ for the purpose of improving vertex resolution and tracking alongside enhancing the b-tagging efficiency for the Run 2 data taking period. It totes a finer pixel granularity than that in the rest of the Pixel Detector, measuring 50 µm in the r–ϕ direction and 250 µm in the z-direction. As shown in Figure 3.8, the resolution of the transverse impact parameter, d_0 (the distance between the z-axis and the closest point of a track to the z-axis as measured in the x–y plane), and the longitudinal impact parameter, z_0 (the distance between a track's z-coordinate measured at its d_0 and the extrapolated primary vertex), are both improved with the addition of the IBL.

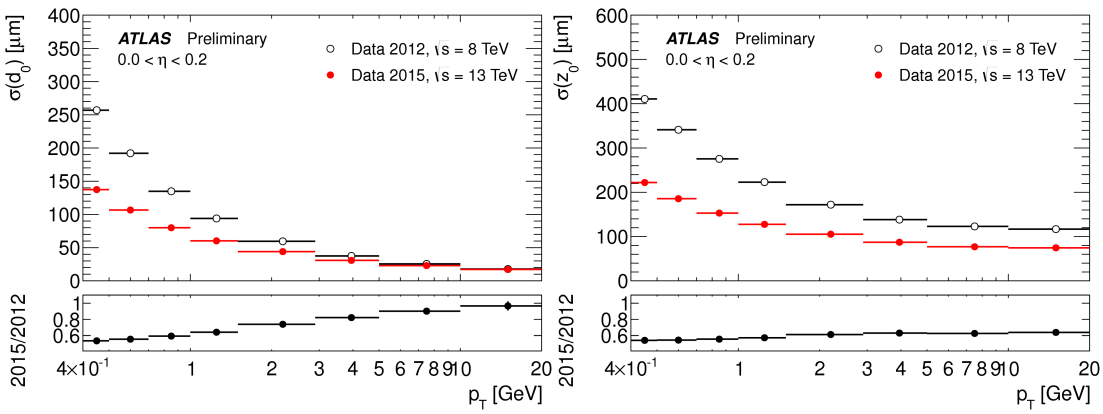

Figure 3.8 *The transverse (a) and longitudinal (b) impact parameter resolution (lower is better) as a function of the detected particle's p_T, measured without the IBL in 2012 and with in 2015 [21].*

Semi-Conductor Tracker

The Semi-Conductor Tracker provides additional position measurements for the reconstruction of charged particle tracks after the Pixel Detector. The barrel region lies between $299 \leq r \leq 514\,\text{mm}$ and is comprised of four silicon strip layers arranged into four cylinders positioned coaxially with the beam line. Each end-cap contains nine discs of SCT modules mounted as concentric circles. Two module layers per barrel cylinder and per end-cap disc are affixed to each other to attain a 40 mrad stereo angle between the direction of their respective microstrip sensors. In this way, r–ϕ positional information can be measured in the barrel and r-position in the end-cap, functioning similar to pixels in the previous sub-detector.

The SCT covers the pseudorapidity region of $|\eta| \leq 2.5$ and detects an average of four hits per charged particle passing through its volume. Utilising a total of 6.2 million read-out channels and a mean strip pitch of 80 µm, these hits are measured with an intrinsic position resolution of 17 µm in the r–ϕ plane and 580 µm in the $z(r)$-direction in the barrel (end-cap) region.

Transition Radiation Tracker

The Transition Radiation Tracker is the outer-most sub-detector of the ID. It is composed of straw tubes measuring 4 mm in diameter with a 31 µm diameter gold-plated tungsten wire running through their centres. The tubes are filled with a gas comprised of xenon, carbon dioxide, and oxygen with concentrations of 70, 27 and 3 % respectively, although some xenon has been replaced by argon due to leaks. The barrel section of the TRT uses 144 cm long straws arranged parallel to the beam pipe, while the end-caps utilise 37 cm long straws positioned radially in wheels.

These straw tubes are separated from each other by polypropylene radiator foils. When a relativistic charged particle crosses a boundary between media of different refractive indices, transition radiation (TR) photons are produced. This TR can then be absorbed by the gas mixture within the tubes, producing a signal proportional to the Lorentz factor ($\gamma = E/m$) of the original charged particle. Along with an energy measurement from the calorimeters, this allows for the distinguishing of pions from electrons by their respective signatures from the TRT.

In addition to the emitted TR, charged particles also ionise the gas as they transit through a straw tube. This frees electrons that proceed to drift towards the central wire which functions as an anode due to a potential difference between the tube walls and the wire. This induces a current as the electron drift starts that can be measured, and consequently the position of the originating particle, its distance from the tube, and the mass information from the TR signal.

The barrel region of the TRT allows for the tracking of charged particles in the $|\eta| \leq 1.0$ region and only gives r–ϕ positional information while the end-caps only provide r–z measurements for $|\eta| \leq 2.0$. A resolution of 130 µm is achieved with an average of 36 hits per track. In total the TRT has 351 000 read-out channels.

In total the Inner Detector allows for the measurement of charged particle tracks to give their momentum, direction, and impact parameters. The total resolution on a transverse momentum measurement, σ_{p_T}, can be approximated during Run 1 (without the IBL) to

$$\frac{\sigma_{pT}}{p_t} = 0.05\% \cdot p_T \oplus 1\%, \tag{3.6}$$

where $\oplus$ denotes an addition in quadrature.

3.2.4 Calorimeters

As a destructive method of measuring a particle's energy, calorimetry requires dense material to cause the particle to interact and be fully absorbed while transforming its energy into a measurable quantity. This involves the incident particle interacting with the calorimeter material through the electromagnetic or strong interaction to produce a *shower* of secondary particles. The energy deposited by the shower is detected as electric charge by a sampling medium. In homogeneous calorimeters, the sampling medium is the same as the absorber, while in a sampling calorimeter there will be alternating layers of absorber and sampler.

Particles that are primarily governed by the electromagnetic interaction (electrons and photons) will interact via pair production and bremsstrahlung at high energies, and via Compton scattering, the photoelectric effect, and ionisation at lower energies. The *radiation length* (X_0) of the calorimeter material is

defined as the average distance a high energy electron would travel before its energy reduces by $1/e$ and is the average distance an electron would travel through the detector before interacting, while a photon with $E > 2m_e$ travels around $\frac{9}{7}X_0$ on average before pair producing. On the other hand, hadrons interact through the strong force and produce gluons and further hadrons which can travel substantial distances before interacting again. They also create an electromagnetic component through the production of neutral pions and their decays to photons ($\pi^0 \rightarrow \gamma\gamma$). The related calorimeter material parameter for hadronic showers is the mean free path or *interaction length* (λ) and is the mean distance between hadronic interactions for high energy hadrons. Figure 3.9 compares the typical shape of an electromagnetic shower to a hadronic one. As can be seen, the hadronic shower is much less dense and has a broader lateral shape [22].

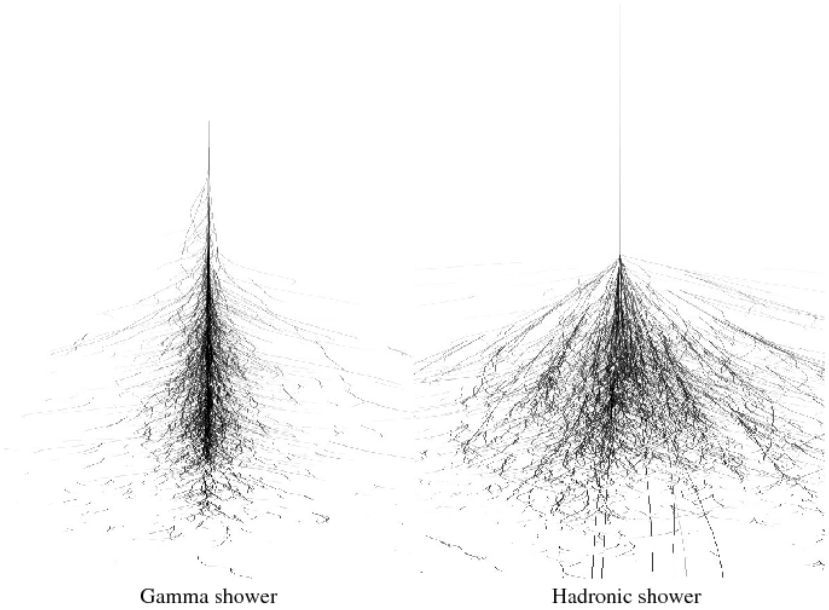

Figure 3.9 *The differences in form between an electromagnetic shower on the left and a hadronic shower on the right [23].*

The calorimeter system of the ATLAS detector is shown in Figure 3.10. It is placed outside of the Inner Detector, occupies the pseudorapidity range of up to $|\eta| \leq 4.9$, and is divided into three sub-detectors. Each of these sub-detectors utilises different technologies to specialise each system to a particular form of calorimetry.

The *Electromagnetic Calorimeter* (ECal) is the first sub-system outside of the ID and is split into a central barrel (EMB) and two end-cap (EMEC) regions that all make use of liquid argon (LAr) as the active material, and use lead as

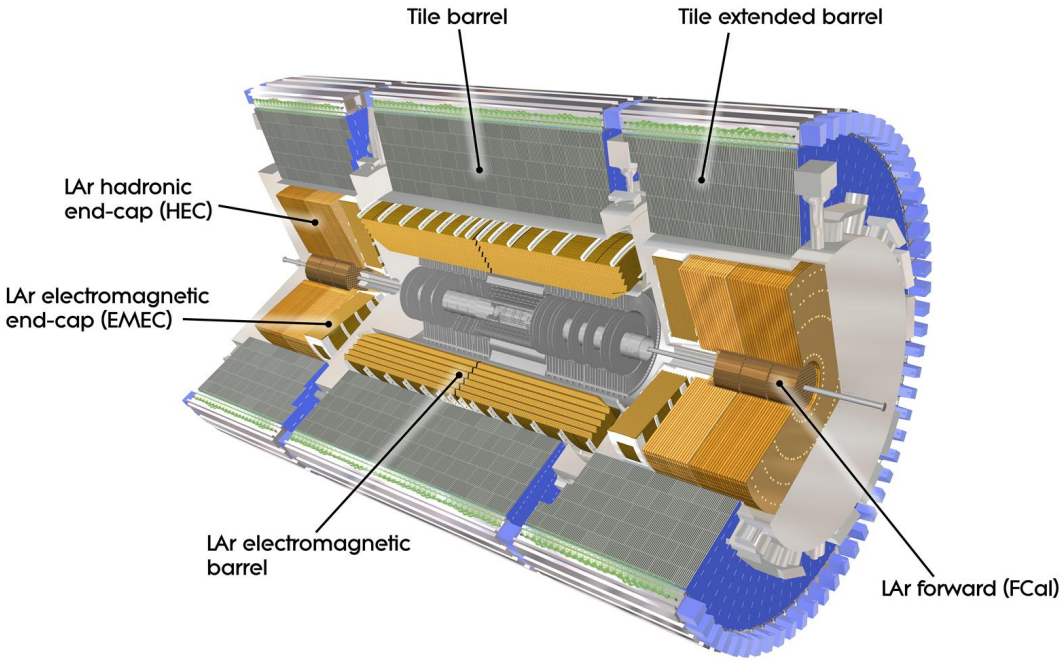

Figure 3.10 *The ATLAS calorimeter systems where the different sub-detectors are labelled [12].*

the absorbing medium. The *Hadronic Calorimeter* (HCal), which is positioned outside the ECal, is also comprised of a barrel region and two end-caps. The hadronic end-caps (HEC) use LAr as in the ECal, but make use of copper as an absorber, while the barrel region (TileCal) uses steel absorbing layers and plastic scintillating tiles as the active medium. The TileCal itself is comprised of three cylindrical sections with a central barrel and two identical extended barrels, each on either side of the central region to increase the covered pseudorapidity range. The final calorimeter sub-detector lies about the beam pipe within the HEC and is known as the *Forward Calorimeter* (FCal). The FCal utilises LAr as the sampling medium and copper absorbing medium in the first layer, while subsequent layers use tungsten.

The resolution of energy measured by the calorimeters can be generalised by

$$\frac{\sigma E}{E} = \frac{a}{\sqrt{E}} \oplus \frac{b}{E} \oplus c. \tag{3.7}$$

The first term is referred to as the *stochastic term* and arises from the statistical fluctuations in the development of the particle shower, it is proportional to the

inverse of the square root of the initial particle energy and is parametrised for each layer by a. Next is the *noise term* describing pileup and the electronic noise contributed by the readout systems (negligible at ATLAS), it is proportional to the inverse of the initial particle energy and is parametrised by b. The final contribution is known as the *constant term* that arises from instrument calibration and dead material effects, it is independent of the initial particle energy and is parametrised by c.

The depth of the calorimeter systems is important as they have to give satisfactory containment of the hadronic and electromagnetic showers and minimise non-muon particles reaching the muon system. The total thickness of the electromagnetic barrel is more than $22X_0$, and more than $24X_0$ in the end-caps. The material of the hadronic tile barrel is comprised of around 9.7λ with approximately 10λ in the end-caps. Taking the outer support into account, the thickness of the hadronic calorimeter is 11λ at $|\eta| = 0$ and has been shown by simulation and measurement to be of adequate depth to contain showers and ensures good missing transverse energy reconstruction. Figure 3.11 shows the amount of material comprising the sub-systems over the covered pseudorapidity range of the ATLAS calorimeters in terms of λ.

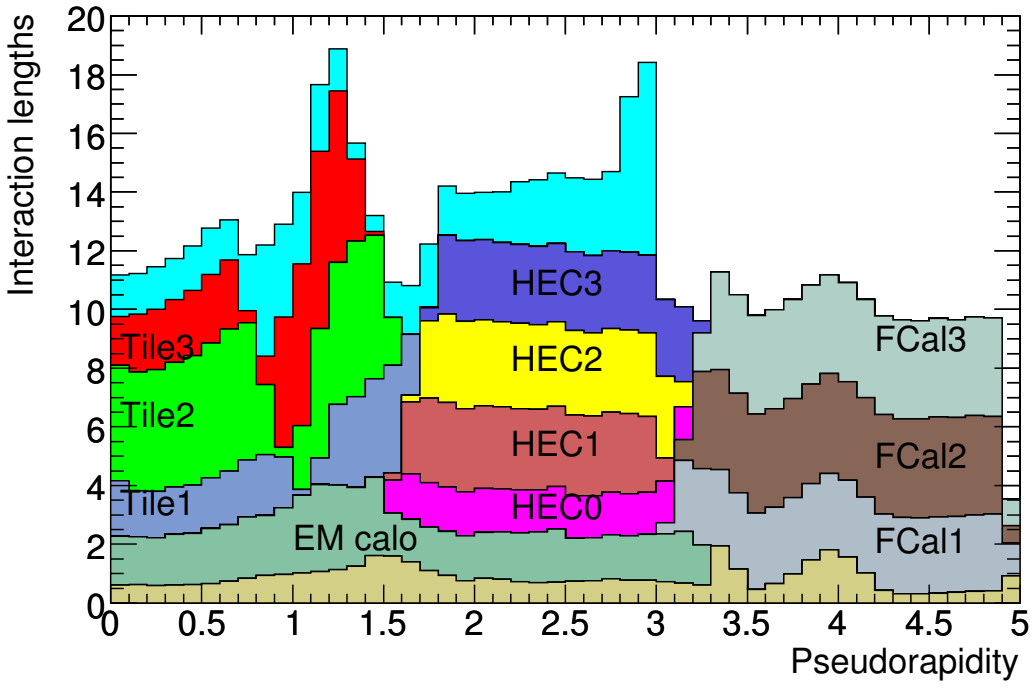

Figure 3.11 *The cumulative amount of material, in λ, as a function of $|\eta|$ for the detector before the calorimeters (beige), the ECal (teal), all layers of the HCal and FCal, and up to before the MS (aqua) [12].*

Electromagnetic Calorimeter

The Electromagnetic Calorimeter uses lead plates with a thickness of 1.53 mm for $|\eta| < 0.8$ or 1.13 mm for $|\eta| > 0.8$ as the absorbing material of the sampling system. The active liquid argon medium is arranged in 2 mm layers and interspersed with copper readout electrodes to collect the charge released from the shower particles ionising the LAr. The lead and electrode layers are arranged in an accordion geometry to provide a full azimuthal coverage without any cracks, and to allow for the rapid extraction of signal at the front and rear of the electrodes.

The ECal is composed of a central barrel region (EMB) occupying $|\eta| \leq 1.475$ and two wheel shaped end-caps to either side of the barrel to cover the $1.375 \leq |\eta| \leq 3.2$ region. The EMB shares the same cryostat as the solenoid while the EMECs use their own separate cryostats to maintain the 88 K operating temperature required by the liquid argon.

There are three sampling layers comprising the ECal in the $|\eta| \leq 2.5$ region and two in the $2.5 \leq |\eta| \leq 3.2$ region, while a presampling layer precedes these in the $|\eta| \leq 1.8$ region. This presampler is a thin layer of only active liquid argon for the purpose of correcting for energy lost in the ID, the solenoid, and the walls of the cryostat. The sampling layers in the central ($|\eta| \leq 1.4$) region can be summarised as follows

- **Sampling Layer 1** is comprised of strip cells with a $\Delta\eta \times \Delta\phi$ granularity of 0.0031×0.0980. This layer allows for a precision measurement of the electromagnetic showers and provides an excellent discrimination between hadronic (hadrons) and electromagnetic objects (photons and electrons) and also allows for the resolving of two separate photons in close proximity. It has a thickness of approximately $4.3X_0$.
- **Sampling Layer 2** is the thickest part of the ECal with a thickness of up to $17X_0$, and so absorbs the majority of the electromagnetic shower. This layer is comprised of cuboid tower cells with a granularity of $\Delta\eta \times \Delta\phi = 0.0250 \times 0.0245$.
- **Sampling Layer 3** has a thickness of around $2X_0$ and is the final layer in the ECal, ensuring that electromagnetic showers are entirely captured by the sub-system. It is composed of tower cells with a granularity of $\Delta\eta \times \Delta\phi = 0.0500 \times 0.0245$.

Figure 3.12 depicts the structure of the described cells comprising the ECal sampling layers in the central $|\eta| \leq 1.4$ region. The orientation of the accordion shaped electrodes is also shown.

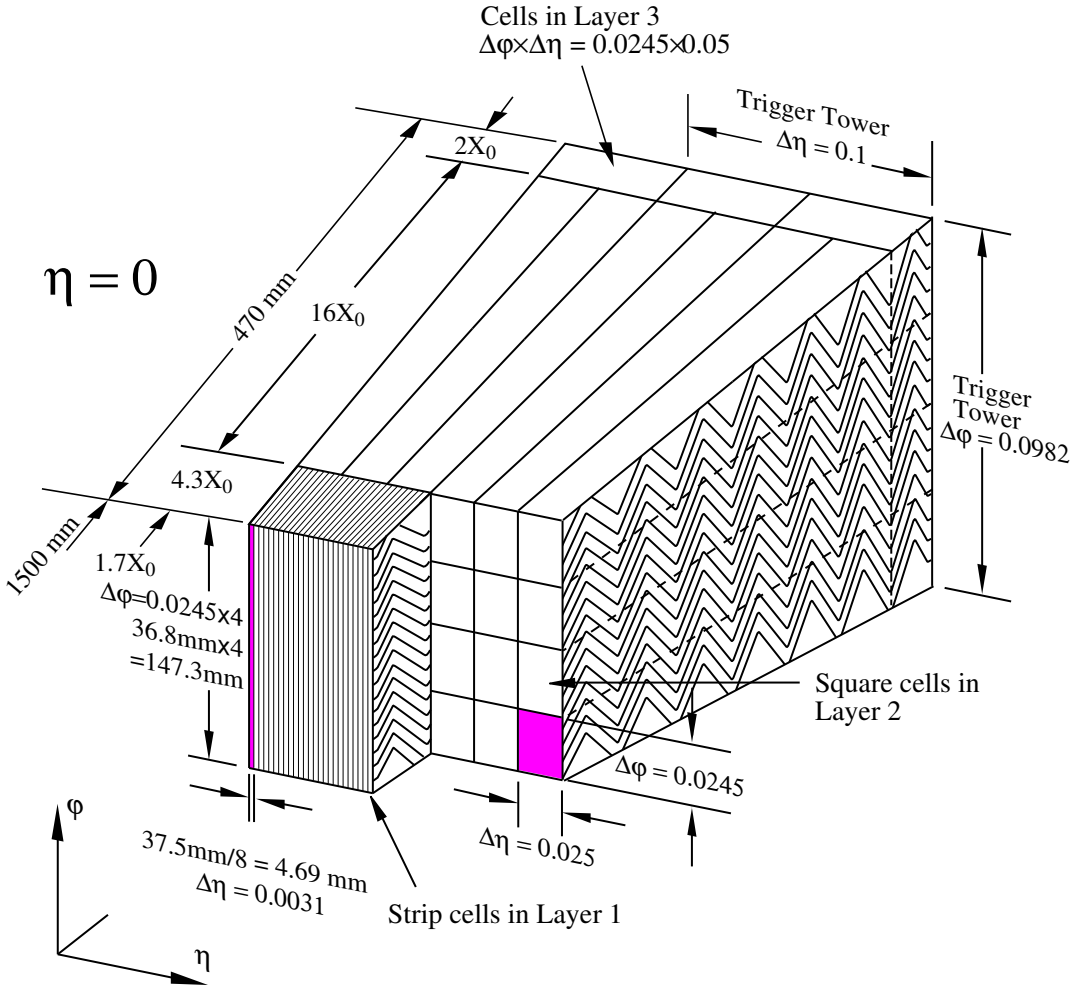

Figure 3.12 *A barrel module in the ATLAS Electromagnetic Calorimeter depicting the arrangement of cells within the sampling layers for $|\eta| \leq 1.4$ [12].*

The granularity and material thickness of the sampling layers in the ECal vary over the pseudorapidity range that the sub-detector covers. Table 3.2 summarises how the cell sizes change while Figure 3.13 depicts how the cumulative radiation length of the Electromagnetic Calorimeter varies with $|\eta|$ for the barrel and end-cap regions.

The design energy resolution of the Electromagnetic Calorimeter is

$$\frac{\sigma E}{E} = \frac{10\%}{\sqrt{E}} \oplus 0.7\%. \tag{3.8}$$

Table 3.2 *Cell granularity for different $|\eta|$ regions of each layer of the Electromagnetic Calorimeter in the EMB and EMEC [12].*

Sampling Layer	Barrel		End-Caps	
	Pseudorapidity	Granularity	Pseudorapidity	Granularity
Presampler	$\|\eta\| < 1.52$	0.025×01	$1.5 < \|\eta\| < 1.8$	0.025×0.1
1	$\|\eta\| < 1.40$ $1.40 < \|\eta\| < 1.475$	0.003×0.1 0.025×0.025	$1.375 < \|\eta\| < 1.425$ $1.425 < \|\eta\| < 1.5$ $1.5 < \|\eta\| < 2.5$ $2.5 < \|\eta\| < 3.2$	0.050×0.1 0.025×0.1 0.003-0.025×0.1 0.1×0.1
2	$\|\eta\| < 1.40$ $1.40 < \|\eta\| < 1.475$	0.025×0.025 0.075×0.025	$1.375 < \|\eta\| < 1.425$ $1.425 < \|\eta\| < 2.5$ $2.5 < \|\eta\| < 3.2$	0.050×0.025 0.025×0.025 0.1×0.1
3	$\|\eta\| < 1.35$	0.050×0.025	$1.5 < \|\eta\| < 2.5$	0.050×0.025

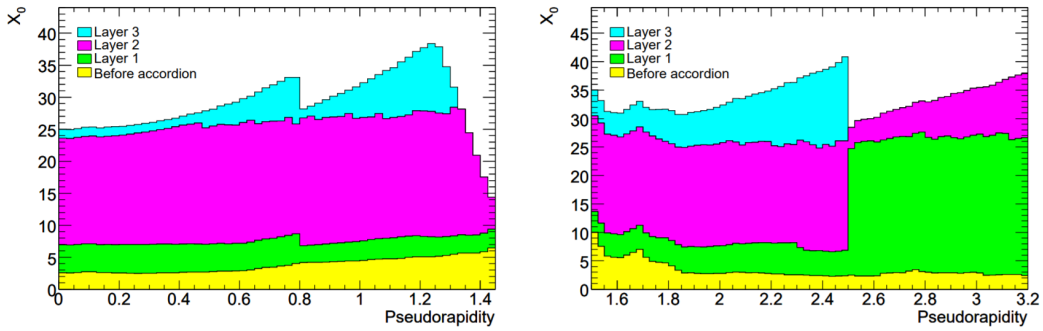

Figure 3.13 *The cumulative amount of material, in terms of X_0, as a function of $|\eta|$ for the detector before the calorimeters (yellow) and for each sampling layer of the ECal. The barrel region is shown in the left plot while the right depicts the end-caps [12].*

Hadronic Calorimeter

The TileCal barrel region makes use of alternating layers of 14 mm thick steel plates and 3 mm thick plastic scintillating tiles and is divided into the main barrel ($|\eta| \leq 1.0$) and two extended barrels ($0.8 \leq |\eta| \leq 1.7$). The steel absorbing medium causes hadrons to interact via the strong force, creating showers of further hadrons, photons, and electrons that proceed to excite the atoms within the scintillator tiles to produce scintillation light that is collected and read out by photomultiplier tubes to provide the signal. To produce a measure of the energy of the original particle, the signal is totalled over many layers of tiles in a depth called a tower. The TileCal is structured into three layers with cells of granularity $\Delta\eta \times \Delta\phi = 0.1 \times 0.1$ in the first two layers, and $\Delta\eta \times \Delta\phi = 0.2 \times 0.1$ in the final layer.

Each end-cap in the HEC is split into two wheels (a front and a back wheel)

arranged in the same orientation as the EMEC and lying further along the z-axis. They use the same LAr technology as the ECal but utilise copper plates as the absorber with thicknesses of 25–50 mm. Each end-cap shares a cryostat with the corresponding end-cap of the EMEC and covers a pseudorapidity range of $1.5 \leq |\eta| \leq 3.2$. Cells in the HEC have sizes of $\Delta\eta \times \Delta\phi = 0.1 \times 0.1$ in the $|\eta| \leq 2.5$ region and $\Delta\eta \times \Delta\phi = 0.2 \times 0.2$ for larger pseudorapidity values.

The energy resolution in the HCal is

$$\frac{\sigma E}{E} = \frac{50\%}{\sqrt{E}} \oplus 3\%. \tag{3.9}$$

Forward Calorimeter

The Forward Calorimeter is comprised of three layers, occupies the $3.1 \leq |\eta| \leq 4.9$ region and lies in the centre of the HEC wheels. The first layer is designed for measuring electromagnetic showers while the outer two layers are designed for hadronic measurements. The FCal uses a LAr active medium and each side shares a cryostat with the corresponding EMEC and HEC end-cap. The EM part of the FCal uses copper absorbing material while the hadronic part uses tungsten. The FCal is vital for the measurement of missing transverse energy in an event, as well as for reconstructing forward jets produced at large η. The energy resolution of the Forward Calorimeter is designed to be

$$\frac{\sigma E}{E} = \frac{100\%}{\sqrt{E}} \oplus 10\%. \tag{3.10}$$

3.2.5 Muon Spectrometer

Due to their highly penetrating nature, only muons and neutrinos are not absorbed by the ATLAS calorimeters and reach the Muon Spectrometer. This sub-detector is designed to deliver a precise momentum measurement of such particles independently of the Inner Detector in the $|\eta| \leq 2.7$ region. However, as neutrinos have such a low interaction probability, it is not feasible to directly measure their properties with ATLAS; therefore, the sole subjects of Muon Spectrometer measurements are, unsurprisingly, muons.

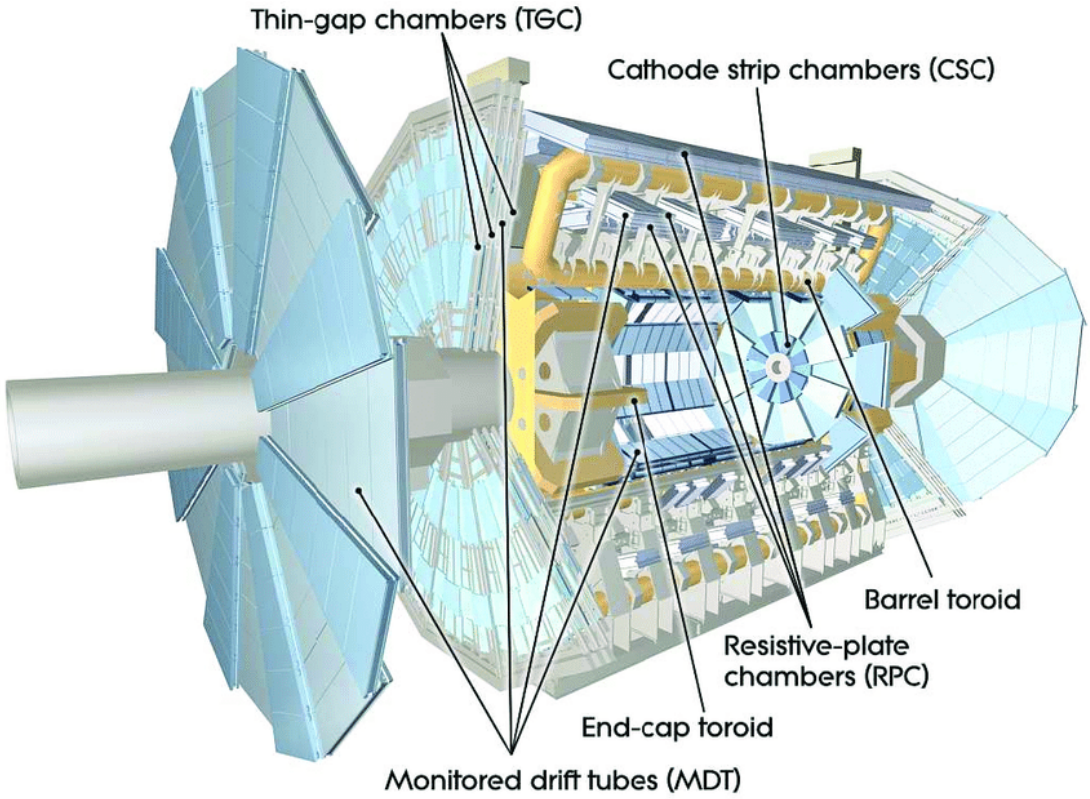

Figure 3.14 *The ATLAS Muon Spectrometer where the comprising sub-detectors are labelled [12].*

The sub-detector is composed of the toroidal superconducting magnet system as described in Section 3.2.2, high-precision tracking (*Type I*) chambers, and fast response detection (*Type II*) chambers. *Monitored Drift Tubes* (MDTs) and *Cathode Strip Chambers* (CSCs) comprise the Type I sub-detectors, and are responsible for providing momentum measurements of the muons. While *Resistive Plate Chambers* (RPCs) and *Thin Gap Chambers* (TGCs) form the Type II systems that allow for triggering on an event in the $|\eta| \leq 2.4$ region. All sub-detectors in the muon system are gaseous, detecting the ionisation of gas through their volume caused by the passage of muons. Together these systems measure the deflection of muon tracks through the r–z plane caused by the toroidal magnetic field acting perpendicularly to the beam axis and that of the solenoid. Figure 3.14 depicts the Muon Spectrometer and the positions of its magnets and sub-detectors.

- **MDTs** are comprised of layers of three to eight drift tubes containing a gas mixture of 93 % argon and 7 % carbon dioxide. The layers are grouped into chambers and arranged so the tubes are aligned in ϕ. They occupy the

whole $|\eta| \leq 2.7$ region but in the $2.0 \leq |\eta| \leq 2.7$ region the first layer is replaced by CSCs due to the high radiation levels there.

- **CSCs** are multiwire proportional chambers composed of cathode planes split into strips arranged orthogonally to the bending plane, allowing for tracking in the r–z and transverse planes. They are arranged into two discs of eight chambers and contain a gas mixture of 93 % argon and 7 % carbon dioxide.

- **RPCs** are attached to the MDT chambers in the barrel ($|\eta| \leq 1.05$) region where they form three concentric cylinders. They utilise two parallel resistive plates with 2 mm separation in a 94.7 % tetrafluoroethane, 5 % isobutane, and 0.3 % sulphur hexafluoride gas mixture. The read-out signal is much faster than in the Type I systems allowing for online event selection based on the presence of muons.

- **TGCs** form multiwire proportional chambers arranged into concentric wheels in the $1.05 \leq |\eta| \leq 2.4$ region. Here they provide a ϕ position measurement to compliment the r–z information from the MDTs. They are functionally similar to the CSCs but possess a smaller separation between wire strips for faster charge collection after gas ionisation. Like the RPCs this allows them to provide online muon triggering. Their gas is composed of 55 % carbon dioxide and 45 % pentane.

The transverse momentum resolution for muons with $10\,\text{GeV} \leq p_T \leq 1\,\text{TeV}$ ranges from 3–11 %. Energy losses and multiple scattering dominate the momentum resolution at low p_T, while the MDT resolution dominates at higher momentum.

3.2.6 Trigger

When recording, ATLAS produces a huge amount of data at a such a rate that makes it technologically impossible to send every single event to storage. During Run 2 operation the ATLAS detector experienced one bunch crossing every 25 ns (40 MHz), with an average of 33 primary vertices per bunch crossing. This results in an average interaction rate of 825 GHz. The ATLAS *Trigger and Data Acquisition* system (TDAQ) is responsible for reducing this figure first to 100 kHz and then to 1 kHz for storage. This reduction factor of about 40 000 cannot be

random and must select the most likely events to be appropriate for current or future physics analyses. The Trigger system is composed of a hardware based *Level 1* (L1) trigger and a software based *High Level Trigger* (HLT).

Level 1 Trigger

The L1 trigger is composed of custom electronics that operates at a maximum frequency of 400 kHz. It utilises the detector systems with the fastest response time (the calorimeters and Type II muon chambers) to provide information on how to reduce the total bunch crossing rate from 40 MHz to 100 kHz. Trigger towers in the calorimeters have a separate electronics path to the read-out channels and produce signals with a granularity of $\Delta\eta \times \Delta\phi = 0.1 \times 0.1$ and a precision of about 1 GeV. These signals are used to create L1 objects from jets, electromagnetic clusters, MET, and hadronic τ decays. In the Muon Spectrometer, the RPC and TGC chambers are used to trigger on muon p_T thresholds. Signals that pass the L1 decision are then used to define *regions of interest* (ROI) from the detector regions from whence they originated, and are passed on to the HLT.

High Level Trigger

The HLT takes the ROIs provided by the L1 trigger and combines the full granularity of the calorimeters with tracking information from the ID in these regions, allowing for particle identification. Reconstruction of these particles can then allow for the HLT to make its final decision on whether the event is of interest to offline physics analyses. These events are then sent to the CERN Data Centre for storage and a first pass on full event reconstruction. The HLT takes the 100 kHz rate passed from L1 and outputs to storage at a rate of 1 kHz.

Data Storage and Processing

Output from the HLT is then passed to the CERN Data Centre (on-site in Geneva), which functions as Tier-0 for the *Worldwide LHC Computing Grid* (WLCG). The WLCG is a distributed computing infrastructure that is arranged in tiers and allows for near real-time access to LHC data and analysis tools for collaboration members [24]. Tier-0 is responsible for the safe-keeping of the first

copy of raw data, provides a first pass on full event reconstruction, and reprocesses data during LHC down-time. Reconstruction of the raw data creates the *event summary data* (ESD) and *analysis object data* (AOD). AODs contain only the reconstructed physics objects while the corresponding ESD contains both the physics objects and all reconstructed quantities measured within the detector. Tier-0 is also responsible for the distribution of these reconstruction outputs along with raw data to the Tier-1 computing sites.

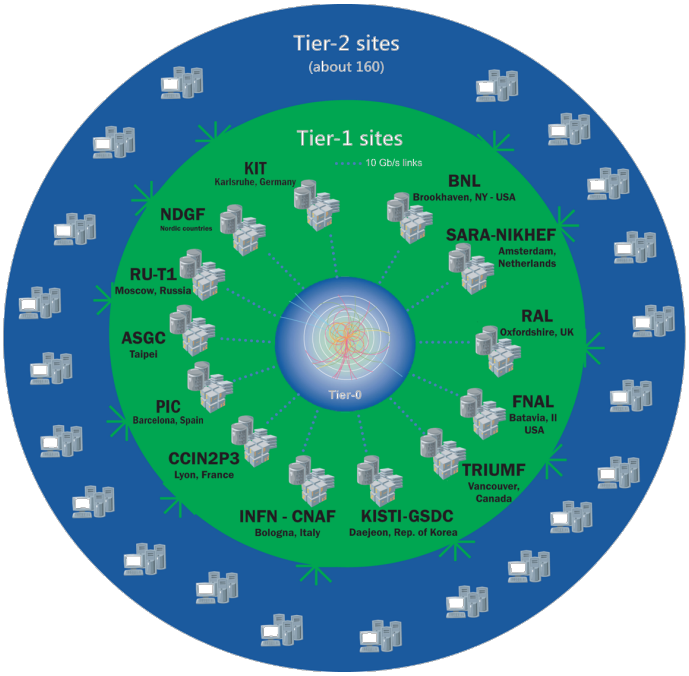

Figure 3.15 *The tier structure of the Worldwide LHC Computing Grid, including the names and locations of the 13 Tier-1 sites [24].*

The 13 Tier-1 sites around the world are centres with sufficient storage and computational capacity with full-time support for the Grid. They keep a proportional share of both raw and reconstructed data and are responsible for the large-scale reprocessing of data, storage of the output, and distribution of data to Tier-2 sites. They also are charged with the safe-keeping of simulation data.

Typically housed at individual scientific institutes, Tier-2 sites are where a significant proportion of the physics analyses on LHC data are performed. They also take a proportional share of Monte Carlo simulated event production and reconstruction. They number approximately 160 sites across the world.

Finally Tier-3 sites are those facilities utilised by individual scientists to access data and perform analyses. They connect to the WLCG but there is no

formal engagement between Tier-3 and the Grid. Figure 3.15 summarises the tier structure of the distributed computing infrastructure as maintained by the WLCG.

3.3 Reconstruction and Particle Identification

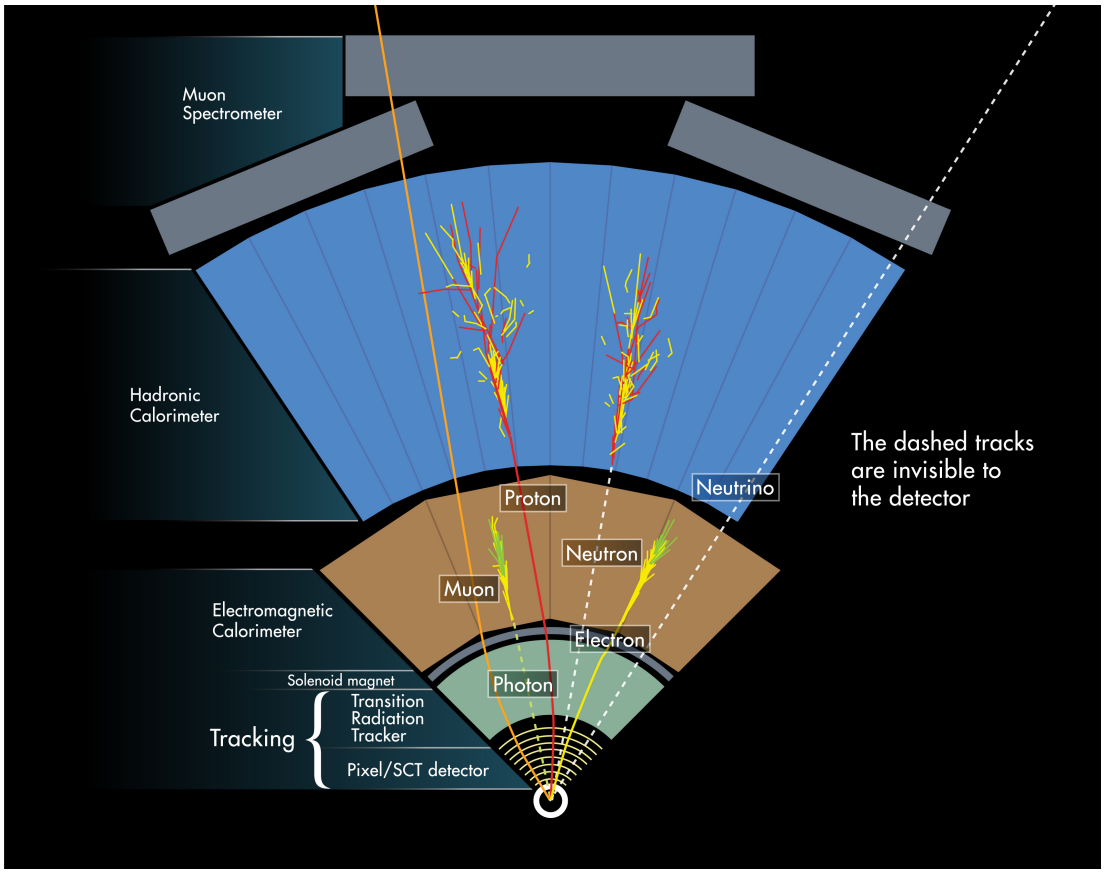

Figure 3.16 *A representation how different particles interact with the ATLAS sub-detector systems [25].*

Different particles produced by collisions in the LHC leave different signals in the ATLAS sub-detectors. Hits in the Inner Detector and Muon Spectrometer, and energy deposits in cells of the Electromagnetic and Hadronic Calorimeters can be used to identify muons from electrons, photons from neutrons, etc. Figure 3.16 depicts examples of how different particles interact with the sub-detector layers in ways that can be used to identify the particle type. Algorithms are used to reconstruct the various hits and energy deposits into physics objects: identifying the particle type, assigning its measured characteristics, and minimising its misclassification.

3.3.1 Tracks

Tracks are reconstructed from hits left by a charged particle throughout the layers of the Inner Detector. A reconstruction algorithm must identify all the hits that originated from one particular particle with as little misidentification as possible. Any hits included that did not originate from the particle in question will lead to a suboptimal measurement, or even to a miscategorisation of that particle.

Although there are several track reconstruction methods used by ATLAS, the *inside-out* algorithm is the most frequently utilised [26]. The algorithm proceeds as follows:

1. **Formation of space-points:** initially, clusters of hits are identified in the Pixel Detector and the SCT, along with drift circles in the TRT. These clusters and drift circles are then converted to three dimensional space-points.

2. **Track finding seeded by space-points:** a minimum of three points in space are required to extrapolate the helical path travelled by a charged particle in the ID. As such, sets of three space-points formed by the previous step are considered to form a seed. Seeds are tagged as Pixel-only, SCT-only, or as a Mixed seed. They must then satisfy transverse momentum and impact parameter resolution cuts before being required to match a fourth space-point deemed compatible with the suggested particle's trajectory in the detector, as estimated from the seed. Track candidates are then completed with all compatible space-points via a combinatorial Kalman filter [27].

3. **Ambiguity solving:** to bias against tracks formed with spurious hits, termed as *fakes*, the track candidates are ranked by a score. Positive scores are applied for those containing unique hit measurements and improved track fit quality, while negative scores are assigned for missing hits and hits that are shared between multiple tracks. The candidates not passing basic quality criteria are then rejected.

4. **TRT extension:** finally, the track candidates passing the ambiguity solver are extended to compatible space-points from drift circles in the TRT. These TRT extended tracks are refitted to improve momentum resolution.

3.3.2 Vertices

The production origin of particles are referred to as their vertex and can only be extrapolated from reconstructed tracks. Primary vertices (PVs) are those found along the beam line produced by the initial proton interactions, while secondary vertices (SVs) are those caused by the subsequent decays of particles and are found displaced from the central axis. The reconstruction of vertices (*vertex finding*) is carried out at ATLAS by a process known as *finding through fitting*.

The region within the detector where all primary vertices from a single bunch crossing are found is known as the *luminous region* or *beam spot*. For tracks to be considered for PV reconstruction, they must satisfy some initial quality requirements. A seed position is then selected from a minimum of two compatible tracks passing the selection criteria and then the best vertex position is fitted using an iterative procedure that negatively weights less compatible tracks and recomputes the vertex position with each iteration. Tracks that are incompatible with the final position are removed from consideration and permitted for the determination of a different PV. This is then repeated until no further vertex can be fitted, or until there are no further tracks unassociated with a vertex. The position and width of the luminous region is also reconstructed to constrain the position resolution of vertices fitted using a small number of tracks [28].

Secondary vertices are primarily used for the flavour identification of jets and so only tracks inside a jet cone are considered for their reconstruction. The axis of the jet, PV position associated with the events from which it originated, and a list of tracks associated with it are compiled for identifying the SV. The algorithm then iteratively works to fit a single SV per jet from these inputs [29].

3.3.3 Muons

Muons can leave tracks in both the Inner Detector and the Muon Spectrometer, thus information from the individual sub-detectors can be combined to reconstruct them for their use in physics analyses. This allows for the identification and reconstruction of four different types of muon:

- **Combined (CB) muons:** compatible tracks that have been reconstructed in both the ID and MS independently of each other are combined in a global fit that utilises the hits from all sub-detectors to reconstruct CB muons.

These have the best identification and reconstruction efficiency of all muon types.

- **Segment-tagged (ST) muons:** at least one local track segment in the Muon System MDT or CSC chambers that can be associated to an extrapolated track in the Inner Detector can be used to reconstruct an ST muon.
- **Extrapolated muons (ME):** those muons that can only be reconstructed from an MS track that is loosely compatible with having originated from the IP are known as ME muons. The constraints to originating from the interaction point are not so stringent so as to allow for multiple scattering and energy loss from traversing detector material. ME muons allow for muon acceptance in the $2.5 \leq |\eta| \leq 2.7$ region.
- **Calorimeter-tagged (CT) muons:** energy deposits in the calorimeter that are compatible with a minimally-ionising particle and can be associated with a track from the Inner Detector are reconstructed and identified as CT muons. The reconstruction efficiency of these muons is the lowest of the four, but allow for their acceptance in regions of the detector without coverage by the Muon Spectrometer.

3.3.4 Topological Clusters

Electrons, photons, and jets are all reconstructed using *topological clusters*, or *topo-clusters*, formed from hits in the calorimeter with a method known as *4-2-0* topological cluster reconstruction. These topo-clusters are seeded by cells that registered a hit with energy measuring over four times that of the noise threshold in that cell. If neighbouring cells contain energy greater than two times their noise threshold, then the cluster is extended to these. If another layer of adjacent cells register hits of energy over their noise threshold, then these are also used in the creation of the topological cluster.

Topo-clusters can then be dynamically arranged into groups known as *superclusters* for the purpose of recovering low energy photons from electron bremsstrahlung interactions with the ID material, and associating electrons from converted photons during their reconstruction. The superclustering algorithm endeavours to locate and associate related secondary clusters (*satellite clusters*) to a primary cluster (*seed cluster*). The algorithm expands outwards from

a high energy deposition locale, including the surrounding shower into one dynamically sized cluster across multiple layers of the calorimeter. Figure 3.17 shows an example of a supercluster that has taken a seed electron topo-cluster and associated it with a satellite cluster from a photon emitted from that electron via bremsstrahlung radiation.

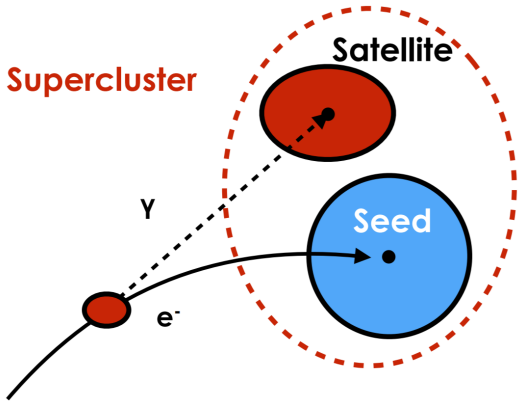

Figure 3.17 *An example supercluster including the energy deposits of a seed electron and those of a satellite photon cluster [30].*

3.3.5 Electrons and Photons

Reconstructing electrons and photons first requires the selection of topo-clusters to consider. A refit allowing for bremsstrahlung compatibility is then performed on Inner Detector tracks, matching them to the selected topo-clusters. Photon conversion vertices are also reconstructed and matched to the selected topo-clusters that they result in. Electron and photon superclustering algorithms then run in parallel, where topo-clusters are ordered by transverse momentum so that higher p_T seeds are only associated with satellite clusters of lower p_T. Reconstruction then proceeds to match tracks to electron superclusters and vertices to photon superclusters. As a single object might be reconstructed as both an electron and a photon, they are somewhat resolved by the following criteria:

- **Electron:** an object is defined as an electron if it consists of a supercluster built in the calorimeter and at least one track from the ID. The candidate cluster must be matched with a track comprised of at least two hits in the Pixel Detector and at least four in the SCT. A best fitting track from a

conversion vertex is considered to identify an electron as long as the hits from one of the tracks defining the vertex are solely from TRT hits.

- **Photon:** an object is defined as a converted photon if a supercluster can be matched to one or more conversion vertices that originate from the SCT. Unconverted photons are reconstructed if a supercluster cannot be matched with either tracks or conversion vertices.

- **Both:** if a candidate particle does not fall into the above categories then it may be reconstructed as both an electron and a photon instead of being discarded to maximise the reconstructed energy within the calorimeter. Individual physics analyses may then impose their own criteria on how to handle these objects.

3.3.6 Jets

Jets are objects defined as a cascade of particles caused by the hadronisation of quarks and gluons immediately after their production from the initial particle collision or within the detector. They are reconstructed from topo-clusters formed by energy deposits in cells of the calorimeter and used as inputs for the anti-k_t algorithm [31]. Two different distance parameters, R, are typically assigned according to different cases. Small-R jets use $R = 0.4$ and tend to represent quarks and gluons, while large-R jets with $R = 1.0$ usually represent hadronically decaying massive particles. The topo-clusters used as inputs to the anti-k_t algorithm can be calibrated at either the raw electromagnetic (EM) scale where the energy of the cluster is the sum of its constituent cell energies, or at the *local cell weighting* (LCW) scale. The LCW scale accounts for the differences between electromagnetic and hadronic interactions within the detector calorimeters, correcting a topo-cluster to the hadronic energy scale. The larger radius used for large-R jet reconstruction is useful to capture all the hadronic decay products from the initial particle into one jet [32].

3.3.7 Flavour Tagging

Dictating what flavour quark generated a jet is especially useful in many physics analyses. In particular to this thesis, top quarks are extremely short lived and do not form hadrons as other quarks do, requiring their reconstruction from decay

products. Since they decay in almost all cases by $t \to Wb$, the tagging of jets as originating from bottom quarks is necessary to identify the presence of top quarks in an event.

When bottom quarks are produced, they *do* hadronise to create b-hadrons. These typically have longer lifetimes than other hadrons (for example $\tau\left(\bar{B}_0(b\bar{d})\right)$ is around $1.5 \times 10^{-12}\,\mathrm{s}$) and result in a secondary vertex at a measurable distance ($\sim$3 mm) from the primary vertex from where the b-quark was produced. Additionally, decay products are emitted at large angles to the original bottom quark trajectory due to the relatively high mass of the b. These properties of b-quark decays are used in multivariable algorithms to assign b-tags to jets with a high probability of originating from bottom quarks. The power of a b-tagging algorithm at a certain *working point* (WP) is characterised by its ability to separate b-, c-, and light-jets when tested on simulated events. It is measured in its b-tagging efficiency ε_b, where efficiency is calculated as

$$\varepsilon_j = \frac{\text{Number of jets tagged as } j}{\text{Number of } j \text{ jets in training sample}}, \tag{3.11}$$

and in its rejection of c- and light-jets, where rejection is calculated as $1/\varepsilon_j$. Working points are defined by sets of selection criteria imposed on the result of the b-tagging algorithm to provide a particular ε_b. Four different WPs are defined at ATLAS, corresponding to 60, 70, 77 and 88 % b-jet tagging efficiency for simulated $t\bar{t}$ events [33].

3.3.8 Missing Transverse Energy

Reconstructing the *missing transverse energy* (MET) for an event at ATLAS is characterised by two contributions. Firstly from *hard-event* signals composed only of reconstructed particles and jets (known as hard objects), where these particles are electrons, photons, τ-leptons, and muons. The second contribution is from *soft-event* signals comprised of reconstructed charged particle tracks (soft signal) that are not associated with hard objects.

MET is reconstructed from the $p_{x(y)}$ components of the transverse momentum vectors ($\mathbf{p}_T$) of the hard objects and soft signals. The MET components $E^{\mathrm{miss}}_{x(y)}$ are given by

$$E_{x(y)}^{\text{miss}} = -\sum_{i \in \text{hard}} p_{x(y),i} - \sum_{j \in \text{soft}} p_{x(y),j}. \tag{3.12}$$

The following set of MET observables is then constructed:

$$\mathbf{E}_T^{\text{miss}} = \begin{bmatrix} E_x^{\text{miss}} \\ E_y^{\text{miss}} \end{bmatrix}, \tag{3.13}$$

$$E_T^{\text{miss}} = |\mathbf{E}_T^{\text{miss}}| = \sqrt{{E_x^{\text{miss}}}^2 + {E_y^{\text{miss}}}^2}, \tag{3.14}$$

$$\phi^{\text{miss}} = \arctan\left(E_y^{\text{miss}} / E_x^{\text{miss}}\right). \tag{3.15}$$

Here the MET is described entirely by the vector $\mathbf{E}_T^{\text{miss}}$ where the magnitude E_T^{miss} is the amount of missing energy in a direction ϕ^{miss} in the transverse plane of the detector, in terms of the azimuthal angle [34].

This chapter described the hardware of the LHC and the ATLAS detector and explained how they are used to produce high energy physics data. It was described how the signatures from various sub-detectors are reconstructed to identify physics objects for manipulation in analyses. Next, Chapter 4 describes how simulated event samples are produced to build statistical representations of physics models to compare with data produced at ATLAS for measurements of the underlying processes.

References

[10] Sarah Fields and Lexi Carver. 'Analyzing the LHC Magnet Quenches'. In: *Multiphysics Simulation: An IEEE Spectrum Insert 2017* (Oct. 2017), pp. 6–9.

[11] Oliver Sim Brüning et al. *LHC Design Report*. CERN Yellow Reports: Monographs. Geneva: CERN, 2004. DOI: 10.5170/CERN-2004-003-V-1.

[12] The ATLAS Collaboration et al. 'The ATLAS Experiment at the CERN Large Hadron Collider'. In: *JINST* 3 (2008). Also published by CERN Geneva in 2010, S08003. 437 p. DOI: 10.1088/1748-0221/3/08/S08003.

[13] The ALICE Collaboration. 'The ALICE experiment at the CERN LHC. A Large Ion Collider Experiment'. In: *JINST* 3 (2008), S08002. DOI: 10.1088/1748-0221/3/08/S08002.

[14] The LHCb Collaboration. 'The LHCb Detector at the LHC'. In: *JINST* 3.LHCb-DP-2008-001 (2008), S08005. DOI: 10.1088/1748-0221/3/08/S08005.

[15] The CMS Collaboration. 'The CMS experiment at the CERN LHC. The Compact Muon Solenoid experiment'. In: *JINST* 3 (2008), S08004. DOI: 10.1088/1748-0221/3/08/S08004.

[16] STFC. *CERN Accelerator Complex*. 2016. URL: https://stfc.ukri.org/research/particle-physics-and-particle-astrophysics/large-hadron-collider/cern-accelerator-complex/ (visited on 29/11/2019).

[17] J. Wenninger. 'LHC status and performance'. In: *PoS(CHARGED2018)001* 339 (Feb. 2019). DOI: 10.22323/1.339.0001.

[18] The ATLAS Collaboration. *LuminosityPublicResultsRun2*. 2019. URL: https://twiki.cern.ch/twiki/bin/view/AtlasPublic/LuminosityPublicResultsRun2 (visited on 04/12/2019).

[19] Izaak Neutelings. *TikZ.net - CMS coordinate system*. June 2017. URL: https://tikz.net/axis3d_cms/ (visited on 04/12/2021).

[20] Laurent Chevalier. 'Muon Detection'. In: ESIPAP 2015 - Module 1 - Physics of particle and astroparticle detectors (European Scientific Institute - Archamps, France). Feb. 2015. URL: https://indico.cern.ch/event/366272/contributions/1781565/.

[21] The ATLAS Collaboration. *Track Reconstruction Performance of the ATLAS Inner Detector at* $\sqrt{s} = 13$ *TeV*. Tech. rep. ATL-PHYS-PUB-2015-018. Geneva: CERN, July 2015. URL: https://cds.cern.ch/record/2037683.

[22] Christian Wolfgang Fabjan and F Gianotti. 'Calorimetry for Particle Physics'. In: *Rev. Mod. Phys.* 75.CERN-EP-2003-075 (Oct. 2003), 1243–1286. 96 p. URL: https://cds.cern.ch/record/692252.

[23] Heinrich J. Voelk and Konrad Bernloehr. 'Imaging Very High Energy Gamma-Ray Telescopes'. In: *Exper. Astron.* 25 (2009), pp. 173–191. DOI: 10.1007/s10686-009-9151-z. arXiv: 0812.4198 [astro-ph].

[24] CERN. *Worldwide LHC Computing Grid Tier Centres*. 2020. URL: https://wlcg-public.web.cern.ch/tier-centres (visited on 02/02/2020).

[25] Joao Pequenao and Paul Schaffner. 'A computer generated image representing how ATLAS detects particles'. Jan. 2013. URL: https://cds.cern.ch/record/1505342.

[26] Kyungeon Choi. *Tracking and Vertexing with the ATLAS Inner Detector in the LHC Run-2*. Tech. rep. ATL-PHYS-PROC-2017-075. Geneva: CERN, June 2017. DOI: 10.1007/978-981-13-1316-5_75.

[27] R Frühwirth. 'Application of Kalman filtering to track and vertex fitting'. In: *Nucl. Instrum. Methods Phys. Res., A* 262.HEPHY-PUB-503 (June 1987), 444. 19 p. URL: https://cds.cern.ch/record/178627.

[28] Federico Meloni. *Primary vertex reconstruction with the ATLAS detector*. Tech. rep. ATL-PHYS-PROC-2016-163. 12. Geneva: CERN, Oct. 2016. DOI: 10.1088/1748-0221/11/12/C12060.

[29] Sebastian Heer. *The secondary vertex finding algorithm with the ATLAS detector*. Tech. rep. ATL-PHYS-PROC-2017-195. Geneva: CERN, Oct. 2017. DOI: 10.22323/1.314.0762.

[30] The ATLAS Collaboration. *Electron and photon reconstruction and performance in ATLAS using a dynamical, topological cell clustering-based approach*. Tech. rep. ATL-PHYS-PUB-2017-022. Geneva: CERN, Dec. 2017. URL: https://cds.cern.ch/record/2298955.

[31] Matteo Cacciari, Gavin P Salam and Gregory Soyez. 'The anti-ktjet clustering algorithm'. In: *Journal of High Energy Physics* 2008.04 (Apr. 2008), pp. 063–063. DOI: 10.1088/1126-6708/2008/04/063.

[32] Steven Schramm. *ATLAS Jet Reconstruction, Calibration, and Tagging of Lorentz-boosted Objects*. Tech. rep. ATL-PHYS-PROC-2017-236. Geneva: CERN, Nov. 2017. URL: https://cds.cern.ch/record/2291608.

[33] The ATLAS Collaboration. 'Measurements of b-jet tagging efficiency with the ATLAS detector using $t\bar{t}$ events at $\sqrt{s} = 13$ TeV'. In: *JHEP* 08.arXiv:1805.01845 (May 2018), 089. 49 p. DOI: 10.1007/JHEP08(2018)089.

[34] The ATLAS Collaboration. 'Performance of missing transverse momentum reconstruction with the ATLAS detector using proton–proton collisions at $\sqrt{s} = 13$ TeV'. In: *The European Physical Journal C* 78.11 (Nov. 2018). ISSN: 1434-6052. DOI: 10.1140/epjc/s10052-018-6288-9.

Chapter 4

Monte Carlo Simulation

Monte Carlo simulation is required for each phase of a particle physics experiment: probing the capability of a detector concept, design of the detector, development of the reconstruction software, and analysis of the physics data [35]. The process uses random sampling and statistical modelling to estimate mathematical functions and to imitate the workings of complex systems. The general method of simulating a system plays out as follows [36]:

1. Model the system as a series of probability density functions (PDFs).
2. Randomly sample from these PDFs over the run of the simulation.
3. Compute required variables according to the physical model desired.

This allows for the emulation of the detector response to individual particles and when repeated over many samples, the output distribution of variables will match that of the modelled physical system. Analysis of collected data can then be compared with the results of simulation to determine the agreement of the model to reality.

4.1 ATLAS Monte Carlo Simulation Chain

Figure 4.1 gives an overview of how ATLAS simulates data. Algorithms and applications are denoted by square-cornered boxes, and their resultant persistent

data objects are within round-cornered boxes. Optional processes for pileup and event overlay are given dashed outlines.

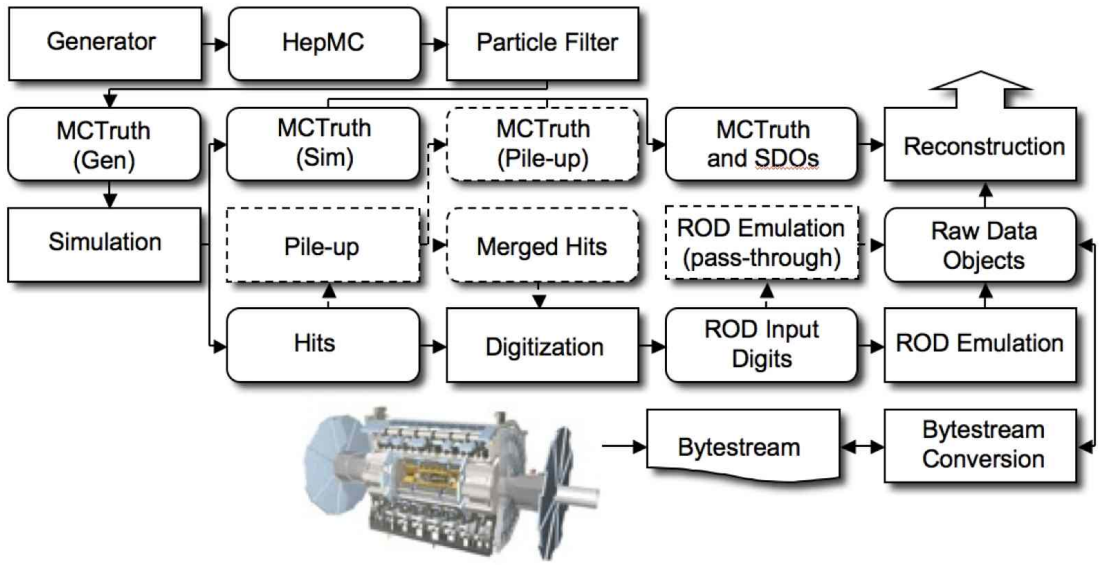

Figure 4.1 *Overview of the flow of ATLAS simulation software. The flow-chart starts with event generators in the top left corner through to reconstruction in the top right and also includes the real data path from detector to reconstruction [37].*

For *generation*, *simulation*, and *digitisation*, *truth* information is retained for every event. At generation, truth is a record of the interactions from the generator, including incoming and outgoing particles. The information is stored for each particle regardless of whether it is passed to the simulation or not. For simulation jobs, only the truth and decay tracks for desired particles are retained. As an example, this information gives the locations of photon conversions in the Inner Detector and the resulting electron and positron tracks. For digitisation, *Simulated Data Objects* (SDOs) are made from the truth information. SDOs map particles in the simulation truth history to the hits recorded in the sensitive regions of the detector. This truth information is then processed further at *reconstruction* and can be used in simulated data analysis to measure the quality of reconstruction software [37].

The ATLAS simulation chain is split into these individual steps as it makes a more effective use of computing resources than to combine generation, simulation, and digitisation into one job, particularly for digitisation since pileup samples are used from pre-simulated banks of events. This helps validation of the software as each step can be examined individually. Event generation is normally quick to run and produces relatively small output files, and so can be run for thousands of events at once. Retaining the event files, rather than running the generation each

time, allows the same set of events to be run through different iterations of the simulation step, or through different configurations of the detector. Conversely, simulation is particularly slow and takes several minutes for each event using Geant4, thus simulation jobs are split into sets of 50 events or fewer. Finally, digitisation is normally set to run on around 1000 events to make it easier to manage the outputs by producing fewer RDO files [37, 38].

4.1.1 Event Generation

Each simulated event begins with a *physics event generator*. Input parameters are provided to the generator to specify the kinds of events to be modelled, such as the centre-of-mass energy and identity of the initial colliding particles. This step results in data objects that represent final state particles, analogous to how final state particles are created in high-energy collisions by the LHC. A filter can be given at production so that only desired events are retained, for example only leptonic decay or events with missing energy above a given threshold. This generator resolves prompt decays, such as to Z or W bosons, but keeps particles that are stable enough to be expected to reach a part of the detector. Detector geometry is not involved in the generation step other than to consider if the resulting particles can be stable with respect to reaching the detector. Each generated event dataset is assigned a run number and each event is given an event number that is ordered by that particular job. Run numbers for simulated sets come from job options and are used to imitate run numbers from real datasets [37, 38]. These data objects are stored in the *EVNT* data format as HepMC event records, although a tree of intermittent particles connecting the initial simulated collision to the final state objects is also included in the file by some event generators. The EVNT persistent data format typical file size is that in the order of tens of kilobytes per event stored, by far the smallest of the persistent formats.

Event generators base their computations for particle properties on theoretical and computational models (which could be the Standard Model or Beyond the Standard Model physics focussed) and are used to test the results against real measured data from the detector. However, some event generators apply some simplifications due to the mathematical complexity of the real physics processes occurring in the model or the conditions of collisions in the LHC. These approximations must be tuned to collected data and different tunings may exist

that tend to change over time. If the settings of an event generator are changed, all subsequent steps of the Monte Carlo production chain usually must be re-run.

Full event generators commonly used by ATLAS that include parton showering and fragmentation are PYTHIA, HERWIG, SHERPA, and HIJING [39].

4.1.2 Detector Simulation

The next Monte Carlo simulation step is to process how the interactions of the final state particles from the EVNT files would occur within the ATLAS detector. This detector simulation computes the particle decays, trajectories, and appropriate matter interactions within the ATLAS detector volume and ends when all considered particles have deposited enough energy to be left below a defined threshold, or have exited the detector volume. The output of this step is produced in the *HITS* persistent data format which contains the location and size of the resultant simulated energy deposits from the particles traversing the sub-detector systems. Each event in the HITS format contributes to an order of hundreds of kilobytes of storage space, and like the EVNT format, there is no corresponding data stream file format as they are purely simulation based.

There are a number of different detector simulation options developed by the ATLAS Collaboration. The most complete of which uses the *Geant4* toolkit and provides the most detailed computations of the particle interactions whilst also currently being the most commonly utilised method. The other options are fast simulation methods: namely *Fatras* for fast tracking simulation in the Inner Detector, and *FastCaloSim* for parametrised shower development simulation in the calorimeters. These different methods are combined to form setups capable of simulating the entire ATLAS detector. These include: a full simulation using Geant4 for all detector systems, *AtlFast-II* which combines FastCaloSim covering the calorimeters and Geant4 for the ID and MS, and *AtlFast-IIF* combining Fatras in the ID with FastCaloSim in the calorimeters and Geant4 for muons throughout the whole detector for an even faster simulation of particles traversing the ATLAS volume.

4.1.3 Digitisation

The HITS files are then passed to digitisation to simulate the electronic response of the detector, where the result is converted to the corresponding format of the real particle data that is read out by the ATLAS DAQ. This output is the *RAW Data Objects* (RDO) persistent data format.

The digitisation step transforms the simulated energy deposits from the interactions of particles with the detector material into quantities such as the magnitude and time-stamp of charge collected by readout electronics, or current measurements in photomultiplier tubes. Just as data from the detector does not contain any information on what particles caused any specific energy deposit, the RDO files also omit this knowledge (instead it is included by the truth record in the SDO format). The corresponding data output from the real detector is produced in the *ByteStream* (BS) format and includes the same level of information as that in RDO files. As such it is possible to map BS objects to RDO and convert files between the two formats.

Event pile-up can also be included with simulated signal events during this step. RAW Data Objects from minimum bias events are merged with those from the simulated signal event, where the minimum bias samples can either be pre-simulated and digitised, or can be recorded from minimum bias collisions by the detector.

RDO files typically require a few megabytes per event and are the last format in the Monte Carlo production chain to be specific to simulation. All subsequent analysis steps are carried out on simulated events and recorded data in the same fashion.

4.1.4 Reconstruction

The reconstruction step is performed on RDO files in the same way as physics objects are interpreted from real detector measurements via BS to identify and measure particle properties as described in Section 3.3. The results for this step when performed on either measured or simulated data are quantities required for subsequent physics analyses where the reconstructed information is stored in the *Event Summary Data* (ESD) format. ESD files store the physics objects derived from RDO (simulated) or BS (recorded) detector hits, but contain additional

truth about the event information when created from simulation. As well as the physics objects, ESD files also contain data collections specific to the sub-detectors and are typically a few megabytes of storage per event as a result of the large amount of information maintained by the format.

ESD files are normally converted to the derivative *Executable Analysis Object Data* (xAOD) format for manipulation in ATLAS physics analyses as they are typical of a much more wieldy file size that can be read in standard ATLAS user environments. The xAOD format contains physics objects as individual collections for a number of identified particle types, and usually does not contain the detailed sub-detector information. Consequently, xAOD files have a significantly smaller size of a few hundred kilobytes per event.

4.2 Full and Fast Detector Simulation

The motivation for the development and use of fast simulation techniques stems from the time taken for Geant4 (the most accurate ATLAS detector simulation) to simulate particles of different energies, which can be as high as a few minutes per event [40]. Geant4 uses more than 90 % of its simulation time to develop the particle showers generated from interactions with the dense calorimeter material [41]. Higher energy initial particles are more of a concern: increasing the number of secondary particles in the shower that require propagation and consequently increasing simulation time. Reducing this time requirement for simulating large numbers of high energy particles is of great importance to such physics analyses and studies that need high statistic samples for comparison. The following citation gives a more comprehensive description of ATLAS detector simulation times [37].

This section gives an overview and description of the operating principles of the full Geant4 detector simulation, as well as the Fatras and FastCaloSim sub-detector specific fast simulation packages. The following Chapter 5 gives detail on the current upgrade under development for FastCaloSim, as relevant to the work presented by this thesis.

4.2.1 Geant4

Geant4 [42] (**GE**ometry **AN**d **T**racking 4), as produced and developed by the collaboration of the same name [43], is one of the most widely used packages for the simulation of particle interactions with matter. It finds many applications in high energy physics experiments, radiation detection, medical science, and space physics projects. The toolkit is capable of simulating the interactions of a large range of particle types with a wealth of different materials for a wide span of energy regimes. Geant4 is based on a number of different physical models that describe particle-matter interactions that can be configured with a physics list. The toolkit allows for application specific geometric descriptions of the materials in a simulated detector and also propagates the decays of any unstable particles.

A number of parameters are provided by Geant4 to allow for the configuration of the simulation job to be run. Along with the aforementioned physics lists, quantities such as the stepping size (the iterative distance that the toolkit develops the simulated scenario over) and the simulated physics effects can be tuned to affect the use-case, accuracy, and computing performance of the simulation.

Due to its long period of development since release in 1998, the Geant4 toolkit has become a highly validated, accurate, and sophisticated simulation for a broad range of particle physics experiments. Consequently it is the principal detector simulation used by ATLAS, where it is commonly referred to as *full* simulation. However, this level of comprehension comes at the price of a huge demand for computing resources to process the number of simulated events required by the increasing luminosity of data utilised by ATLAS physics analyses. As a result, fast simulation solutions have been implemented to work alongside Geant4 and aid in the production of the unprecedentedly large simulated datasets used in such analyses.

4.2.2 Fatras

Fatras [44] (**Fa**st ATLAS **Tra**ck **S**imulation) is a fast detector simulation package designed for simulating particle interactions with the ATLAS Inner Detector. Particle tracks are simulated using the standard reconstruction tools, but use a simplified *reconstruction geometry* in place of the more detailed Geant4 detector

geometry description, as shown in Figure 4.2. This reconstruction geometry broadly describes the ID material as a series of thin and discrete layers of *averaged materials* that are arranged to impart the overall effects of the real ID materials onto traversing simulated particles. Particle interactions with the averaged materials are computed either by parametrised algorithms or by accessing specific routines from the Geant4 library. When using Geant4 routines, the average material parameters are converted to the closest matching existing material beforehand.

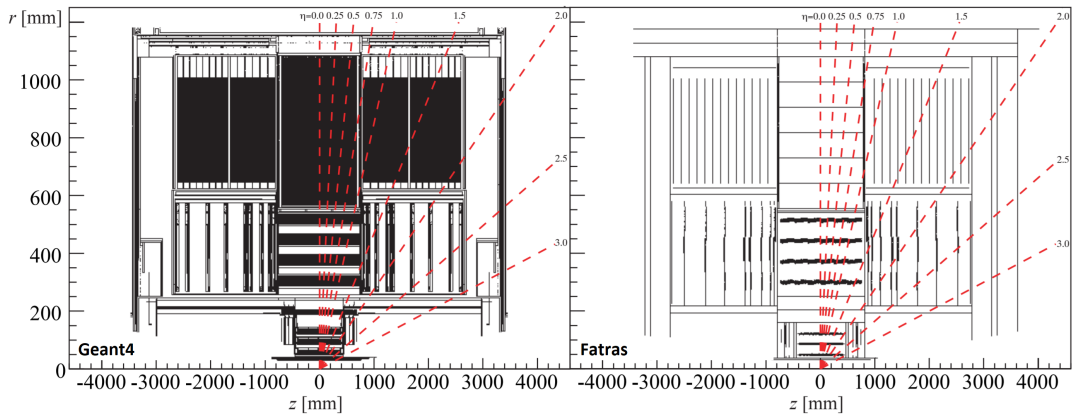

Figure 4.2 *Material hit map in the r–z plane of the Inner Detector created with the full Geant4 simulation and the simplified reconstruction geometry of Fatras [45].*

Compared to Geant4, Fatras saves on computation time by spending less resources on the creation of secondary particles during the material interactions. As a result, Fatras can simulate the ATLAS Inner Detector faster by about a factor of 10 when compared to Geant4, but at the price of a less accurate description of processes as they would occur in the physical detector.

4.2.3 FastCaloSim

FastCaloSim [41] (**Fast Calo**rimeter **Sim**ulation) is a parametrised fast simulation of the particle energy response and distribution in the ATLAS calorimeter system. There is an upgrade to this package in the advanced stages of development to be used for bulk production in Run 3 [46], but the underlying operation principles are broadly the same as for the legacy version that is described here. Chapter 5 details the major feature changes of the new FastCaloSim version, as relevant to this thesis.

FastCaloSim is based on a library of parametrised *probability density functions* (PDFs) created from the Geant4 simulation of single particles propagated through the calorimeters. To reduce complexity, the generated particle types are only electrons and photons (representing electromagnetic showers), and charged pions (representing hadronic showers), produced in a fine grid of energy and η. In the FastCaloSim simulation step, the closest fitting parametrisation is loaded from the library and the particle response (such as deposited energy or energy density about the shower axis) is randomly sampled from the PDFs.

The FastCaloSim parametrisations are divided into the lateral and longitudinal directions of shower development. For *longitudinal shower development*, the energy deposited in each layer of the calorimeter is determined. The energy distribution in each calorimeter layer is stored in 2D histograms against 10 bins of the shower depth (distance of the energy deposit from the front face of the calorimeter). The correlations of the energy deposits between the layers are also stored in correlation matrices. For *lateral shower development*, the energy density about the shower axis is modelled with a radially symmetric third order polynomial function. This function is subsequently modified to accommodate asymmetries produced by showers from particles not travelling perpendicularly to the calorimeter surface. While this allows legacy FastCaloSim to adequately model the average shower shape, it has problems describing the sub-structure of jets, rendering it inappropriate for analyses that require the selection of boosted objects [47]. The FastCaloSim V2 upgrade significantly improves on this, as covered in Chapter 5.

Legacy FastCaloSim has been used widely and successfully by the ATLAS Collaboration for Run 2 Monte Carlo production campaigns in the AtlFast-II and AtlFast-IIF modes [38]. A comparison for the simulation time (averaged over 250 events) for full and fast simulation modes is given in Table 4.1. As can be seen, legacy FastCaloSim reduces calorimeter simulation time by an order of magnitude over Geant4 (AtlFast-II), while Fatras provides an additional factor of 10 reduction (AtlFast-IIF).

This chapter gave a overview of the production of simulated event samples for physics analyses at ATLAS. The differences between full and fast detector simulation were summarised, and the importance of high quality fast simulation toolkits was emphasised. It was highlighted how Geant4 spends the longest CPU times on showering particles in the calorimeters, and how FastCaloSim is used as a critical alternative. Chapter 5 gives a more detailed overview of the

Table 4.1 *Simulation times of a few physics processes in seconds, obtained using full and fast simulation modes, and averaged over 250 events [37].*

Process	**Geant4** [s]	**ATLFAST-II** [s]	**ATLFAST-IIF**[s]
Minimum Bias	551	31.2	2.13
$t\bar{t}$	1990	101	7.41
Jets	2640	93.6	7.68
Photon + Jets	2850	71.4	5.67
$W \to e\nu$	1150	57.0	4.09
$W \to \mu\nu$	1030	55.1	4.13

FastCaloSim V2 upgrade, and illustrates how the accordion structure of the LAr calorimeters is emulated in the new toolkit version.

References

[35] G Weidenspointner M G Pia. 'Monte Carlo Simulation for Particle Detectors'. In: *CERN Council Open Symposium on European Strategy for Particle Physics* (2012). arXiv: 1208.0047 [comp-ph].

[36] RL Harrison. 'Introduction to Monte Carlo Simulation'. In: *AIP Conference Proceedings* 1204 (2010), pp. 17–21.

[37] The ATLAS Collaboration. 'The ATLAS Simulation Infrastructure'. In: *European Physics Journal C* 70 (2010), pp. 823–874. arXiv: 1005.4568 [ins-det].

[38] Jana Schaarschmidt. *The new ATLAS Fast Calorimeter Simulation*. Tech. rep. ATL-SOFT-PROC-2017-005. Geneva: CERN, Jan. 2017. URL: https://cds.cern.ch/record/2240206.

[39] C Ay et al. 'Monte Carlo generators in ATLAS software'. In: *Journal of Physics: Conference Series* 219.3 (Apr. 2010), p. 032001. DOI: 10.1088/1742-6596/219/3/032001.

[40] Elmar Ritsch. 'ATLAS Detector Simulation in the Integrated Simulation Framework applied to the W Boson Mass Measurement'. Presented 27 Feb 2015. Dec. 2014. URL: https://cds.cern.ch/record/2221649.

[41] ATLAS Collaboration et al. *The simulation principle and performance of the ATLAS fast calorimeter simulation FastCaloSim*. Tech. rep. ATL-PHYS-PUB-2010-013. Geneva: CERN, Oct. 2010. URL: https://cds.cern.ch/record/1300517.

[42] The Geant4 Collaboration. 'Geant4 – a simulation toolkit'. In: *Nuclear Instruments and Methods in Physics Research Section A: Accelerators, Spectrometers, Detectors and Associated Equipment* 506.3 (2003), pp. 250–303. ISSN: 0168-9002. DOI: 10.1016/S0168-9002(03)01368-8.

[43] The Geant4 Collaboration. *Geant4: A Simulation Toolkit*. 2020. URL: https://www.geant4.org/geant4/ (visited on 17/04/2020).

[44] K Edmonds et al. *The Fast ATLAS Track Simulation (FATRAS)*. Tech. rep. ATL-SOFT-PUB-2008-001. ATL-COM-SOFT-2008-002. Geneva: CERN, Mar. 2008. URL: https://cds.cern.ch/record/1091969.

[45] A Salzburger, S Todorova and M Wolter. *The ATLAS Tracking Geometry Description*. Tech. rep. ATL-SOFT-PUB-2007-004. ATL-COM-SOFT-2007-009. Geneva: CERN, June 2007. URL: https://cds.cern.ch/record/1038098.

[46] Hasib Ahmed. 'Fast Simulation in ATLAS'. WorkShop on Efficient Computing for High Energy Physics. 2020. URL: https://indico.ph.ed.ac.uk/event/66/contributions/826/.

[47] The ATLAS Collaboration. *Performance of the Fast ATLAS Tracking Simulation (FATRAS) and the ATLAS Fast Calorimeter Simulation (FastCaloSim) with single particles*. Tech. rep. ATL-SOFT-PUB-2014-001. Geneva: CERN, Mar. 2014. URL: https://cds.cern.ch/record/1669341.

Chapter 5

The New FastCaloSim

As mentioned in Section 4.2, the production of billions of accurately simulated Monte Carlo events required by ATLAS to match LHC datasets is becoming more difficult as the luminosity of the datasets increase. It is projected that 45 % of the total computing resources available to the ATLAS experiment will be required to simulate the propagation of particles through the detector material during the LHC Run 3 data-taking period.

The complex accordion geometry of the ATLAS electromagnetic calorimeter (as described in Section 3.2.4) makes the simulation of shower development particularly CPU intensive when using the Geant4 toolkit (Section 4.2.1). In fact, around 80–90 % of the total simulation time used by ATLAS is devoted to modelling this shower development [37]. Thus the first version of FastCaloSim (Section 4.2.3) was developed and employed to obtain a fast detector simulation of the calorimeter systems using parametrised showers. During Run 1 and Run 2, FastCaloSim has been utilised to produce around 35 billion simulated events out of the 52 billion used in physics analyses.

The legacy version of FastCaloSim is known to have limitations however. Most notable of which is the poor performance in modelling the substructure of jets. Consequently, a new version of the simulation, *FastCaloSim V2*, has been developed with the same CPU performance as its legacy version, but with improved accuracy in matching full Geant4 simulation. FastCaloSim V2 has been deployed by the ATLAS collaboration to resimulate 7 billion events for Run 2 physics analyses, and is scheduled to run as the default calorimeter simulation for Run 3 and beyond, only employing Geant4 if an analysis group proves a

need for full simulation. Further information on FastCaloSim V2 and its role in the new ATLAS fast simulation mode, *AtlFast3*, can be found in this cited publication [48].

5.1 FastCaloSim V2 Overview

The mechanism underpinning FastCaloSim V2 again utilises a parametrisation of the calorimeter response to simulate and deposit the energy of particle showers in a single step. This results in a constant simulation time regardless of the energy or the number of particles entering the calorimeter volume. This underlying parametrisation is built from single particles simulated using Geant4 to model the particle shower developments in the ATLAS electromagnetic and hadronic calorimeters.

FastCaloSim V2 is designed to simulate particle showers in such a way that no significant deviations from Geant4 simulation can be rendered using the ATLAS physics object reconstruction tools. This includes electron, photon, and tau identification and reconstruction, as well as jet reconstruction and clustering. The fast simulation of calorimeter showers can be factorised in several aspects: the total shower energy, the proportion of energy deposited in each calorimeter layer, the average lateral shower development within a layer, and the uncorrelated energy fluctuations in individual showers when compared to average showers. The energy deposited in the calorimeter by a particle is proportional to its kinetic energy (E_{kin}) and is the energy that is used for parametrisation unless otherwise specified. The E_{kin} is defined as the total energy of the particle minus its mass. For anti-protons and anti-neutrons, the mass energy is added instead of being subtracted as their annihilation in the calorimeter volume results in additional deposited energy.

FastCaloSim can provide the simulation of photons, electrons, jets, and tau particles: approximately simulating how much energy these particles deposit in total, and how that energy is distributed between the calorimeter layers. The average lateral spread of energy deposits is a key consideration for FastCaloSim V2, due to how critical this aspect of shower development is in the reconstruction and identification of physics objects. A simplified calorimeter cell geometry is utilised to decrease simulation time, in which each cell is generalised as a cuboid and is assigned to a specific sampling layer. These cuboid cell coordinates span either:

- η, ϕ, and r for the layers in the detector barrel,
- η, ϕ, and z for the layers in the detector end-caps within $|\eta| < 3.2$,
- or x, y, and z for the forward calorimeter layers.

For reference, a summary of the ATLAS calorimeter sampling layers and their pseudorapidity coverages are given in Table 5.1. Since this geometry is too simplistic to include details such as the accordion structure of the absorbers in the liquid argon calorimeters, these effects on the development of particle showers must be emulated (see Section 5.2). The improved FastCaloSim V2 simulation of the average energy distribution of showers, and the new capability to emulate the accordion structure of LAr cells allows for greater particle reconstruction and identification efficiencies.

Table 5.1 *The ATLAS calorimeter sampling layers and their pseudorapidity coverages.*

Calorimeter Sub-System	**Module**	**η-Coverage**	**Sampling Layers**
Electromagnetic Calorimeter	EMB	$0 < \|\eta\| < 1.5$	PreSamplerB EMB1 EMB2 EMB3
	EMEC	$1.5 < \|\eta\| < 3.2$	PreSamplerE EME1 EME2 EME3
Hadronic Calorimeter	Tile Barrel	$0 < \|\eta\| < 1.0$	TileBar0 TileBar1 TileBar2
	Tile Gap	$1.0 < \|\eta\| < 1.6$	TileGap1 TileGap2 TileGap3
	Tile Extended Barrel	$0.8 < \|\eta\| < 1.7$	TileExt0 TileExt1 TileExt2
	HEC	$1.5 < \|\eta\| < 3.2$	HEC0 HEC1 HEC2 HEC3
Forward Calorimeter	FCal	$3.1 < \|\eta\| < 4.9$	FCal0 FCal1 FCal2

Fluctuations also play an important role in the calorimeter simulation. The simulation of independent and uncorrelated energy fluctuations in calorimeter cells for individual showers with respect to average showers are required for an

accurate description of electrons and photons of all energies. A correct modelling of the fluctuations is crucial for hadrons, where at low energy the fluctuations in the lateral energy distribution are dominated by sampling fluctuations, noise and additional proton-proton interactions.

5.1.1 Geant4 Reference Samples

The calorimeter parametrisations comprising FastCaloSim V2 were derived from reference samples simulated with Geant4 version 10.1.3 [43] and using the FTFP_BERT_ATL physics list. The reference samples are single particle events with travel directions congruous with the interaction point of the ATLAS detector, but produced at the calorimeter surface so as not to waste computing resources on particles that would not be viable for the parametrisations. Specifically, the single particles were generated to originate on a cylinder of dimensions $r = 1148\,\text{mm}$ and $z = 3550\,\text{mm}$. This cylinder was centred on the interaction point and positioned just outside of the TRT to also include the effects of the cryostat and solenoid material on the propagation of the particles.

Other than the differences introduced from electromagnetic components and hadronic components (see Section 3.2.4), the development of showers is sufficiently independent of the initial particle that the reference samples can be simplified. The electromagnetic shower parametrisations were built from photons (γ) and electrons ($e^{\pm}$), whilst charged pions ($\pi^{\pm}$) were used for hadronic showers. To develop the lateral shower shape parametrisations, Geant4 was configured to use smaller than usual iterative development steps to provide greater detail of the spatial position of the energy deposits, or *hits*, of the shower.

The reference sample particles were produced with a uniform distribution in azimuthal angle, and with both positive and negative pseudorapidity in 100 uniform slices up to $|\eta| = 5$. This exceeds the forward boundary of the calorimeters by a small margin to include particles that interact minimally before penetrating the calorimeter volume. For every η-slice, 17 energy samples for each single particle type were produced: starting at a minimum of 64 MeV, with each subsequent sample doubling in energy, up to 4 TeV ($64\,\text{MeV}\times 2^{16}$). 10 000 events were produced for the first 13 samples with energies up to 256 GeV ($64\,\text{MeV}\times 2^{12}$). As Geant4 simulation time increases with initial particle energy, the number of sample events was decreased for successively higher energies until reaching 1000 for the 4 TeV sample.

5.1.2 Longitudinal Energy Deposition

The longitudinal direction of a particle shower in the calorimeter concerns how much energy is deposited in each layer as the shower evolves. This energy per layer is dependent on the calorimeter depth that the incident particle initiates the shower and how much energy that particle began with. However, it is highly correlated between layers which makes the independent parametrisation of the response for each separate layer difficult. Here, a technique called *Principal Component Analysis* (PCA) [49] is used to classify showers from the reference samples described in Section 5.1.1 for each energy point, η-slice, and particle type. This performs a transformation on a set of variables to produce a new set of orthogonal and uncorrelated *principal components* [50]. The PCA transformation is enacted twice, where the *first PCA* classifies showers into *PCA bins*, and the *second PCA* is implemented on each of these bins to result in uncorrelated Gaussian distributions. These Gaussian distributions are then used by FastCaloSim to model the energy to be deposited per calorimeter layer for a simulated particle shower.

To prepare the PCA inputs for each Geant4 reference sample, the distribution of the energy fraction deposited in each calorimeter layer is determined, such as in Figure 5.1a. The cumulative distribution of this energy fraction is then taken as in Figure 5.1b, and subsequently transformed into Gaussian distributions using the inverse error function, as in Figure 5.1c. The first PCA is then performed on a matrix comprised of the Gaussian distributions from each layer, transforming the set of correlated energies into a set of linearly decorrelated principal components by means of an orthogonal transformation of the coordinate system. The principal components with the highest and second highest variance are now termed as the leading and sub-leading principal components respectively. The particle shower is then classified by dividing the principal component of the first PCA into bins of equal probability, including a bin for depositing zero energy. The leading principle component distribution for the first PCA in this example process is shown in Figure 5.1d, displaying the defined PCA bins.

The same method is then used to transform the total energy and energy fractions in each bin of the first PCA principal component into Gaussian distributions before enacting a second PCA. The second PCA only considers the events in the bin from the first PCA that it is being performed on, but otherwise is processed in the same way to remove remaining correlations. The mean and *root mean square*

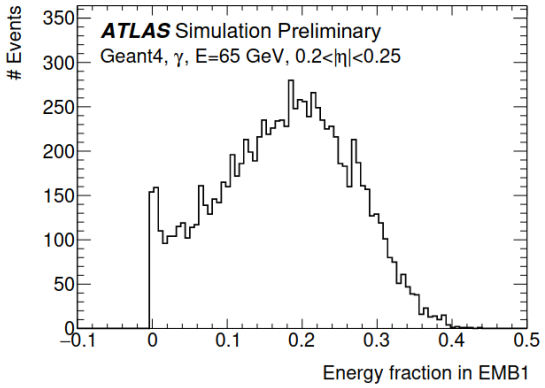

(a) *Distribution of energy fractions in EMB1.*

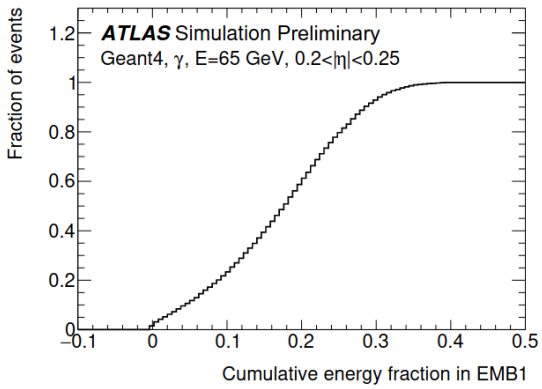

(b) *Cumulative distribution of energy fractions in EMB1.*

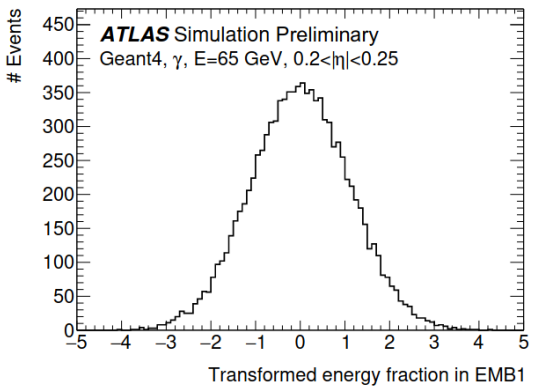

(c) *Gaussian transformed distribution of energy fractions in EMB1.*

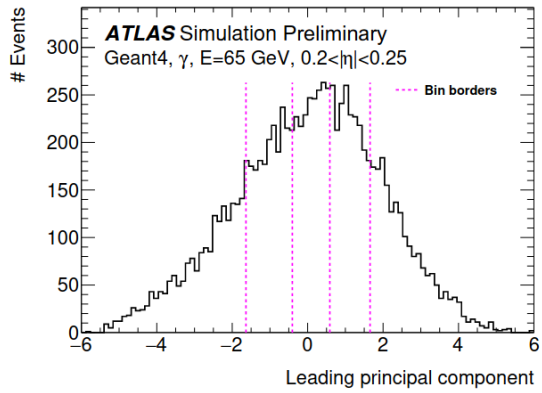

(d) *Bin definitions in the leading principle component distribution.*

Figure 5.1 *The steps taken in performing the first PCA transformation for 65 GeV photons in the EMB1 sampling layer for $0.20 < |\eta| < 0.25$ [48].*

(RMS) of the resulting decorrelated Gaussian distributions, PCA matrices, PCA bin probabilities and inverse cumulative distributions are all stored and used in FastCaloSim V2. To simulate a particle shower, the described PCA chain can now be carried out in reverse:

1. Select a PCA bin using a random number generated from a distribution of the PCA bin probabilities.

2. Generate random numbers from the uncorrelated Gaussian distributions in the selected PCA bin.

3. Rotate these numbers using the inverse second PCA matrix to correlate them.

4. Map the correlated random numbers back to the total energy and energy fractions deposited in each layer using the error function and the inverse cumulative distributions.

5.1.3 Lateral Shower Shape

The localised energy deposits of the Geant4 reference samples are collected by layer into bins in the radial direction from the shower axis. Here, only layers with energy fractions greater than 0.1 %, referred to as *relevant layers*, are considered in the parametrisation. Relevant layers are determined for each sample independently.

The pseudorapidity and azimuthal angle coordinates of hits in relevant layers, η^{hit} and ϕ^{hit}, are derived in respect to the extrapolated position of the initial particle in that layer, η^{extr} and ϕ^{extr}. This extrapolated position is determined from the initial momentum of the particle from when it enters the calorimeter volume, and is propagated through the layers while taking the detector magnetic field into account if the particle is charged. The relative angular coordinates of the showers, $\Delta\eta$ and $\Delta\phi$, are shown in Equation 5.1. The coordinates of the calorimeter cell where the hit is located, z_{cell} and r_{cell}, are also used to calculate the relative hit coordinates in millimetre units, $\Delta\eta^{\text{mm}}$ and $\Delta\phi^{\text{mm}}$, as this gives a better description of the shower.

$$\begin{aligned} \Delta\eta &= \eta^{\text{hit}} - \eta^{\text{extr}}, \\ \Delta\phi &= \phi^{\text{hit}} - \phi^{\text{extr}}, \\ \Delta\eta^{\text{mm}} &= \Delta\eta \times \eta_{\text{jacobi}} \times \sqrt{r_{\text{cell}}^2 + z_{\text{cell}}^2}, \\ \Delta\phi^{\text{mm}} &= \Delta\phi \times r_{\text{cell}}, \end{aligned} \tag{5.1}$$

where $\eta_{\text{jacobi}} = 2\left|\frac{\exp(-\eta_{\text{extr}})}{1+\exp(-2\eta_{\text{extr}})}\right|$. These hit positions are then converted to polar coordinates in Equation 5.2,

$$\begin{aligned} \Delta R^{\text{mm}} &= \sqrt{\left(\Delta\eta^{\text{mm}}\right)^2 + \left(\Delta\phi^{\text{mm}}\right)^2}, \\ \alpha &= \arctan2\left(\Delta\phi^{\text{mm}}, \Delta\eta^{\text{mm}}\right). \end{aligned} \tag{5.2}$$

These hit positions in polar coordinates are then grouped into bins of different size to exploit the shower symmetry in ϕ. A binning of 1 mm in the radial direction is used in the high-granularity EMB1 and EME1 layers while 5 mm is used in the rest. Along the angular direction, eight uniform bins are used in all relevant layers. The size of each resultant 3-dimensional hit volume is much smaller than the calorimeter cell dimensions.

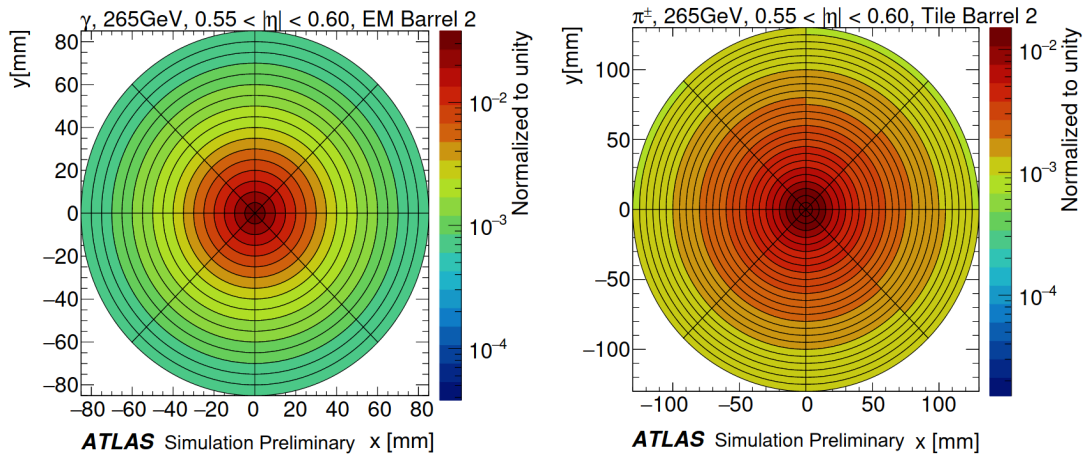

(a) *Photons in EMB2.* **(b)** *Pions in TileBar2.*

Figure 5.2 *Lateral shape parametrisation examples for 265 GeV photons and pions for 0.55 < |η| < 0.60 in the second layer of the electromagnetic and the tile barrel respectively. To better represent the core of the shower, these plots have a threshold at $\Delta R \sim 100$ mm [48].*

The lateral shower shape describes the distribution of energy deposits about the shower axis in each calorimeter layer. The specific parametrisation is derived for each relevant layer and in each PCA bin. The polar coordinates of hits defined in Equation 5.2 are used to parametrise the shower development. Only hits that constitute 99.5 % of the total energy in each PCA bin cumulatively along ΔR^{mm} are considered so as to exclude hits that are relatively far from the shower axis. For each layer, the shower shape distribution in each PCA bin is then normalised with the energy in that bin to derive the probability density function of the average lateral shower shape. The average shower profile for electromagnetic showers in EMB2, and for hadronic showers in TileBar2 are depicted in Figure 5.2. As the shower shape is demonstrated to be symmetric in $\Delta\phi^{\text{mm}}$, the storage size of these histograms describing the lateral shower parametrisation is reduced by only storing the $|\Delta\phi^{\text{mm}}|$ coordinates for $0 \leq \alpha \leq \pi$.

5.1.4 Simulating Hits

FastCaloSim V2 uses the average shower shape as a *probability density function* (PDF) to randomly sample hits to map to calorimeter cells using the simplified geometry description. For particles that are not simulated to enter calorimeter cells perpendicularly, the generated hit positions are altered to account for this. The energies of hits are assigned as described in the following sections and then the total energy of the hits are normalised so the sum corresponds with the determined simulated energy to be deposited in that layer, as described in Section 5.1.2.

Electrons and Photons

Changes in electron and photon shower shapes depend on the intrinsic energy resolution of the calorimeter system. This is due to the compact cascades of particles in an electromagnetic shower (see Figure 3.9). As a result, the number of hits to be assigned in each layer for a simulated electron or photon is determined by the particle energy and the energy resolution of that layer. For a simulated energy, E, the resolution of a calorimeter layer is defined as,

$$\frac{\sigma_E}{E} = \frac{a}{\sqrt{E/\text{GeV}}} \oplus c, \tag{5.3}$$

where a is the stochastic term, and c is the constant term. Table 5.2 lists the values for these terms for the different calorimeter subsystems.

Table 5.2 *The stochastic and constant terms of the different calorimeter systems as used to define their intrinsic energy resolution [51].*

Calorimeter System	**Stochastic Term (a) [%]**	**Constant Term (c) [%]**
EMB and EME	10.1	0.2
Tile Barrel	56.4	5.5
HEC	76.2	0.0
FCal	28.5	3.5

A Poisson distribution, Pois(λ), is constructed where λ is the mean of the distribution and is related to the energy resolution of a layer and the energy deposited in that layer by,

$$\lambda = \frac{1}{(\sigma_E/E)^2}. \tag{5.4}$$

A random number, N, is sampled from the Poisson distribution to give the number of hits in that layer, each of which possessing an equal energy of $E_{\text{hit}} = E/N$. The positions are determined by randomly sampling from the average lateral shower shape described in Section 5.1.3.

Hadrons

The procedure for generating hits for hadronic showers follows the same philosophy as for their electromagnetic counterparts. However, the stochastic and constant terms in each calorimeter layer vary by pseudorapidity and are much larger due to the intrinsically greater fluctuations of hadronic showers. A dedicated simulation of charged pions is used to derive these resolution terms, recording the total energy lost in both the active and the inactive volumes of the calorimeter. The ratio of the energy deposited in the active volumes of a layer to the total energy deposited in each layer is the sampling fraction, $f_{\text{sample}}(E)$, per shower and varies with the total energy deposited by the pion. The relative resolution, σ_E/E, of $f_{\text{sample}}(E)$ is fitted using Equation 5.3 for showers depositing more than 1 GeV in that layer, to derive the stochastic and constant terms for each pseudorapidity slice.

The stochastic terms, a, that were obtained from this fit range between 30–40 % for the electromagnetic calorimeters, 50–60 % for the Tile calorimeter, 60–80 % for the hadronic end-caps, and 80–100 % for the forward calorimeters. The constant terms, c, range between 1–10 % for all layers. Considering the changes in a and c for different pseudorapidities greatly improves the modelling of hadronic showers for most layers. However, EMB1 and EME1 are highly granular and the terms from Table 5.2 are used instead.

5.2 Hit to Cell Assignment

The sections of the ATLAS calorimeter based on liquid argon (LAr) technology use accordion-shaped electrodes that permeate the cells using an interleaved structure to avoid gaps in the azimuthal angle coverage, as described in Sec-

tion 3.2.4. This arrangement of material is not represented in the FastCaloSim V2 simplified geometry, and when unaddressed results in a notable bias in the ϕ position of energy deposits in the cells that they are assigned to. This bias is caused by a significant rate of hits being assigned to the wrong calorimeter cells when compared to how energy deposition is simulated using the full Geant4 geometry. To account for this effect while keeping the reduced simulation CPU time afforded by the simplified geometry, a method was developed that applies a small displacement in ϕ to each FastCaloSim hit before calling the geometry to assign it to a calorimeter cell. The net effect on a set of hits that is equally distributed in the ϕ direction of a cell (representing how the hits would be modelled using the unmodified FastCaloSim method) is to alter the distribution to match that produced by the full Geant4 geometry. Figure 5.3 displays the effect of these ϕ displacements on hits to correct for the lack of accordion structure, achieving substantially greater agreement with Geant4.

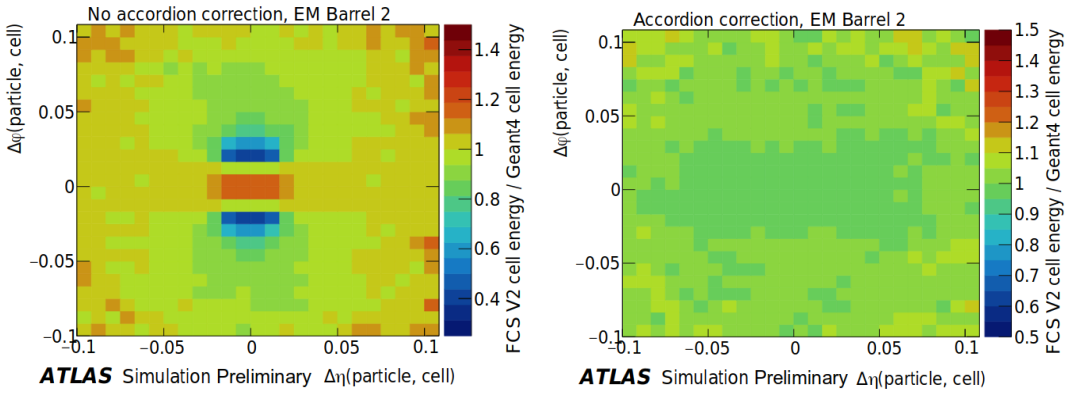

(a) *Before accordion correction in ϕ.* **(b)** *After accordion correction in ϕ.*

Figure 5.3 *Comparison of energy deposition of 65 GeV photons with $0.20 < |\eta| < 0.25$ for cells in the second electromagnetic barrel layer for FastCaloSim V2 and Geant4 before and after correcting for the simplified FastCaloSim geometry [48].*

5.2.1 Efficiency of Correct Cell Assignment

To determine how much a hit is to be displaced in ϕ, the differences in how the FastCaloSim and Geant4 geometries attribute hits to cells are required. A distribution of *'correct cell assignment efficiency'* can be constructed for cells in a calorimeter layer by analysing the hit positions of the simulated reference samples described in Section 5.1.1. The process begins by filling a histogram with the ϕ positions of the hits, ϕ_{hit}, in relation to the centre of their assigned FastCaloSim

cell, ϕ^0_{cell}. A second histogram is then constructed for the same calorimeter layer, but only filled by hits that are assigned to the same cell in the FastCaloSim geometry as in the Geant4 detector description, i.e. assigned to the *'correct cell'*. If $f_{\text{all}}(\Delta\phi_{\text{rel}})$ is the former distribution, and $f_{\text{matched}}(\Delta\phi_{\text{rel}})$ is the latter, then the efficiency of correct cell assignment, $\varepsilon_{\text{correct cell}}(\Delta\phi_{\text{rel}})$ is given by,

$$\varepsilon_{\text{correct cell}}(\Delta\phi_{\text{rel}}) = \frac{f_{\text{matched}}(\Delta\phi_{\text{rel}})}{f_{\text{all}}(\Delta\phi_{\text{rel}})}, \tag{5.5}$$

where $\Delta\phi_{\text{rel}} = \phi_{\text{hit}} - \phi^0_{\text{cell}}$ is the relative ϕ position of a hit to its assigned cell centre. This distribution of correct cell assignment efficiency now shows the ϕ position within a cell where FastCaloSim hits are more likely, and where they are less likely to have been assigned to that same cell if they had been simulated using Geant4. Figure 5.4 shows an example distribution of the efficiency of correct cell assignment as a function of relative ϕ positions using hits from 10 000 65 GeV photons. This example is for cells in the EMB2 layer of the calorimeter with the pseudorapidity range $0.20 < |\eta| < 0.25$.

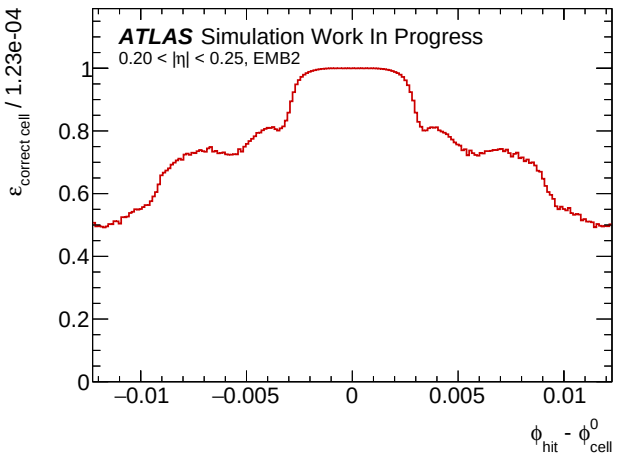

Figure 5.4 *The efficiency of correct cell assignment for the hits of* 10 000 65 GeV *photons in the Electromagnetic Barrel 2 layer in the pseudorapidity range 0.20 < |η| < 0.25.*

Figure 5.5 demonstrates the effect of normalising the integral of the efficiency of correct cell assignment distribution from Figure 5.4 to 1, and using it as a PDF for assigning $\delta\phi$ displacements to 1 million toy hits. The toy hits were produced with an even distribution in ϕ before the randomly sampled displacements were applied. The $\varepsilon_{\text{correct cell}}(\Delta\phi_{\text{rel}})$ is calculated for the displaced toy hits and compared to the distribution from Geant4 hits. This $\varepsilon_{\text{correct cell}}(\Delta\phi_{\text{rel}})$ of the adjusted toy hits shows the distribution of hits that were moved to neighbouring

cells when the $\delta\phi$ displacement was applied.

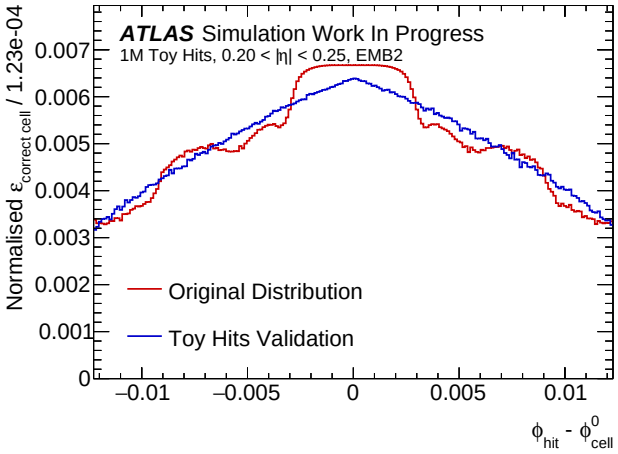

Figure 5.5 *Efficiency of correct cell assignment for 1 million toy hits displaced in ϕ using Figure 5.4 as a PDF to assign the $\delta\phi$ displacements (blue), compared to $\varepsilon_{correct\ cell}(\Delta\phi_{rel})$ for Geant4 hits (red). The integral of both distributions are normalised to 1.*

It is evident that the displacements have not replicated the original distribution that hits in these cells were determined to have using Geant4, and so a more appropriate PDF for applying $\delta\phi$ displacements must be derived.

5.2.2 Probability Density Function Derivation

For the distribution of $\varepsilon_{correct\ cell}(\Delta\phi_{rel})$ in Figure 5.4, values of 1 at the cell centre signify that 100 % of hits that are placed there are assigned the correct cell by FastCaloSim. No $\delta\phi$ displacements are required to move any to neighbouring cells. As $\varepsilon_{\text{correct cell}}(\Delta\phi_{\text{rel}})$ is less than 1 when away from the centre, this indicates that a fraction of these hits need to be moved. Very centrally placed hits in the wrong cell require a large $\delta\phi$ displacement to move them to adjacent cells. From each edge of a cell to the centre, $\varepsilon_{\text{correct cell}}(\Delta\phi_{\text{rel}})$ is essentially a *cumulative distribution function* (CDF) from 0.5 to 1 of the probability that a hit is assigned correctly. The CDF from 0 to 0.5 would concern hits assigned to the neighbouring cell that belong to the cell under consideration. Figure 5.6 shows the form of this CDF. The distribution is normalised to the width of one cell, $\Delta\phi_{\text{cell}}$, in the EMB2 layer, and the frame of reference is centred on the cell boundary at $x = 0$. The function ranges from the centre of the considered cell at $x = +0.5$ to the centre of the neighbouring cell in the $-\phi$ direction at $x = -0.5$, but is applicable for all cells in the layer at the indicated pseudorapidity range, $0.20 < |\eta| < 0.25$.

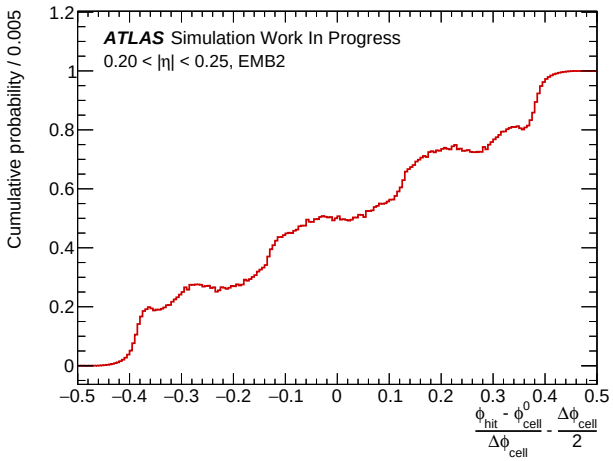

Figure 5.6 *Cumulative distribution of the probability that a hit is assigned to any considered cell as a function of the hit position in ϕ. The frame of reference is centred on a cell boundary and is normalised to the width of one cell in ϕ.*

According to probability theory, a probability density function is determined from the derivative of the associated cumulative distribution function [52]. As the CDF in Figure 5.6 is an empirically binned distribution, the derivative is approximated with the trapezium rule. The value for the i^{th} bin in the PDF is calculated from the difference between the i^{th} and $(i+1)^{\text{th}}$ bin values in the CDF, and the integral is normalised to 1. Figure 5.7 shows the PDF derived from Figure 5.6 for cells in the EMB2 calorimeter layer for the range $0.20 < |\eta| < 0.25$.

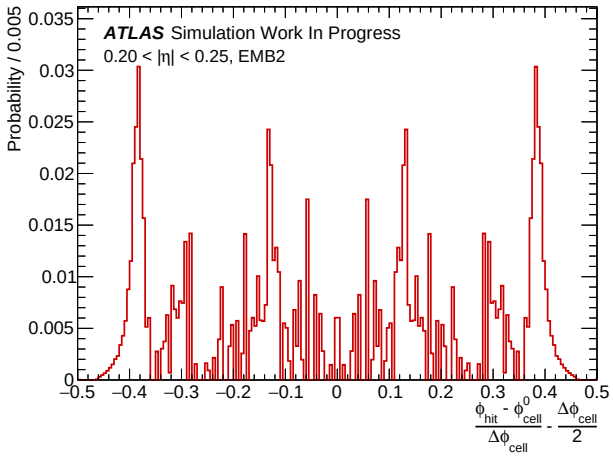

Figure 5.7 *Probability density function that a hit is correctly assigned to the cell as a function of the hit position in ϕ.*

This PDF is validated by using it for assigning $\delta\phi$ displacements to 1 million toy hits, as shown in Figure 5.8. The toy hits were produced with an even distribution in ϕ before the randomly sampled displacements were applied.

The $\varepsilon_{\text{correct cell}}(\Delta\phi_{\text{rel}})$ is calculated for the displaced toy hits and compared to the distribution from Geant4 hits. It is evident that this method shifts the distribution of hits correctly to neighbouring cells, achieving great agreement with the cell assignment efficiency of Geant4 hits.

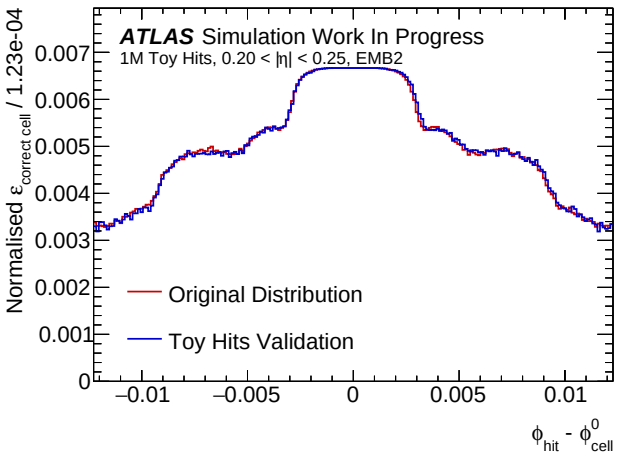

Figure 5.8 *Efficiency of correct cell assignment for 1 million toy hits displaced in ϕ using Figure 5.7 as a PDF to assign the $\delta\phi$ displacements (blue), compared to $\varepsilon_{correct\ cell}(\Delta\phi_{rel})$ for Geant4 hits (red). The integral of both distributions are normalised to 1.*

5.2.3 Probability Density Function Production

The method described in Section 5.2.2 was used to create PDFs for each layer in the LAr calorimeter: PreSamplerB, EMB1, EMB2, EMB3, PreSamplerE, EME1, EME2, and EME3. The LAr accordion structure does not alter particle shower shapes differently for different particle types, so the PDFs were made only from photons. Each was constructed from 10 000 65 GeV Geant4 generated particles.

The PDFs were validated using a set of 1 million toy hits that were produced with an even distribution in ϕ and were found to sufficiently reproduce the desired Geant4 $\varepsilon_{\text{correct cell}}(\Delta\phi_{\text{rel}})$ distributions when the $\delta\phi$ displacements were applied. When integrated with FastCaloSim V2 simulation, the technique greatly reduces the energy deposition bias that is present when the accordion electrodes are not addressed (see Figure 5.3). The validation results for EMB layers in the $0.20 < |\eta| < 0.25$ pseudorapidity range and EME layers in $2.00 < |\eta| < 2.05$ are shown in Figure 5.9 to demonstrate a range of cell structures the $\delta\phi$ displacement method can emulate. The ratio plots show the closure of the displaced toy hits with the original Geant4 distribution.

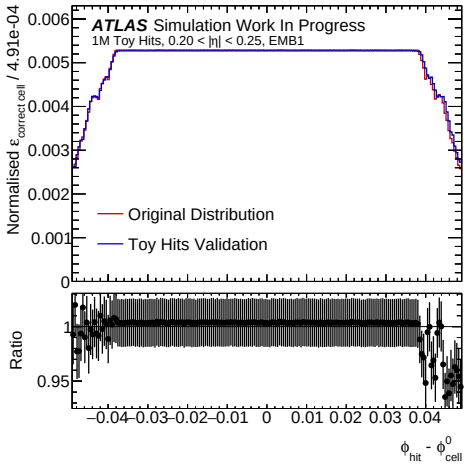

(a) *EMB1, $0.20 < |\eta| < 0.25$*

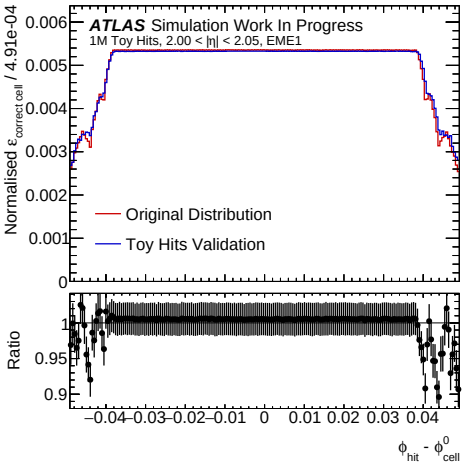

(b) *EME1, $2.00 < |\eta| < 2.05$*

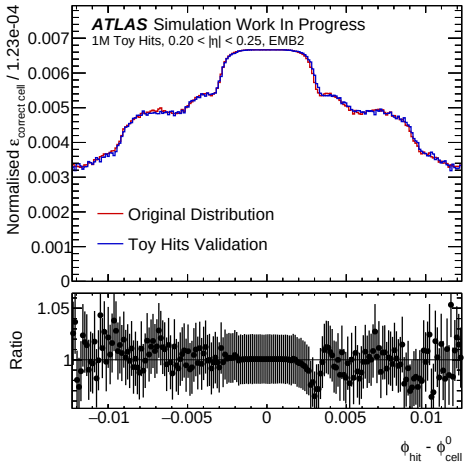

(c) *EMB2, $0.20 < |\eta| < 0.25$*

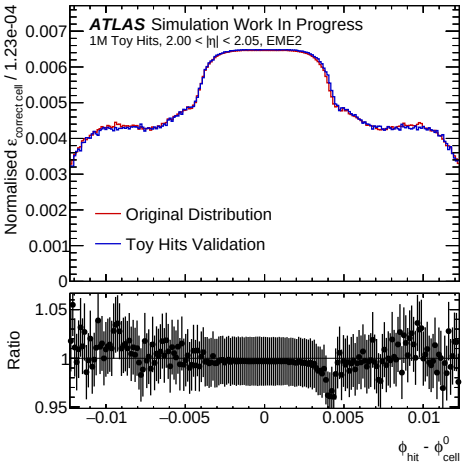

(d) *EME2, $2.00 < |\eta| < 2.05$*

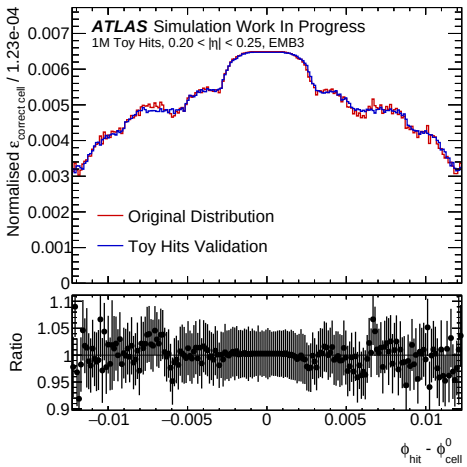

(e) *EMB3, $0.20 < |\eta| < 0.25$*

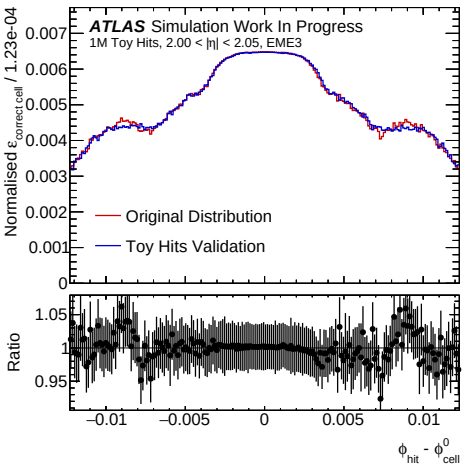

(f) *EME3, $2.00 < |\eta| < 2.05$*

Figure 5.9 *Efficiency of correct cell assignment for 1 million toy hits displaced in ϕ using derived PDFs to assign $\delta\phi$ displacements (blue). They are compared to the original Geant4 distributions (red) in the EMB layers for $0.20 < |\eta| < 0.25$ and the EME layers for $2.00 < |\eta| < 2.05$.*

One final consideration is that for different pseudorapidities, particles originating from the interaction point are incident to the LAr accordion geometry at different angles. In addition, as shown in Table 3.2, the ϕ-granularity of cells changes for particular η ranges. As a result, PDFs were generated for each layer over the pseudorapidity range of $0.00 < |\eta| < 3.20$ in steps of $\delta\eta = 0.05$ to account for these differences. Figure 5.10 shows the validation of the PDFs used for the EME2 layer at two different pseudorapidity slices to illustrate the dissimilarities in the distributions.

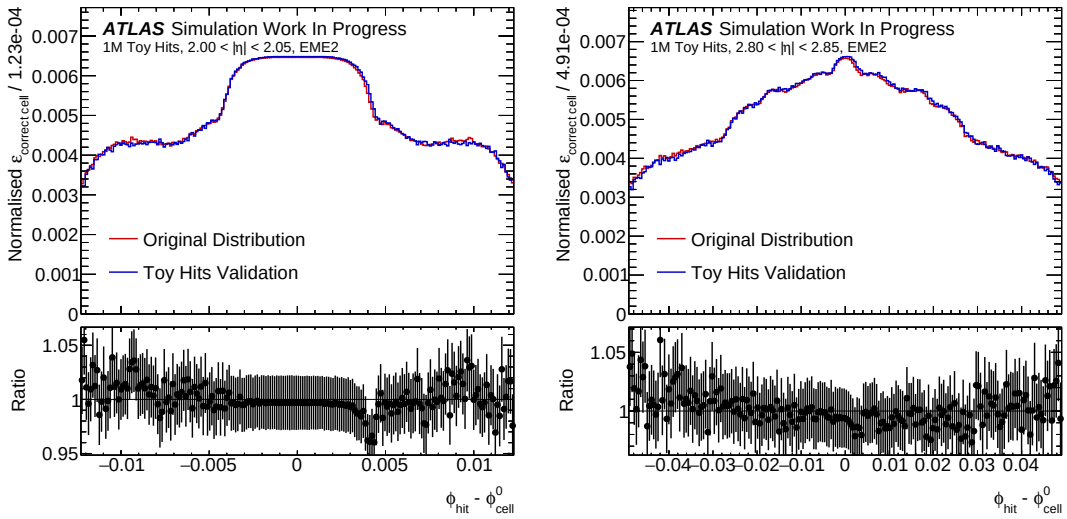

(a) *EME2, $2.00 < |\eta| < 2.05$* **(b)** *EME2, $2.80 < |\eta| < 2.85$*

Figure 5.10 *Comparing the effect of applying $\delta\phi$ displacements to 1 million toy hits to the original distribution of correct cell assignment efficiency for the Electromagnetic End-caps 2 layer of the calorimeter at $2.00 < |\eta| < 2.05$ and at $2.80 < |\eta| < 2.85$.*

This chapter gave a summary of the upgrade for FastCaloSim that retains the simulation speed of the toolkit, but achieves greatly improved agreement with full Geant4 simulation. As part of this upgrade, a method for emulating the accordion structure of the liquid argon calorimeters is described. The technique uses derived PDFs for applying corrective $\delta\phi$ displacements to hits assigned to LAr cells, and these PDFs are now integrated with FastCaloSim V2. The ensuing chapters will describe measurements and studies of the $H \to \gamma\gamma$ channel using the theory, tools, and techniques outlined in Chapters 2–5.

References

[37] The ATLAS Collaboration. 'The ATLAS Simulation Infrastructure'. In: *European Physics Journal C* 70 (2010), pp. 823–874. arXiv: 1005.4568 [ins-det].

[43] The Geant4 Collaboration. *Geant4: A Simulation Toolkit*. 2020. URL: https://www.geant4.org/geant4/ (visited on 17/04/2020).

[48] The ATLAS Collaboration. *AtlFast3: the next generation of fast simulation in ATLAS*. Tech. rep. CERN-EP-2021-174. Geneva: CERN, Sept. 2021. URL: http://cds.cern.ch/record/2780174.

[49] Ian Jolliffe. 'Principal Component Analysis'. In: *International Encyclopedia of Statistical Science*. Ed. by Miodrag Lovric. Berlin, Heidelberg: Springer Berlin Heidelberg, 2011, pp. 1094–1096. ISBN: 978-3-642-04898-2. DOI: 10.1007/978-3-642-04898-2_455.

[50] Flavia Dias. *The new ATLAS Fast Calorimeter Simulation*. Tech. rep. ATL-SOFT-PROC-2016-008. Geneva: CERN, Oct. 2016. URL: https://cds.cern.ch/record/2228659.

[51] The ATLAS Collaboration. *ATLAS calorimeter performance: Technical Design Report*. Technical design report. ATLAS. Geneva: CERN, 1996. URL: https://cds.cern.ch/record/331059.

[52] Douglas C. Montgomery and George C. Runger. *Applied Statistics and Probability for Engineers*. John Wiley and Sons, Inc., 2003, p. 104. ISBN: 978-0-471-20454-1.

Part II

The $H \to \gamma\gamma$ Channel

Chapter 6

Higgs Boson Measurements in the $H \to \gamma\gamma$ Channel

This chapter details the measurement of production cross-sections multiplied by the Higgs boson to diphoton ($H \to \gamma\gamma$) branching ratio using the full Run 2 dataset recorded by ATLAS. The analysis performed the measurement using the *Simplified Template Cross Section* (STXS) framework [6], partitioning the Higgs production phase space in its rapidity range of $|y_H| < 2.5$ by kinematics, event properties, and the production process. A full account of the results of this measurement can be found within this cited publication [53].

6.1 The Run 2 Dataset

The Run 2 dataset is comprised of an integrated luminosity of $(139.0 \pm 2.4)\,\text{fb}^{-1}$ of $\sqrt{s} = 13\,\text{TeV}$ proton-proton collision events, with a mean number of interactions per bunch crossing of $\langle\mu\rangle = 33.7$. Events selected for this analysis were triggered by the presence of two photons exceeding a transverse momentum threshold of 35 GeV and 25 GeV for the respective leading and subleading reconstructed photon objects.

6.2 Monte Carlo Simulation Samples

The event generators, parton distribution function sets, and showering generators used to produce the Monte Carlo signal and background samples used for this measurement are summarised in Table 6.1. The Higgs production cross-sections were calculated for a Standard Model Higgs with a mass of 125.09 GeV at $\sqrt{s} = 13\,\text{TeV}$ to the indicated order of calculation. The cross sections of the background processes were neglected as the normalisation was determined from fits to data.

Table 6.1 *Summary of the event generators and parton distribution function sets used to generate the Monte Carlo samples for signal (upper section) and background (lower section) processes [53].*

Process	Generator	Showering	Parton Distribution Function Set	Cross-Section [pb] at $\sqrt{s} = 13\,\text{TeV}$	Order of Cross-Section Calculation
ggF	NNLOPS	Pythia 8	PDF4LHC15	48.52	N^{3}LO(QCD)+NLO(EW)
VBF	Powheg-Box	Pythia 8	PDF4LHC15	3.78	approx.-NNLO(QCD)+NLO(EW)
WH	Powheg-Box	Pythia 8	PDF4LHC15	1.37	NNLO(QCD)+NLO(EW)
$qq/qg \to ZH$	Powheg-Box	Pythia 8	PDF4LHC15	0.76	NNLO(QCD)+NLO(EW)
$gg \to ZH$	Powheg-Box	Pythia 8	PDF4LHC15	0.12	NLO(QCD)
$t\bar{t}H$	Powheg-Box	Pythia 8	PDF4LHC15	0.51	NNLO(QCD)+NLO(EW)
$b\bar{b}H$	Powheg-Box	Pythia 8	PDF4LHC15	0.49	NNLO(QCD)
$tHqb$	MG5_aMC@NLO	Pythia 8	NNPDF3.0nnlo	0.07	NLO(QCD)
tWH	MG5_aMC@NLO	Pythia 8	NNPDF3.0nnlo	0.02	NLO(QCD)
$\gamma\gamma$	Sherpa	Sherpa	NNPDF3.0nnlo		
$V\gamma\gamma$	Sherpa	Sherpa	NNPDF3.0nnlo		
$t\bar{t}\gamma\gamma$	MG5_aMC@NLO	Pythia 8	NNPDF2.3lo		

To estimate the uncertainty due to the generator modelling of the signal processes, additional samples in which the events are showered using the Herwig 7 generator were also produced.

Pileup from the same and neighbouring bunch crossings was modelled by overlaying inelastic proton-proton simulated events generated using Pythia 8 over the original hard-scattering event.

6.3 Event Selection

Events were selected using the following procedure:

1. Reconstructed photons must satisfy a set of *preselection*-level criteria.
2. The two preselected photons with the highest transverse momenta define the diphoton system and an algorithm selects the primary vertex.

3. This *diphoton primary vertex* is used to define properties of objects in the event, such as: photons, electrons, muons, jets, and missing transverse energy.

4. The photons are then required to meet isolation and additional identification selection criteria.

Electrons, muons, jets, b-tagged jets, and missing transverse energy were all used in the analysis to categorise the diphoton events and measure properties of the Higgs boson.

6.3.1 Photon Identification

Reconstructed photons must have been determined to be contained within the Electromagnetic Calorimeter by having $|\eta| < 2.37$, and avoiding the transition region between the end-caps and the barrels by being exclusive of $1.37 < |\eta| < 1.52$. The candidates were differentiated from jet processes using identification criteria constructed from shower shape variables. This used a *loose* working point for the preselection phase, and then a *tight* working point for final selection. The efficiency of this tight identification ranges from 84–94 % (85–98 %) for unconverted (converted) photons with a transverse momentum above 25 GeV.

The final selection was based on isolation criteria in both the calorimeter and tracking sub-detectors to further reduce misidentification of jets. Calorimeter isolation concerns energy in the Electromagnetic Calorimeter in a radius of $\Delta R = 0.2$ about the photon candidate shower. To have passed, this energy must be less than 6.5 % of the photon transverse momentum. For tracking isolation, the scalar sum of the transverse momenta of tracks with $p_T > 1$ GeV and within a radius of $\Delta R = 0.2$ of the photon candidate must be less than 5 % of the photon transverse momentum.

6.3.2 Selection of Events

The selection of an event initially required identifying two photons passing the preselection loose identification criteria. All photons but the two with the highest transverse momentum were then discarded from consideration. The reconstructed vertex information of the event, in addition to the measured trajectory of the

selected two photons, were used as inputs to a neural network trained on simulated events to identify the diphoton primary vertex. The two photon candidates then must have passed the tight and isolated selection criteria, before being required to pass a final threshold of $p_T/m_{\gamma\gamma} > 0.35$ (0.25) for the leading (subleading) photon. Events failing the tight or isolated selection criteria were used for background estimation and modelling.

Events passing the selection were used in the measurement of the Higgs boson properties. This resulted in around 1.2 million events that exhibit a diphoton invariant mass of $105 < m_{\gamma\gamma} < 160\,\text{GeV}$. Background processes for this selected sample are comprised primarily of continuum $\gamma\gamma$, γj, and jj production where the indicated jets were misidentified as photons during the selection.

6.3.3 Selection of Further Reconstructed Objects

Jets were required to have $p_T > 25\,\text{GeV}$ and $|y| < 4.4$, while the multivariate discriminant of a *jet-vertex-tagger* (JVT) was applied to jets with $p_T < 60\,\text{GeV}$ and $|\eta| < 4.4$ to reduce included jets from pileup. A b-tagging algorithm with 60, 70, 77, and 85 % working points was combined to give a pseudo-continuous b-tagging score to identify jets containing b-hadrons within $|\eta| < 2.5$.

Electrons were selected such that they have $p_T < 10\,\text{GeV}$, $|\eta| < 2.47$, and satisfy isolation criteria. The track of an electron candidate must have been consistent with the primary diphoton vertex by requiring its longitudinal impact parameter in respect to the vertex to satisfy $|z_0 \sin\theta| < 0.5\,\text{mm}$. Also its transverse impact parameter with respect to the beam axis divided by its uncertainty must have satisfied $|d_0|/\sigma_{d_0} < 5$.

Muons must have been determined to have $p_T < 10\,\text{GeV}$, $|\eta| < 2.7$, and satisfy isolation criteria. In addition their tracks must have $|z_0 \sin\theta| < 0.5\,\text{mm}$ and $|d_0|/\sigma_{d_0} < 3$.

To eschew the possibility of double-counting a reconstructed object, electrons overlapping with the two photons within $\Delta R < 0.4$, then jets overlapping with the photons within $\Delta R = 0.4$ and electrons within $\Delta R = 0.2$, followed by electrons overlapping with remaining jets within $\Delta R = 0.4$, and finally muons overlapping with either photons or jets within $\Delta R = 0.4$ were removed in the indicated order.

Finally, missing transverse energy for an event was defined to be the negative

vector sum of the transverse momenta of the selected photons, electrons, muons and jets, in addition to those of the remaining low-p_T tracks originating from the primary vertex.

6.4 Measurement Design

The analysis was constructed to measure the Higgs boson production cross-section in each of the STXS fiducial regions. These regions were defined separately for Higgs bosons with rapidity $|y_H| < 2.5$ based on the Higgs boson production processes:

- The $gg \to H$ process, incorporating the ggF and $gg \to ZH$ production processes, where the Z boson decays hadronically for the latter case.
- The $qq' \to Hqq'$ process, including VBF and $q\bar{q}' \to VH$ processes, where the vector boson decays hadronically in the latter case.
- The VH process, namely $pp \to VH$ production where the vector boson decays leptonically (both to charged leptons and to neutrinos for the ZH instance).
- The associated production with top quarks processes, $t\bar{t}H$ and tH.

For the definition of these regions, the kinematics of the Higgs and associated leptons, jets, top quarks, and jet and lepton multiplicity were used, while the Higgs boson decay properties were not. The specific definitions of these STXS regions are depicted in Figure 6.1, of which there are 44.

In each of these regions a measurement of the product of $\sigma_i \times B_{\gamma\gamma}$ was taken, where σ_i is the production cross-section for an STXS region, i, and $B_{\gamma\gamma}$ is the branching ratio of the Higgs diphoton decay.

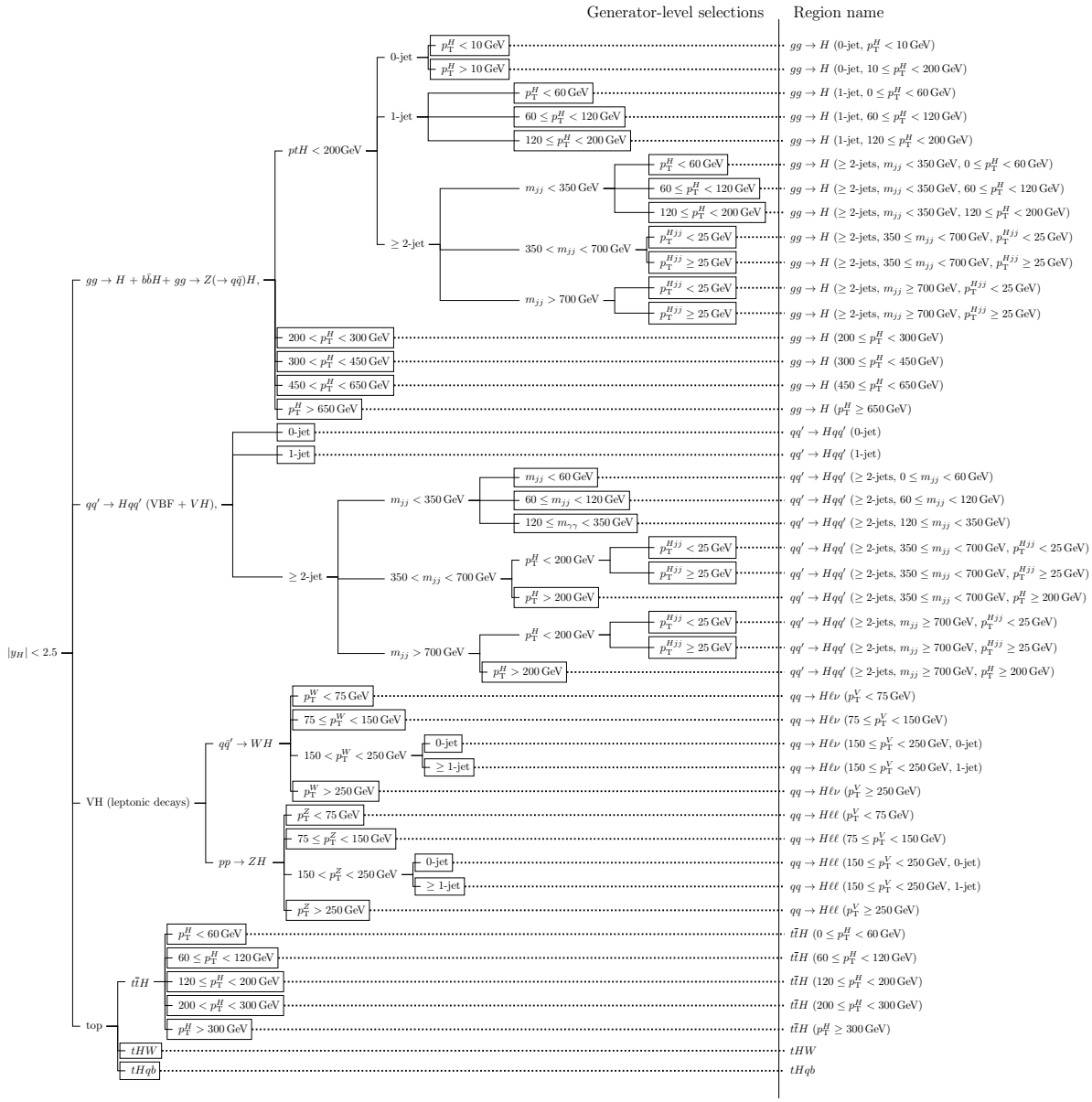

Figure 6.1 *Definitions of the 44 fiducial STXS measurement regions considered in the $H \to \gamma\gamma$ analysis. The names of the regions are listed on the right, while the left depicts the sequentially applied selections that determine events in that region [53].*

6.4.1 Event Categorisation

The selected events were sorted into mutually exclusive *categories*, each designed for measuring one of the particular STXS regions. The assignation of events to a category involved a unified technique that covered all the considered processes simultaneously, designed to maximise the global sensitivity of the categorised events to the STXS parameters. The categorisation occured as follows:

1. A multiclass *boosted decision tree* (BDT), trained on simulation samples to separate signal from the different STXS regions, assigned one discriminant value for each STXS region to each selected event.
2. These discriminant values were used to sort the events into detector level *classes* designed to group events by STXS region at the particle level.
3. Events were assigned categories dependent on the discriminant of a binary BDT classifier trained to separate signal from background in each class.

The initial multiclass BDT permited events to be sorted into classes that would be prohibited due to failures in passing criteria concerning detector level properties using other methods. For instance, events targeted by the $gg \to H$ (1-jet, $p_T^H < 60\,\text{GeV}$) STXS region that failed to reconstruct an associated jet could still have been selected by the multiclass discriminant if it was determined to be the best class match, allowing for measurements with smaller uncertainties and lower correlations.

The binary BDT classifiers trained to split the classes into categories allowed for an increase in the overall measurement sensitivity. For each class, the selected events were sorted into categories dependent on ranges of the resultant binary BDT score, defining a maximum of three categories per STXS region that vary by projected signal purity. The threshold BDT scores that define the number of categories per class were determined by considering all possible values and choosing the definitions that maximise the quadratic sum of the expected significances for all categories. The expected significance, Z, is defined as,

$$Z = \sqrt{2((S+B)\ln(1+S/B) - S)}, \tag{6.1}$$

where S and B were the expected signal and background yields. A total of 88 categories were used, shown in Table 6.2.

The expected SM yields for the measurement were obtained by normalising the simulated samples with the production cross-sections in Table 6.1 multiplied by the $H \to \gamma\gamma$ branching ratio, $B_{\gamma\gamma} = 0.227\,\%$ [6].

Table 6.2 *The expected signal (S) and background (B) event yields contained within the smallest possible mass window that contains 90 % of signal events for each of the 88 $H \to \gamma\gamma$ analysis categories. Also listed are estimates of the signal purities, $f = S/(S+B)$, and the expected significances, Z, as calculated using Equation 6.1. Categories labelled as 'Other' contain groups of events with only minimal contribution to the analysis sensitivity [53].*

Category	S	B	f	Z
$gg \to H$				
0-jets, $p_T^H < 10\,\text{GeV}$	730	24000	0.03	4.6
0-jets, $10 \leq p_T^H < 200\,\text{GeV}$	2200	66000	0.03	8.4
1-jets, $p_T^H < 60\,\text{GeV}$	550	16000	0.03	4.4
1-jets, $60 \leq p_T^H < 120\,\text{GeV}$	470	10000	0.04	4.7
1-jets, $120 \leq p_T^H < 200\,\text{GeV}$, High-purity	37	250	0.13	2.3
1-jets, $120 \leq p_T^H < 200\,\text{GeV}$, Med-purity	50	620	0.07	2.0
$\geq$ 2-jets, $m_{jj} < 350\,\text{GeV}$, $p_T^H < 60\,\text{GeV}$, High-purity	39	1200	0.03	1.1
$\geq$ 2-jets, $m_{jj} < 350\,\text{GeV}$, $p_T^H < 60\,\text{GeV}$, Med-purity	120	5300	0.02	1.6
$\geq$ 2-jets, $m_{jj} < 350\,\text{GeV}$, $p_T^H < 60\,\text{GeV}$, Low-purity	490	19000	0.03	3.6
$\geq$ 2-jets, $m_{jj} < 350\,\text{GeV}$, $60 \leq p_T^H < 120\,\text{GeV}$, High-purity	36	370	0.09	1.8
$\geq$ 2-jets, $m_{jj} < 350\,\text{GeV}$, $60 \leq p_T^H < 120\,\text{GeV}$, Med-purity	110	2300	0.05	2.2
$\geq$ 2-jets, $m_{jj} < 350\,\text{GeV}$, $60 \leq p_T^H < 120\,\text{GeV}$, Low-purity	230	7000	0.03	2.4
$\geq$ 2-jets, $m_{jj} < 350\,\text{GeV}$, $120 \leq p_T^H < 200\,\text{GeV}$, High-purity	44	220	0.17	2.9
$\geq$ 2-jets, $m_{jj} < 350\,\text{GeV}$, $120 \leq p_T^H < 200\,\text{GeV}$, Med-purity	70	830	0.08	2.4
$\geq$ 2-jets, $350 \leq m_{jj} < 700\,\text{GeV}$, $p_T^H < 25\,\text{GeV}$, High-purity	4.1	17	0.19	0.9
$\geq$ 2-jets, $350 \leq m_{jj} < 700\,\text{GeV}$, $p_T^H < 25\,\text{GeV}$, Med-purity	15	110	0.12	1.4
$\geq$ 2-jets, $350 \leq m_{jj} < 700\,\text{GeV}$, $p_T^H < 25\,\text{GeV}$, Low-purity	16	380	0.04	0.8
$\geq$ 2-jets, $350 \leq m_{jj} < 700\,\text{GeV}$, $p_T^H \geq 25\,\text{GeV}$, High-purity	5.7	40	0.12	0.9
$\geq$ 2-jets, $350 \leq m_{jj} < 700\,\text{GeV}$, $p_T^H \geq 25\,\text{GeV}$, Med-purity	20	270	0.07	1.2
$\geq$ 2-jets, $350 \leq m_{jj} < 700\,\text{GeV}$, $p_T^H \geq 25\,\text{GeV}$, Low-purity	22	930	0.02	0.7
$\geq$ 2-jets, $m_{jj} \geq 700\,\text{GeV}$, $p_T^H < 25\,\text{GeV}$, High-purity	4.4	9.0	0.33	1.4
$\geq$ 2-jets, $m_{jj} \geq 700\,\text{GeV}$, $p_T^H < 25\,\text{GeV}$, Med-purity	14	40	0.26	2.1
$\geq$ 2-jets, $m_{jj} \geq 700\,\text{GeV}$, $p_T^H < 25\,\text{GeV}$, Low-purity	16	150	0.10	1.3
$\geq$ 2-jets, $m_{jj} \geq 700\,\text{GeV}$, $p_T^H \geq 25\,\text{GeV}$, High-purity	5.1	33	0.14	0.9
$\geq$ 2-jets, $m_{jj} \geq 700\,\text{GeV}$, $p_T^H \geq 25\,\text{GeV}$, Med-purity	14	150	0.09	1.1
$\geq$ 2-jets, $m_{jj} \geq 700\,\text{GeV}$, $p_T^H \geq 25\,\text{GeV}$, Low-purity	16	380	0.04	0.8
$200 \leq p_T^H < 300\,\text{GeV}$, High-purity	7.2	11	0.40	2.0
$200 \leq p_T^H < 300\,\text{GeV}$, Med-purity	28	84	0.25	2.9
$200 \leq p_T^H < 300\,\text{GeV}$, Low-purity	28	210	0.12	1.9
$300 \leq p_T^H < 450\,\text{GeV}$, High-purity	1.7	1.8	0.49	1.1
$300 \leq p_T^H < 450\,\text{GeV}$, Med-purity	7.1	10	0.41	2.0
$300 \leq p_T^H < 450\,\text{GeV}$, Low-purity	17	63	0.21	2.1
$450 \leq p_T^H < 650\,\text{GeV}$, High-purity	1.9	1.4	0.58	1.4
$450 \leq p_T^H < 650\,\text{GeV}$, Med-purity	2.1	7.5	0.22	0.7
$p_T^H \geq 650\,\text{GeV}$, High-purity	0.72	1.0	0.42	0.7
$p_T^H \geq 650\,\text{GeV}$, Med-purity	0.21	1.1	0.17	0.2
$qq' \to Hqq'$				
0-jet, High-purity	0.32	3.9	0.08	0.2
0-jet, Med-purity	0.60	8.1	0.07	0.2
1-jet, High-purity	1.9	2.3	0.45	1.1
1-jet, Med-purity	2.4	4.8	0.33	1.0
1-jet, Low-purity	4.9	33	0.13	0.8
$\geq$ 2-jets, $m_{jj} < 60\,\text{GeV}$, High-purity	0.61	1.8	0.25	0.4
$\geq$ 2-jets, $m_{jj} < 60\,\text{GeV}$, Med-purity	2.0	8.1	0.20	0.7
$\geq$ 2-jets, $m_{jj} < 60\,\text{GeV}$, Low-purity	5.9	52	0.10	0.8
$\geq$ 2-jets, $60 \leq m_{jj} < 120\,\text{GeV}$, High-purity	5.3	6.1	0.46	1.9
$\geq$ 2-jets, $60 \leq m_{jj} < 120\,\text{GeV}$, Med-purity	6.9	32	0.18	1.2

Category	S	B	f	Z
$qq' \to Hqq'$				
$\geq$ 2-jets, $120 \leq m_{jj} < 350\,\text{GeV}$, High-purity	0.91	3.0	0.23	0.5
$\geq$ 2-jets, $120 \leq m_{jj} < 350\,\text{GeV}$, Med-purity	14	87	0.14	1.4
$\geq$ 2-jets, $120 \leq m_{jj} < 350\,\text{GeV}$, Low-purity	27	380	0.07	1.4
$\geq$ 2-jets, $350 \leq m_{jj} < 700\,\text{GeV}$, $p_T^H < 25\,\text{GeV}$, High-purity	3.1	3.0	0.51	1.6
$\geq$ 2-jets, $350 \leq m_{jj} < 700\,\text{GeV}$, $p_T^H < 25\,\text{GeV}$, Med-purity	12	51	0.19	1.6
$\geq$ 2-jets, $350 \leq m_{jj} < 700\,\text{GeV}$, $p_T^H \geq 25\,\text{GeV}$, High-purity	1.3	1.8	0.42	0.9
$\geq$ 2-jets, $350 \leq m_{jj} < 700\,\text{GeV}$, $p_T^H \geq 25\,\text{GeV}$, Med-purity	0.42	4.7	0.08	0.2
$\geq$ 2-jets, $m_{jj} \geq 700\,\text{GeV}$, $p_T^H < 25\,\text{GeV}$, High-purity	9.0	1.8	0.83	4.5
$\geq$ 2-jets, $m_{jj} \geq 700\,\text{GeV}$, $p_T^H < 25\,\text{GeV}$, Med-purity	18	22	0.45	3.5
$\geq$ 2-jets, $m_{jj} \geq 700\,\text{GeV}$, $p_T^H \geq 25\,\text{GeV}$, High-purity	1.5	1.7	0.47	1.0
$\geq$ 2-jets, $m_{jj} \geq 700\,\text{GeV}$, $p_T^H \geq 25\,\text{GeV}$, Med-purity	2.4	3.4	0.42	1.2
$\geq$ 2-jets, $m_{jj} \geq 700\,\text{GeV}$, $p_T^H \geq 25\,\text{GeV}$, Low-purity	6.5	20	0.24	1.4
$\geq$ 2-jets, $350 \leq m_{jj} < 700\,\text{GeV}$, $p_T^H \geq 200\,\text{GeV}$, High-purity	1.6	1.3	0.55	1.2
$\geq$ 2-jets, $350 \leq m_{jj} < 700\,\text{GeV}$, $p_T^H \geq 200\,\text{GeV}$, Med-purity	0.55	2.0	0.22	0.4
$\geq$ 2-jets, $m_{jj} \geq 700\,\text{GeV}$, $p_T^H \geq 200\,\text{GeV}$, High-purity	8.1	1.6	0.83	4.3
$\geq$ 2-jets, $m_{jj} \geq 700\,\text{GeV}$, $p_T^H \geq 200\,\text{GeV}$, Med-purity	7.6	11	0.42	2.1
$qq \to H\ell\nu$				
Other	7.7	210	0.04	0.5
$0 \leq p_T^V < 75\,\text{GeV}$, High-purity	2.3	3.5	0.40	1.1
$0 \leq p_T^V < 75\,\text{GeV}$, Med-purity	6.3	39	0.14	1.0
$75 \leq p_T^V < 150\,\text{GeV}$, High-purity	3.7	1.8	0.67	2.2
$75 \leq p_T^V < 150\,\text{GeV}$, Med-purity	1.3	4.8	0.21	0.6
$150 \leq p_T^V < 250\,\text{GeV}$, 0-jet	1.8	1.9	0.48	1.1
$150 \leq p_T^V < 250\,\text{GeV}$, 1-jet	2.2	2.3	0.49	1.3
$p_T^V \geq 250\,\text{GeV}$	1.5	1.2	0.56	1.2
$qq \to H\ell\ell$				
Other	11	280	0.04	0.6
$0 \leq p_T^V < 75\,\text{GeV}$	0.9	1.8	0.32	0.6
$75 \leq p_T^V < 150\,\text{GeV}$, High-purity	3.2	3.9	0.45	1.4
$75 \leq p_T^V < 150\,\text{GeV}$, Med-purity	5.6	21	0.21	1.2
$150 \leq p_T^V < 250\,\text{GeV}$, 0-jet	1.6	2.1	0.42	1.0
$150 \leq p_T^V < 250\,\text{GeV}$, 1-jet	1.7	3.2	0.35	0.9
$p_T^V \geq 250\,\text{GeV}$	1.8	2.0	0.47	1.1
$t\bar{t}H$				
Other (including tH)	11	120	0.08	1.0
$p_T^H < 60\,\text{GeV}$, High-purity	3.2	5.0	0.39	1.3
$p_T^H < 60\,\text{GeV}$, Med-purity	3.5	15	0.18	0.8
$60 \leq p_T^H < 120\,\text{GeV}$, High-purity	5.1	4.3	0.54	2.1
$60 \leq p_T^H < 120\,\text{GeV}$, Med-purity	3.7	10	0.26	1.1
$120 \leq p_T^H < 200\,\text{GeV}$, High-purity	6.1	3.8	0.62	2.6
$120 \leq p_T^H < 200\,\text{GeV}$, Med-purity	3.1	8.1	0.28	1.0
$200 \leq p_T^H < 300\,\text{GeV}$	4.6	1.7	0.73	2.7
$p_T^H \geq 300\,\text{GeV}$	3.6	1.0	0.78	2.6
tHW	0.80	2.4	0.25	0.5
$tHqb$	0.88	2.7	0.24	0.5

6.5 Diphoton Invariant Mass Spectrum Modelling

The diphoton invariant mass spectrum for each analysis category is represented by a probability density function that describes the signal and background shapes as analytic functions of $m_{\gamma\gamma}$ defined in the range $105 < m_{\gamma\gamma} < 160\,\text{GeV}$. A simultaneous fit of the diphoton invariant mass spectra to their modelled category

PDFs was performed to obtain the likelihood function for the analysis, incorporating systematic uncertainties as Gaussian or log-normal nuisance parameter PDFs. The Higgs boson cross-sections were represented as parameters of the signal components of the likelihood model, extracted via a maximum likelihood fit over all categories. The normalisation of the signal PDF for each category, i, was defined by

$$N_i = \sum_t (\sigma_t \times B_{\gamma\gamma}) \varepsilon_{it} \mathcal{L} K_i(\theta_{\text{yield}}) + N_i^{\text{spur}} \theta_{\text{spur}}, \tag{6.2}$$

summed over each STXS region, t, where ε_{it} represents the efficiency of events from a region t to be categorised in i, $\mathcal{L}$ is the integrated luminosity of the sample, $K_i(\theta_{\text{yield}})$ denotes multiplicative corrections to the signal yields from systematic uncertainties as a function of θ_{yield} nuisance parameters, and N_i^{spur} is the background modelling uncertainty for i as an additive correction to the signal yield proportional to the θ_{spur} nuisance parameter.

6.5.1 Signal Shape Modelling

The signal shape for each category was modelled as a *double-sided Crystal Ball* (DSCB) function, defined as a Gaussian distribution for the peak region of the shape and flanked by power-law tails continuing from the higher and lower $m_{\gamma\gamma}$ sides of the distribution. The parameters of the DSCB functions for each category were derived from fits to the signal Monte Carlo samples, accounting for the proportion of Standard Model cross-sections of the different production mechanisms that comprised a particular category. Example fits are shown in Figure 6.2.

6.5.2 Background Templates

To model the continuum backgrounds of the analysis categories, a background $m_{\gamma\gamma}$ template was built from an appropriate mixture of data control samples and background Monte Carlo samples. Then a parametric analytic function was assigned to this template from a number of candidate functions, where the best match was determined using the *spurious signal test*. The aim of this test was to assign a function that can flexibly match the diphoton mass distribution from

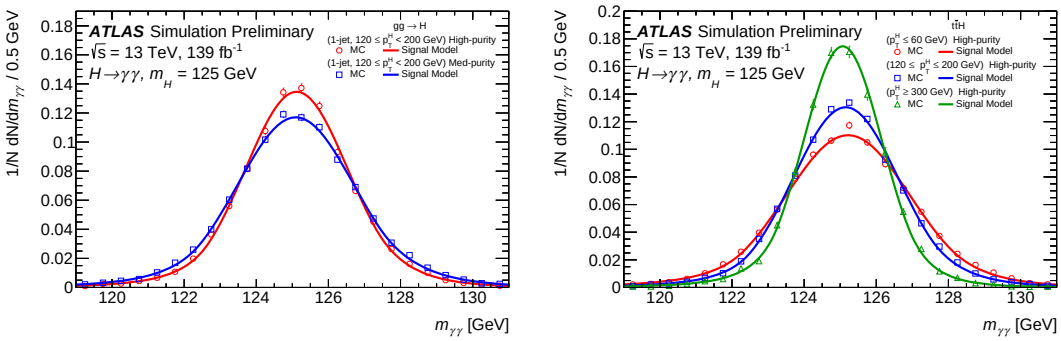

(a) $gg \to H$ *(1-jet,* $120 \leq p_T^H < 200$ *GeV)* **(b)** $t\bar{t}H$

Figure 6.2 *Signal shapes in the diphoton invariant mass spectra for two purity categories for* $gg \to H$ *(1-jet,* $120 \leq p_T^H < 200$ *GeV) and three* $t\bar{t}H$ *analysis categories, fitted as double-sided Crystal Ball functions to signal Monte Carlo samples [53].*

data and that gives very little bias in comparison to the statistical uncertainty.

The continuum background processes were comprised of a combination of $\gamma\gamma$, $j\gamma$, and jj components for the $gg \to H$ and $qq' \to Hqq'$ categories. However the VH, $t\bar{t}H$, and tH background templates were built from only $\gamma\gamma$ processes as the other contributions are negligible. The $\gamma\gamma$ processes for the $gg \to H$ and $qq' \to Hqq'$ categories were modelled using simulation, but $j\gamma$ and jj contribution shapes were obtained from the data sidebands of events that fail to pass the photon identification and isolation selection in the $105 < m_{\gamma\gamma} < 120\,\text{GeV}$ and $130 < m_{\gamma\gamma} < 160\,\text{GeV}$ regions. For the VH categories, background was primarily modelled using $V\gamma\gamma$ simulation samples, while for $t\bar{t}H$ and tH categories the templates were constructed from $t\bar{t}\gamma\gamma$ Monte Carlo. The constructed background templates for two example categories are depicted in Figure 6.3. Data sidebands are represented by the black points and exclude the $120 < m_{\gamma\gamma} < 130$ GeV signal region, while background simulation contributions are shown as coloured histograms.

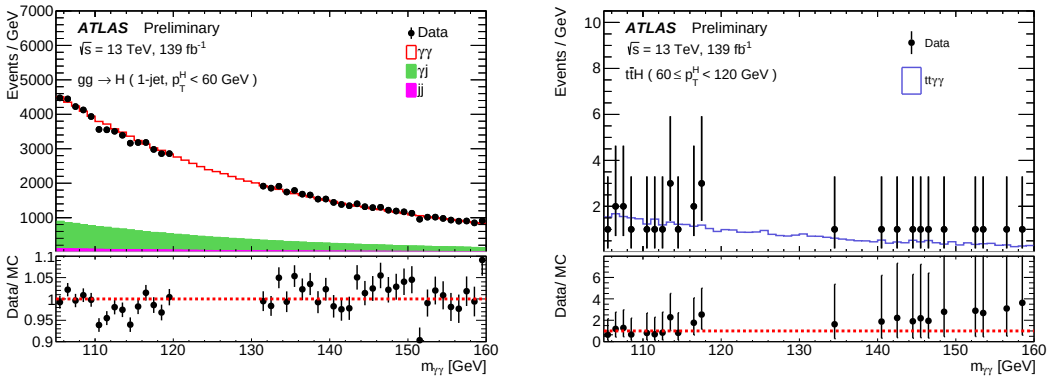

(a) $gg \to H$ *(1-jet,* $p_T^H < 60\,\text{GeV}$*)* **(b)** $t\bar{t}H$ *(*$60 \leq p_T^H < 120\,\text{GeV}$*)*

Figure 6.3 *Constructed background templates in the diphoton invariant mass spectrum for two* $H \to \gamma\gamma$ *analysis categories [53].*

6.5.3 The Spurious Signal Test

The candidate analytic functions tested to model the diphoton invariant mass background continuum for each category are summarised in Table 6.3. All coefficients of these functions were considered as independent across categories and treated as free parameters in fits to the data.

Table 6.3 *The analytic functions used for defining the shape of the continuum* $m_{\gamma\gamma}$ *background and the number of free parameters,* N_{pars}*, used to describe each shape.*

Function Name	Expression	N_{pars}	Acronym
Power Law	$m_{\gamma\gamma}^{a}$	1	`PowerLaw`
Exponential	$\exp(am_{\gamma\gamma})$	1	`Exp`
Exponential of Second-Order Polynomial	$\exp\left(a_1 m_{\gamma\gamma} + a_2 m_{\gamma\gamma}^2\right)$	2	`ExpPoly2`
Exponential of Third-Order Polynomial	$\exp\left(a_1 m_{\gamma\gamma} + a_2 m_{\gamma\gamma}^2 + a_3 m_{\gamma\gamma}^3\right)$	3	`ExpPoly3`
Bernstein Polynomial	$(1-m_{\gamma\gamma})^n + a_1 n m_{\gamma\gamma}(1-m_{\gamma\gamma})^{n-1} + \ldots + a_n m_{\gamma\gamma}^n$	n = 1–5	`Bern1–5`

The selection of the functional form for a category background template was decided by the results of its spurious signal test. For this, the background template was fitted with a model of free parameters to determine both the signal and background event yields. The possible bias that may be incurred by mismodelling the background $m_{\gamma\gamma}$ continuum was then estimated from the resulting fitted signal yield to this purely background template, referred to as the *spurious signal*. The test was performed for possible values of the Higgs mass of $121 < m_H < 129\,\text{GeV}$ in steps of 1 GeV. The potential bias was then considered to be the maximum value of the fitted spurious signal yield, $|S_{\text{spur}}|$, over the range of $121 < m_H < 129\,\text{GeV}$.

Categories containing a minimum of 100 events in their sidebands passed the spurious signal test if it resulted in $|S_{\text{spur}}|$ satisfying either of the following criteria:

- $|S_{\text{spur}}|$ was smaller than 10 % of the expected number of total Higgs boson signal events, S_{exp}.
- $|S_{\text{spur}}|$ was smaller than 20 % of the statistical uncertainty of the fitted signal yield, σ_{exp}.

If more than one analytic function passed the spurious signal test, then the function with the fewest parameters was selected. However, if all functions failed to pass the test then the success criteria were relaxed to require either $\big||S_{\text{spur}}| - 10\,\%S_{\text{exp}}\big| < 2\sigma_{\text{tm}}$ or $\big||S_{\text{spur}}| - 20\,\%\sigma_{\text{exp}}\big| < 2\sigma_{\text{tm}}$, where σ_{tm} is the signal yield uncertainty from the size of the samples comprising the background template. For those categories with fewer than 100 events in the data sidebands, the selection of analytic function was constrained to `Exp`, `ExpPoly2`, and `ExpPoly3` to avoid fitting unphysical shapes caused by large statistical fluctuations.

The fitted spurious signal yield for each category gives an estimate of the possible bias in the fitted true signal yield caused by the intrinsic difference between the background $m_{\gamma\gamma}$ continuum and the selected analytic function. As a result, $|S_{\text{spur}}|$ was used as the systematic uncertainty for modelling the background and its value was substituted for N_i^{spur} for that category, i, in Equation 6.2.

6.6 Systematic Uncertainties

The systematic uncertainties on these measurements arise from uncertainties on the modelling of the diphoton invariant mass spectrum, experimental uncertainties on the expected yields in each category, and theoretical modelling uncertainties. These sources were collected as nuisance parameters into the likelihood model, as explained in Section 6.5. The contributions of groups of systematic uncertainties to the total error on the measured $(\sigma \times B_{\gamma\gamma})$ for the considered Higgs boson production processes are shown in Table 6.4.

Table 6.4 *The percentage contributions of groups of systematic uncertainties to the total error on the observed measurements of cross section multiplied by branching ratio for the indicated production processes.*

Uncertainty Source	$\Delta\sigma$ [%]				
	ggF $+b\bar{b}H$	**VBF**	WH	ZH	$t\bar{t}H + tH$
Underlying Event and Parton Shower (UEPS)	± 2.3	± 10	$< \pm 1$	± 9.6	± 3.5
Modelling of Heavy Flavour Jets in non-$t\bar{t}H$ Processes	$< \pm 1$	$< \pm 1$	$< \pm 1$	$< \pm 1$	± 1.3
Higher Order QCD Terms (QCD)	± 1.6	$< \pm 1$	$< \pm 1$	± 1.9	$< \pm 1$
Parton Distribution Function and α_S Scale (PDF+α_S)	$< \pm 1$	± 1.1	$< \pm 1$	± 1.9	$< \pm 1$
Photon Energy Resolution	± 2.9	± 2.4	± 2.0	± 1.3	± 4.9
Photon Energy Scale (PES)	$< \pm 1$	$< \pm 1$	$< \pm 1$	± 3.4	± 2.2
Jet/E_T^{miss}	± 1.6	± 5.5	± 5.5	± 4.0	± 3.0
Photon Efficiency	± 2.5	± 2.3	± 2.4	± 1.4	± 2.4
Background Modelling ($\lvert S_{\text{spur}}\rvert$)	± 4.1	± 4.7	± 2.8	± 18	± 2.4
Flavour Tagging	$< \pm 1$	$< \pm 1$	$< \pm 1$	$< \pm 1$	$< \pm 1$
Leptons	$< \pm 1$	$< \pm 1$	$< \pm 1$	$< \pm 1$	$< \pm 1$
Pileup	± 1.8	± 2.7	± 2.1	± 3.8	± 1.1
Luminosity and Trigger	± 2.1	± 2.1	± 2.3	± 1.1	± 2.3
Higgs Boson Mass	$< \pm 1$	$< \pm 1$	$< \pm 1$	± 3.7	± 1.9

6.7 Measurement Results

The Higgs boson total production cross-section multiplied by the $H \to \gamma\gamma$ branching ratio was measured to be

$$(\sigma \times B_{\gamma\gamma})_{\text{obs}} = (127 \pm 10)\,\text{fb} = 127 \pm 7\ (\text{stat.}) \pm 7\ (\text{syst.})\ \text{fb}, \tag{6.3}$$

which is considered to be in good agreement with the expected Standard Model value of

$$(\sigma \times B_{\gamma\gamma})_{\text{exp}} = (116 \pm 5)\,\text{fb}. \tag{6.4}$$

The measurements of the STXS region cross-sections are displayed in Figure 6.4 as a ratio to their Standard Model descriptions. To avoid large absolute correlations and uncertainties, some of the 44 regions shown in Figure 6.1 were merged, resulting in a total of 27 measurement bins.

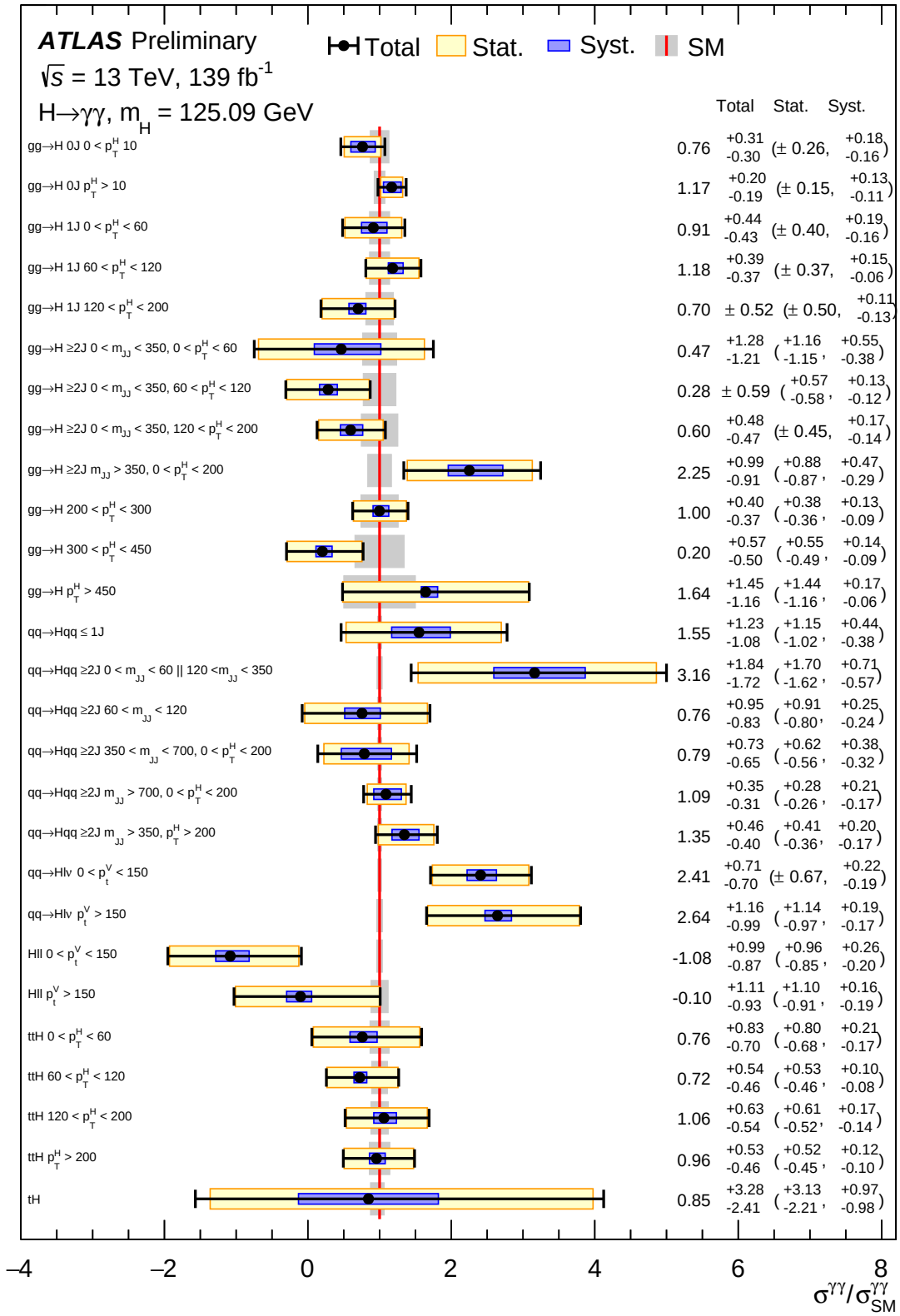

Figure 6.4 *Best-fit values and uncertainties for the cross-sections of the STXS regions considered by the $H \to \gamma\gamma$ as a ratio to their expected Standard Model values. Measurements for the $gg \to H$ process also include the contributions from the $b\bar{b}H$ production mechanism. The grey bands display the theoretical uncertainties on the SM predictions [53].*

This chapter outlined how the Higgs boson production cross-sections multiplied by the diphoton branching ratio were measured. The utilisation of categories based on STXS classes and how they were defined to increase the significances of the measurements were explained. It was described how signal and background shapes in these categories were modelled, and how the contributions of the uncertainties on these models affect the measurement. Chapters 7–10 present studies for improving the understanding of these modelling uncertainties and for reducing their impact on the $H \to \gamma\gamma$ analysis.

References

[6] D. de Florian et al. *Handbook of LHC Higgs Cross Sections: 4. Deciphering the Nature of the Higgs Sector*. CERN Yellow Reports: Monographs CERN-2017-002-M. Oct. 2016. DOI: 10.23731/CYRM-2017-002.

[53] The ATLAS Collaboration. *Measurement of the properties of Higgs boson production at $\sqrt{s}$=13 TeV in the $H \to \gamma\gamma$ channel using 139 fb^{-1} of pp collision data with the ATLAS experiment*. Tech. rep. ATLAS-CONF-2020-026. Geneva: CERN, Aug. 2020. URL: https://cds.cern.ch/record/2725727.

Chapter 7

Estimating Required Sizes of $\gamma\gamma$ Background Samples

As described in Section 6.5.2, modelling the background diphoton invariant mass continuum for $H \to \gamma\gamma$ analysis categories relies on the construction of templates from simulated background Monte Carlo samples. Section 6.5.3 then details how the spurious signal test is used on these constructed templates to model the continuum shape as an analytic functional form, determining the background modelling uncertainty in the process. However, the statistical fluctuations arising from the number of simulated events comprising a background template will cause discrepancies between its fitted functional form and the intrinsically unknown true shape. Consequently, the systematic uncertainty on the background modelling ($|S_{\text{spur}}|$) is dependent on the size of the simulation samples used to construct the background template.

As shown in Table 6.4, the systematic uncertainty on the background modelling in the ggF production category is the largest error contribution for measuring ($\sigma_{gg\to H} \times B_{\gamma\gamma}$). Unless more events are generated, the relative contribution of this uncertainty to the total measurement uncertainty is expected to grow, as the data statistical uncertainty will decrease with future increases in the integrated luminosity. This chapter describes a method used for estimating the number of simulated events required in the background $\gamma\gamma$ Monte Carlo sample to pass the spurious signal test in the $gg \to H$ categories.

7.1 Creating Pseudo-Datasets

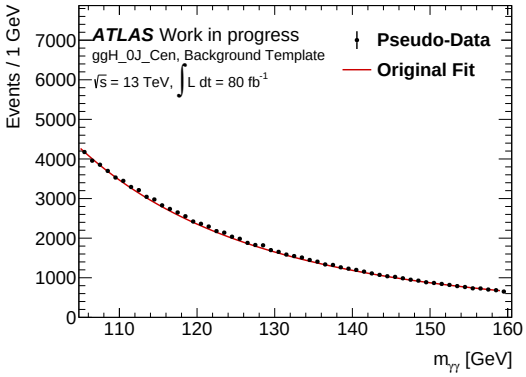

(a) *Nominal background template.*

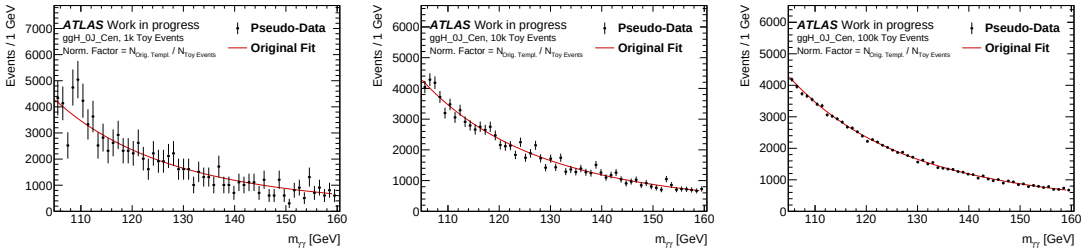

(b) 1 k *toy events.* **(c)** 10 k *toy events.* **(d)** 100 k *toy events.*

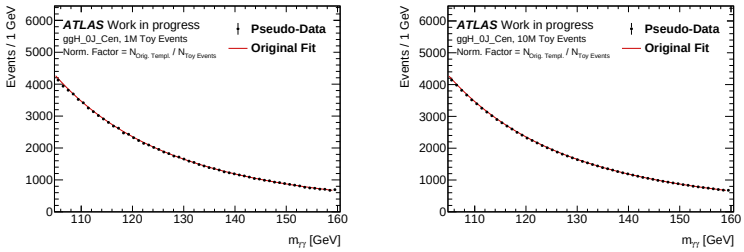

(e) 1 M *toy events.* **(f)** 10 M *toy events.*

Figure 7.1 *The nominal background template for the legacy* `ggH_0J_Cen` *$H \to \gamma\gamma$ analysis category and five generated pseudo-datasets with differing statistics.*

To quantify how the statistics of a Monte Carlo sample affect the resultant spurious signal, a number of different templates were produced, comprised of differing numbers of events. To produce these templates of variable statistics, *pseudo-datasets* were created using the nominal category background templates from the previous pass of measurements in the $H \to \gamma\gamma$ channel [54], referred to as *legacy* categories. By randomly sampling from a PDF in $m_{\gamma\gamma}$, derived from fitting the nominal templates to the functional form assigned to them by the spurious signal test, 500 pseudo-datasets for each $gg \to H$ category were created:

100 occurrences each of 1000, 10 000, 100 000, 1 million, and 10 million toy event samples. Each pseudo-dataset was normalised to the number of events contained in the original category background template. Figure 7.1 displays the nominal fitted background template for the legacy `ggH_0J_Cen` category and an example pseudo-dataset created for each statistical size that was produced.

7.2 Effects of Sample Sizes on Spurious Signal

The spurious signal test was subsequently performed on each of the aforementioned 500 pseudo-datasets in each legacy category, testing the functional forms from Table 6.3. For each spurious signal test result, the quantities of $S_{\text{spur}}/S_{\text{exp}}$, and $S_{\text{spur}}/\sigma_{\text{exp}}$ (as defined in Section 6.5.3) were recorded for the best fitting functional form. These quantities are the scores used by the spurious signal test to determine whether the background template fit to a functional form is valid for the analysis. For a functional form to be accepted, the spurious signal yield must satisfy either,

- $S_{\text{spur}}/S_{\text{exp}} < 10\,\%$,
- or $S_{\text{spur}}/\sigma_{\text{exp}} < 20\,\%$.

By taking the *root mean square* (RMS) value for each of these scores over the results from all pseudo-datasets constructed with the same number of randomly sampled toy events, and then plotting these values as a function of the pseudo-dataset size, the dependence of these quantities on the number of events in a sample can be determined. The number of events in a background template that would be required for each category to be defined to pass the spurious signal test, $N_{\text{MC}}^{\text{req.}}$, can be derived by evaluating these trends for the spurious signal passing criteria stated above. This was compared to the number of $\gamma\gamma$ events in the original sample to determine the scale factor required to increase the sample size.

Figure 7.2 shows the resultant trends for the RMS of the relevant spurious signal test quantities as a function of pseudo-dataset sample size for the legacy `ggH_0J_Cen` category. The mean of the results over the 100 samples for each number of toy events is shown underneath the spurious signal quantity trends. These should equate as 0 if the toy events distribution is truly random because the spurious signal quantities fitted to the pseudo-data templates should have an

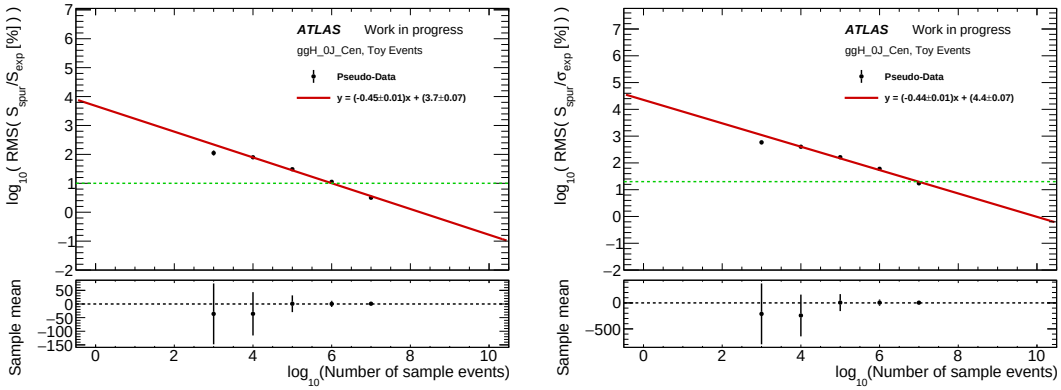

Figure 7.2 *The dependence of spurious signal test quantities on the size of the background template it was performed on for the legacy* `ggH_0J_Cen` *$H \to \gamma\gamma$ analysis category. The green dotted lines represent the spurious signal passing criteria thresholds, valued at 10 % for (a) and 20 % for (b).*

equal chance of being positive or negative when exhibiting fluctuations around the fit in the signal region. The sample mean plots in Figure 7.2 show that although each pseudo-data point is consistent with 0 within one standard deviation, negative fitted spurious signal yields are more common for templates produced from a low number of events.

7.3 Results for the $|S_{\text{spur}}| < 10\%\ S_{\text{exp}}$ Criterion

This section presents the results for estimating the required number of background template events, $N_{\text{MC}}^{\text{req.}}$, for the legacy $gg \to H$ categories. This estimate is compared to the number of events comprising the original template, $N_{\text{MC}}^{\text{orig.}}$, for that category to give a proposed scale factor, $SF = N_{\text{MC}}^{\text{req.}}/N_{\text{MC}}^{\text{orig.}}$, that the original simulated sample would need to be increased by to achieve the indicated requirement. The total number of simulated $\gamma\gamma$ events produced for the original category templates was 500 million events. Table 7.1 displays these results by category.

The selection efficiency of $\gamma\gamma$ simulated events for categorisation is constant on average between samples, and so scaling the nominal sample by the largest specified value of SF is sufficient to increase the sample size for all category background templates. The largest value for SF when considering the $|S_{\text{spur}}| < 10\%\ S_{\text{exp}}$ spurious signal test criterion is the `ggH_2J_BSM` category,

Table 7.1 *The number of background template events required to pass the spurious signal test $|S_{\text{spur}}| < 10\%\ S_{\text{exp}}$ criterion for each legacy $gg \to H$ category and the required scale factors.*

Category	$N_{\text{MC}}^{\text{orig.}}$	$N_{\text{MC}}^{\text{req.}}$	$SF = N_{\text{MC}}^{\text{req.}}/N_{\text{MC}}^{\text{orig.}}$
ggH_0J_Cen	1 655 000	1 021 000	0.62
ggH_1J_LOW	3 072 000	1 986 000	0.65
ggH_1J_MED	1 164 000	846 000	0.73
ggH_1J_HIGH	128 000	188 000	1.47
ggH_1J_BSM	20 000	57 000	2.81
ggH_2J_LOW	1 435 000	4 265 000	2.97
ggH_2J_MED	822 000	1 543 000	1.88
ggH_2J_HIGH	137 000	267 000	1.94
ggH_2J_BSM	12 000	45 000	3.60

requiring a multiplicative increase of **3.60** over the original template size.

7.4 Results for the $|S_{\text{spur}}| < 20\%\ \sigma_{\text{exp}}$ Criterion

Table 7.2 displays the results for passing the $|S_{\text{spur}}| < 20\%\ \sigma_{\text{exp}}$ spurious signal test criterion for legacy $gg \to H$ categories. The largest value of SF is caused by the ggH_0J_Cen category, requiring a multiplicative increase of **5.73** to the original number of template events.

Table 7.2 *The number of background template events required to pass the spurious signal test $|S_{\text{spur}}| < 20\%\ \sigma_{\text{exp}}$ criterion for each legacy $gg \to H$ category and the required scale factors.*

Category	$N_{\text{MC}}^{\text{orig.}}$	$N_{\text{MC}}^{\text{req.}}$	$SF = N_{\text{MC}}^{\text{req.}}/N_{\text{MC}}^{\text{orig.}}$
ggH_0J_Cen	1 655 000	9 485 000	5.73
ggH_1J_LOW	3 072 000	10 979 000	3.57
ggH_1J_MED	1 164 000	3 258 000	2.80
ggH_1J_HIGH	128 000	275 000	2.15
ggH_1J_BSM	20 000	39 000	1.92
ggH_2J_LOW	1 435 000	4 010 000	2.86
ggH_2J_MED	822 000	1 979 000	2.41
ggH_2J_HIGH	137 000	295 000	2.14
ggH_2J_BSM	12 000	32 000	2.59

7.5 Required $\gamma\gamma$ Background Sample Size Estimate

When considering the results from the two different spurious signal test criteria presented in Section 7.3 and Section 7.4, the required scale factors determined to adequately increase the background simulation samples were $\boldsymbol{SF = 3.60}$ and $\boldsymbol{SF = 5.73}$. However, since both the $|S_{\text{spur}}| < 10\%\ S_{\text{exp}}$ and the $|S_{\text{spur}}| < 20\%\ \sigma_{\text{exp}}$ criteria hold equal weight in passing the test, the smaller factor of $SF = 3.60$ was adequate.

Due to the stochastic nature of the random fluctuations in the modelling shape caused by the background template statistics, this increase of $SF = 3.60$ corresponds to passing the spurious signal test with a confidence level of $\sim 68\,\%$ (1σ of a normal distribution). To achieve an estimate for the increase in generated $\gamma\gamma$ events that produce $gg \to H$ background templates that pass the spurious signal test with a confidence level of $\sim 95\,\%$ (2σ), it was suggested to increase the sample by a $\boldsymbol{SF = 7.2}$. Similar checks were performed in the VBF and VH categories, where it was determined that no increase in template statistics was required.

This estimate on the required number of $\gamma\gamma$ simulated background events was used as strong evidence for the case of increasing the sample sizes. A request for a further 500 million $\gamma\gamma$ events was granted by ATLAS Monte Carlo production, and the sample size was increased for the legacy Run 2 analysis paper.

Other techniques have been developed for the $H \to \gamma\gamma$ analysis to improve the spurious signal yield, and thus the uncertainty on the background modelling. One such technique uses *Gaussian process regression* (GPR) [55, 56] to smooth background templates and reduce statistical fluctuations before applying the spurious signal test. These methods are complementary to increasing the background statistics as they only provide unbiased results in case of large background template statistics, and are thus applicable only to a subset of $H \to \gamma\gamma$ analysis categories. For all others, this sample size estimation method is important for identifying when the background statistics must be increased.

This chapter detailed a method for estimating the number of simulation events required for a background template to pass the spurious signal test. This was used to determine the number of simulated $\gamma\gamma$ background events that would be

required for legacy $gg \to H$ category background templates. It was concluded that the background sample required an increase by a factor of 7.20 to pass the spurious signal test in all categories with a 95 % confidence level. This result led to the production of an additional 500 million events for the $H \to \gamma\gamma$ analysis, substantially reducing the systematic uncertainties for the measurement. Chapter 8 will describe a method using multivariate reweighting to estimate $H \to \gamma\gamma$ uncertainties introduced by the differences between event generator calculations.

References

[54] The ATLAS Collaboration. *Measurements of Higgs boson properties in the diphoton decay channel using 80 fb^{-1} of pp collision data at $\sqrt{s}$ = 13 TeV with the ATLAS detector*. Tech. rep. ATLAS-CONF-2018-028. Geneva: CERN, July 2018. URL: `https://cds.cern.ch/record/2628771`.

[55] The ATLAS Collaboration. *Measurements and interpretations of Higgs-boson fiducial cross sections in the diphoton decay channel using 139 fb^{-1} of pp collision data at $\sqrt{s}$ = 13 TeV with the ATLAS detector*. Tech. rep. ATLAS-CONF-2019-029. Geneva: CERN, July 2019. URL: `https://cds.cern.ch/record/2682800`.

[56] Rachel Jordan Hyneman. 'Measuring Higgs Boson Couplings, including to the Top Quark, in the Diphoton Decay Channel with Run 2 Data Collected by the ATLAS Detector'. Presented 04 Feb 2020. URL: `https://cds.cern.ch/record/2712576`.

Chapter 8

Multivariate Reweighting of Simulation Samples

When using Monte Carlo simulation to create the statistical representations of an underlying physics model, the particular generator used will affect the results. The different generators utilise complementary techniques to evaluate the hard process matrix elements, and to model parton showers and hadronisation, which are difficult to calculate from first principles and must be approximated. Unless the data indicates otherwise, all generators must be assumed to match the real physics model and the differences between them introduce a systematic uncertainty. The traditional method used to evaluate this uncertainty is to produce supplementary simulation samples using variant generator settings and to perform the analysis steps on both the nominal and the supplementary samples to observe how the results change. However, since the size of nominal samples is increasing to match the growing integrated luminosity produced by the LHC, it becomes evermore computationally intensive to provide statistically significant supplementary simulation samples. This chapter introduces a multivariate reweighting method, which may be used to estimate generator modelling uncertainty without the production of supplementary samples.

The proposed technique uses the `carl-torch` toolbox [57]. It is based on `carl` [58], a package developed for likelihood-free inference using PyTorch [59], but built for the purpose of multivariate reweighting in particle physics experiments.

8.1 Multivariate CARL Weights

To illustrate the technique, we will first begin with the case of two samples of events characterised by a single variable, x. Each sample was produced using a different probability density function, $p(x)$, to represent a difference in event generator. To reweight the sample produced using the function $p_0(x)$ to look like it was produced using the other, $p_1(x)$, we would apply a weight defined by the ratio,

$$r(x) = p_1(x)/p_0(x). \tag{8.1}$$

This would result in a perfect reweighting by definition, but particle physics events are characterised by many variables and the underlying probability densities of their distributions are not explicitly known.

To expand this concept to encompass the full phase space, multivariate reweighting is defined using samples of events characterised by n considered variables represented by an n-dimensional vector, $\mathbf{x}$. A neural network is used to train a binary classifier to differentiate the sample generated using $p_0(\mathbf{x})$ from that generated using $p_1(\mathbf{x})$. In the perfect case, this classifier would equate to

$$s(\mathbf{x}) = \frac{p_0(\mathbf{x})}{p_0(\mathbf{x}) + p_1(\mathbf{x})}, \tag{8.2}$$

resulting in an output of either 0 or 1. However, as the network is trained on finite samples from each generator, the classifier will instead be an approximation, $\hat{s}(\mathbf{x})$, which is shown to be sufficient to produce accurate results [60]. By using Equation 8.1, the classifier can be written as

$$\hat{s}(\mathbf{x}) = \frac{1}{1 + \hat{r}(\mathbf{x})}, \tag{8.3}$$

where $\hat{r}(\mathbf{x})$ are the derived CARL weights that are used to reweight the initial sample to the desired one, and are extracted from the neural network using

$$\hat{r}(\mathbf{x}) \approx \frac{1 - \hat{s}(\mathbf{x})}{\hat{s}(\mathbf{x})}. \tag{8.4}$$

8.2 Deriving CARL Weights with Neural Networks

The neural networks constructed in this thesis were executed on two samples of Monte Carlo events that were each produced with a defined generator variation. The events in the samples were processed by the network as feature vectors of a set of input variables. The chosen input variables are critical in the ability of the neural network to accurately estimate the binary classifier, $\hat{s}(\mathbf{x})$. Thus, the input variables are selected based on their propensity to allow the network to distinguish events as belonging to one generator setting or the other, and for their importance in the $H \to \gamma\gamma$ analysis categorisation.

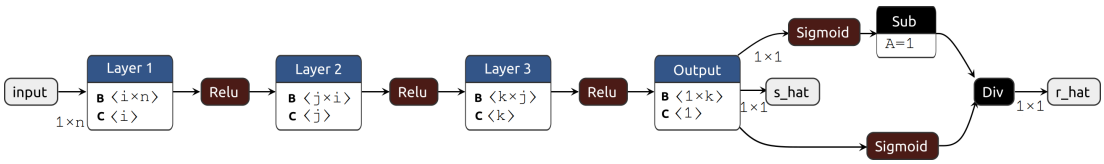

Figure 8.1 *The neural network model used for deriving CARL weights, as visualised using Netron [61].*

The composition of the network for each study is defined as an input layer of n nodes that feed three fully connected successive hidden layers comprised of i, j, and k nodes. The template structure of the neural network is shown in Figure 8.1. Each node in a layer is connected to every node in the next layer. For every input event processed by the network, the value of each input node is set as the corresponding input variable. The value of each node in the first hidden layer is then given by the output of the *Rectified Linear Unit* (ReLU) activation function [62] for the sum of values of all the nodes connected to it. This process is repeated through each of the hidden layers before defining one output classifier value in the output layer. This value is then transformed into the ratio estimate as in Equation 8.4, by estimating $1 - \hat{s}(\mathbf{x})$, then dividing this by the determined classifier value using the *Sigmoid* activation function [63]. Each connection in the network is characterised by a weight, and the activation of each node is defined by a bias. In Figure 8.1, the number of values for the weights and biases in each layer are given by **B** and **C** respectively. For example, if each input value is defined by x_1 to x_n, each connection to the first node of the first hidden layer has a weight labelled w_{11} to w_{n1}, and the activation bias of that node is b_1, then the result of the activation of that node, A_1, is given by

$$A_1 = \text{ReLU}(x_1 w_{11} + x_2 w_{21} + ... + x_n w_{n1} + b_1). \tag{8.5}$$

The training of each network is the process by which the weights for each connection and the biases for each node are tuned using a training sample, $\mathbf{x}$. The *binary cross-entropy* function [64] is used during training as the *loss function* to evaluate how well the network identified an input training event as belonging to the correct Monte Carlo sample. A lower loss indicates a more accurate classification. The network is trained by backpropagating through the network result and altering the weights and biases to minimise the net value of this loss function for the entire training sample in a process called *gradient descent*, which was optimised using the AMSGrad algorithm [65]. Gradient descent is controlled by a number of factors:

- the *batch size* is the number of events that the network processes before updating the model weights and biases,
- the *training rate* is the value by which the net value of the loss function is reduced at every update of the network,
- and the total number of *epochs* is the total number of full passes made over the entire training sample and defines the total length of the training.

The structure of the neural network and the settings used when training are termed as *hyperparameters* and are important factors in the performance of deriving CARL weights. The networks used in this thesis optimise the number of nodes in each hidden layer, as well as the training batch size, and learning rate. For all cases it was found that 200 epochs resulted in a well trained network.

8.2.1 Optimising Hyperparameters

The process for optimising the CARL derivation neural network for each study tested a number of different hidden layer node architectures. Each architecture was assessed by training that network model on the training sample over the 200 epochs using batch sizes of 1024, 2048, and 4096 events; and initial learning rates of 0.05, 0.01, and 0.001, decaying by a factor of 10 over the full course of training until reaching 0.005, 0.001, and 0.0001. The trained network is then used to apply the CARL weights it determines to a validation sample that is comprised of the remaining events from the two original Monte Carlo samples that were excluded from training.

To assess the performance of a particular network architecture, an ensemble of unbinned two-sample *Kolmogorov-Smirnov* (KS) tests [66] were evaluated for the variable distributions of the validation sample. The KS test determines the compatibility of two distributions with each other, giving a lower *KS score* the better they match. This is used to test the compatibility of the variable distributions of the two differently generated Monte Carlo samples before and after CARL reweighting of one sample to the other, with the hope that the CARL weighted sample results in a lower KS score. For each considered variable, the improvement in the KS score, KS_{Impr}, was calculated as a function of the CARL weighted (KS_{CARL}) and unweighted ($KS_{\text{no weights}}$) KS score as,

$$KS_{\text{Impr}} = \frac{KS_{\text{no weights}} - KS_{\text{CARL}}}{KS_{\text{no weights}} + KS_{\text{CARL}}}. \tag{8.6}$$

The optimal hyperparameter configuration was then chosen as that which produces the highest average KS_{Impr} over all considered variable distributions.

8.3 Evaluating CARL Reweighting Performance

An assessment of the CARL reweighting in each study was made initially by evaluating how well the neural network training performed, and subsequently by how well the reweighting emulates the generator variation being studied.

8.3.1 Neural Network Performance

The training of the neural network can be assessed by plotting the value of the loss function for each training epoch. The desire is that the loss function value plateaus towards the end of the training, as this indicates that the network has been trained optimally. Additionally, if a second training is performed using the validation sample, then the loss value per epoch can be compared to assess *overtraining*. The network would be said to be overtrained if the training and validation loss functions are not in close agreement, indicating that the network was taught to model statistical fluctuations in the training data.

The performance of the network in deriving the CARL weights can be assessed by training a second network to classify whether an event was produced using

one generator variation (G_0) or the other (G_1). By executing this second network on a sample comprised of G_1 and unweighted G_0 events, and then again but CARL weighting the G_0 events, then the number of times the network correctly or incorrectly classifies an event as G_0 or G_1 can be counted. These results can be used to create *receiver operating characteristic* (ROC) curves [67]. If the classifier fails to be able to reliably distinguish events and determines that the classification is completely random, then the *area under the curve* (AUC) of the ROC curve will evaluate as 0.5. Thus, if the CARL derivation network performs as desired, the AUC of the ROC curve produced using the CARL weighted G_0 sample will be as close to 0.5 as possible, and substantially closer than the unweighted G_0 sample.

8.3.2 Reweighting Performance

The performance of the CARL reweighting is assessed by comparing variable distributions of the CARL weighted and unweighted G_0 samples to those from the G_1 sample. For each considered variable, χ^2/NDF is evaluated to gauge the agreement of both of the G_0 distributions to that of the G_1 events. The χ^2/NDF value for comparing two distributions is equal to 0 if they match perfectly. Thus, if the reweighting performs as desired, then the χ^2/NDF value for the agreement of the CARL weighted distribution ($(\chi^2/NDF_{\text{CARL}})$) will be lesser than the value for the unweighted distribution ($(\chi^2/NDF_{\text{no weights}})$).

The difference in the values, $\Delta\chi^2/NDF$, is used as a metric to determine the reweighting performance, and is calculated using,

$$\Delta\chi^2/NDF = (\chi^2/NDF_{\text{no weights}}) - (\chi^2/NDF_{\text{CARL}}). \tag{8.7}$$

The larger this value is, the greater the effect of the CARL reweighting for emulating G_1 in that variable. However, if this value is negative then it demonstrates that the CARL reweighting has worsened agreement between the two generator variations. The average $\Delta\chi^2/NDF$ value across all considered variables is used as a single metric for the performance of the CARL reweighting.

8.4 Applying CARL Weights to Reconstruction Level Events

The CARL weight derivation is performed using simulated events at the parton or particle level. A key part of the technique that has been developed as part of this thesis is that the weights can be then be applied to a sample that has passed the detector simulation, digitisation, and reconstruction stages of the MC production chain. This new technique constructs a map at the moment the weights are derived to pair unique event numbers to the CARL weight assigned to that event. This allows the effects of the generator variation on the analysis to be observed without requiring the computing resources it would have taken to produce a supplementary sample conventionally.

It was explained in this chapter how simulation samples produced using one event generator configuration can be reweighted to appear as if another was used. The procedure for training a neural network to derive the CARL weights required for this was outlined, and it was explained how the performance of the technique can be evaluated. Chapter 9 and Chapter 10 each use these ideas to determine the impact of generator uncertainties on a different aspect of the $H \to \gamma\gamma$ analysis.

References

[57] Leonora Vesterbacka and Stephen Jiggins. *CARL-Torch - GitHub*. 2020. URL: `https://github.com/leonoravesterbacka/carl-torch` (visited on 24/08/2021).

[58] Gilles Louppe, Kyle Cranmer and Juan Pavez. *carl: a likelihood-free inference toolbox*. Mar. 2016. URL: `https://dx.doi.org/10.5281/zenodo.47798` (visited on 24/08/2021).

[59] Adam Paszke et al. 'PyTorch: An Imperative Style, High-Performance Deep Learning Library'. In: *Advances in Neural Information Processing Systems 32*. Ed. by H. Wallach et al. Curran Associates, Inc., 2019, pp. 8024–8035. URL: `https://papers.neurips.cc/paper/9015-pytorch-an-imperative-style-high-performance-deep-learning-library.pdf`.

[60] Kyle Cranmer, Juan Pavez and Gilles Louppe. *Approximating Likelihood Ratios with Calibrated Discriminative Classifiers*. 2016. arXiv: 1506.02169 [stat.AP].

[61] Lutz Roeder. *Netron - GitHub*. 2021. URL: https://github.com/lutzroeder/netron (visited on 06/08/2021).

[62] Vinod Nair and Geoffrey E. Hinton. 'Rectified Linear Units Improve Restricted Boltzmann Machines'. In: ICML'10. Haifa, Israel: Omnipress, 2010, pp. 807–814. ISBN: 9781605589077.

[63] Jun Han and Claudio Moraga. 'The Influence of the Sigmoid Function Parameters on the Speed of Backpropagation Learning'. In: *Proceedings of the International Workshop on Artificial Neural Networks: From Natural to Artificial Neural Computation*. IWANN '96. Berlin, Heidelberg: Springer-Verlag, 1995, pp. 195–201. ISBN: 3540594973.

[64] Shie Mannor, Dori Peleg and Reuven Rubinstein. 'The Cross Entropy Method for Classification'. In: *Proceedings of the 22nd International Conference on Machine Learning*. ICML '05. Bonn, Germany: Association for Computing Machinery, 2005, pp. 561–568. ISBN: 1595931805. DOI: 10.1145/1102351.1102422.

[65] Sashank J. Reddi, Satyen Kale and Sanjiv Kumar. 'On the Convergence of Adam and Beyond'. In: *International Conference on Learning Representations*. 2018. URL: https://openreview.net/forum?id=ryQu7f-RZ.

[66] I.M. Chakravarti, R.G. Laha and J. Roy. *Handbook of Methods of Applied Statistics*. Handbook of Methods of Applied Statistics Vol. 1. John Wiley and Sons, 1967, pp. 392–394. URL: https://books.google.co.uk/books?id=IdI-AAAAIAAJ.

[67] Michael L. Meistrell. 'Evaluation of neural network performance by receiver operating characteristic (ROC) analysis: examples from the biotechnology domain'. In: *Computer Methods and Programs in Biomedicine* 32.1 (1990), pp. 73–80. ISSN: 0169-2607. DOI: 10.1016/0169-2607(90)90087-P.

Chapter 9

Generator Uncertainties for $tHqb$ Signal Samples

This chapter will apply the multivariate CARL techniques from Chapter 8 to reweight $tHqb$ events generated in the *4-flavour* scheme to the *5-flavour* scheme. The reweighting is then applied at the reconstruction level and used to estimate this particular generator systematic uncertainty on the $H \to \gamma\gamma$ analysis measurements, avoiding the production of an additional sample.

9.1 Comparing 4-Flavour and 5-Flavour Event Generation Schemes

The considered event generation variation in this study regards the parton distribution functions of the colliding protons. In the 5-flavour event generation of $tHqb$ events, b-quarks are included in the parton distribution function; differing from 4-flavour generation where they are excluded. Figure 9.1 displays the Feynman diagrams of the $tHqb$ production process for both generator schemes and highlights the difference in the matrix element. The final state is the same in both cases, but the 4-flavour matrix element has an initial state of qg whilst the 5-flavour matrix element begins with qb. As a direct result, the final state b-quark is not included in the matrix element for the 5-flavour scheme (shown in black in Figure 9.1b), but arises instead from an initial gluon splitting ($g \to \bar{b}b$). This ultimately results in differing kinematic distributions of the final state particles

for the two generator settings that will form the basis of the reweighting and the systematic we wish to study.

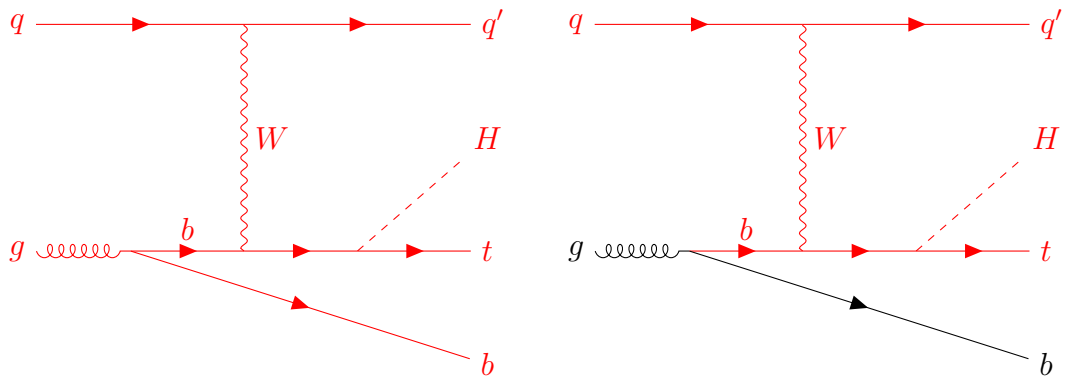

(a) *4-flavour event generation.* **(b)** *5-flavour event generation.*

Figure 9.1 *The 4-flavour and 5-flavour event generation schemes for the $tHqb$ final state. Particles in red are included in the matrix element.*

The 4-flavour and 5-flavour schemes have complementary benefits. On one hand, the 4-flavour scheme provides a more accurate description of the final state b-quark kinematics, due to its inclusion in the matrix element calculation. Whereas in the 5-flavour scheme the b-quark kinematics are predicted by the parton shower, which is only accurate for soft or collinear $g \to b\bar{b}$ splitting. Consequently, the 4-flavour scheme is used as a nominal prediction for the event shapes, while the 5-flavour scheme, in which the b-quark is accounted for in the parton distribution function, provides a more accurate inclusive cross-section, and a more accurate momentum prediction for the b-quark shown in red in Figure 9.1b.

The events used in this chapter are generated with the MadGraph_aMC@NLO generator at *next-to-leading order* (NLO) accuracy in perturbative QCD. The matrix element diagrams in Figure 9.1 may therefore also contain a gluon radiated from one of the quarks, referred to as the *first QCD emission*.

9.2 Derivation of CARL Weights

CARL weights were derived as described in Chapter 8, this section presents the results of the reweighting. Since the generator variation under study occurs at the matrix element level, parton level kinematics are used. This avoids the dilution of differences introduced by showering and hadronisation, which are performed

by the PYTHIA 8 generator. The training variables used for the network were constructed from the final state particles, they were:

- the transverse momentum, pseudorapidity, azimuthal angle, and energy (p_T, η, ϕ, E) Lorentz vectors of the final state q, H, t, and b particles, as well as the first QCD emission;
- the pseudorapidity separation and angle between the final state top quark and Higgs ($\eta(t, H)$ and $\theta(t, H)$ respectively);
- the reconstructed invariant mass of the top-Higgs system, m_{tH};
- and the pseudorapidity separation, angle, and spatial separation of the top-Higgs system and the bottom quark ($\eta(tH, b)$, $\theta(tH, b)$, and $\Delta R(tH, b)$ respectively).

The input 4-flavour and 5-flavour samples each contained 200 000 events. These were then randomly split 3:1 to result in a 150 000 event sample used exclusively to train the network, while the remaining 50 000 events were then used as a validation sample. The reweighting performance is evaluated using a test sample containing 400 000 events, orthogonal to both the training and validation samples.

9.2.1 Training the Neural Network

The network hyperparameters were determined using the process outlined in Section 8.2.1. It was found that the optimal batch size was 1024 events, and the selected initial learning rate was 0.001 decaying to 0.0001 over the course of the training.

Some variable distributions from the list of input variables were considered more critical for the reweighting than others. Key variables were identified as those that exhibited a greater discrepancy in distribution between the 4-flavour and 5-flavour samples, which are important for training the network classifier; and variables that directly affect the classification of $tHqb$ events in the $H \to \gamma\gamma$ analysis. When calculating the mean of the KS_{Impr} score, as defined in Equation 8.6, the identified key values were assigned weights to reflect their importance in selecting the neural network architecture. The KS_{Impr} score of the distributions in $p_T(b)$, $\eta(b)$, $\Delta\eta(t, H)$, $\theta(t, H)$, m_{tH}, $\Delta\eta(tH, b)$, $\theta(tH, b)$, and $\Delta R(tH, b)$ were given a

weight of 2 when calculating their mean to signify them as the most critical. The KS_{Impr} score for $p_T(H)$, $\eta(H)$, $p_T(t)$, and $\eta(t)$ were weighted by 1, and all other variables were disregarded for the choice of network architecture. The results for the average KS score improvement for each tested architecture are presented in Table 9.1. Also shown are the orders of magnitude of the spread in the resulting CARL weights applied by the different neural networks. This spread is an important consideration, as events that are assigned weights of very high relative values become dominant in the sample. This effectively reduces the statistical significance of the sample as events assigned with low value weights become negligible. As such, smaller spreads are preferred.

Table 9.1 *The weighted mean Kolmogorov-Smirnov test statistic improvement scores for different neural network architectures. The selected node configuration for the three hidden layers is shown in bold.*

Network Architecture	KS Improvement Score [%]	$\log_{10}$(Spread of Weights)
27, 27, 27	8.9	5.3
27, 13, 13	20.4	4.8
27, 13, 6	**23.4**	**3.5**
13, 13, 13	22.3	3.5
13, 9, 6	22.0	3.7
13, 6, 6	16.7	3.7
9, 9, 9	23.1	2.9
6, 6, 6	8.0	1.1

Apropos of these results, the (27, 13, 6) node architecture of the three hidden layers was selected, resulting in the neural network configuration depicted in Figure 9.2.

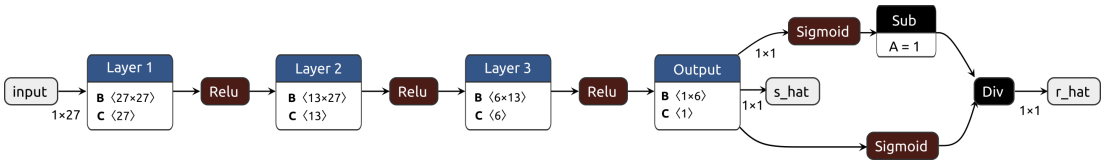

Figure 9.2 *The neural network structure as used in this chapter to reweight 4-flavour generated $tHqb$ events to 5-flavour, visualised using Netron [61].*

9.2.2 CARL Reweighting Performance

The performance of the (27, 13, 6) neural network training was evaluated as described in Section 8.3. To prevent the network from training on behaviour caused by large random statistical fluctuations of the input samples, outlier training events for which any of the input variables were more than five standard

deviations from the mean value of that variable distribution over the training sample were trimmed. This resulted in the removal of around 3.5 % of events before training.

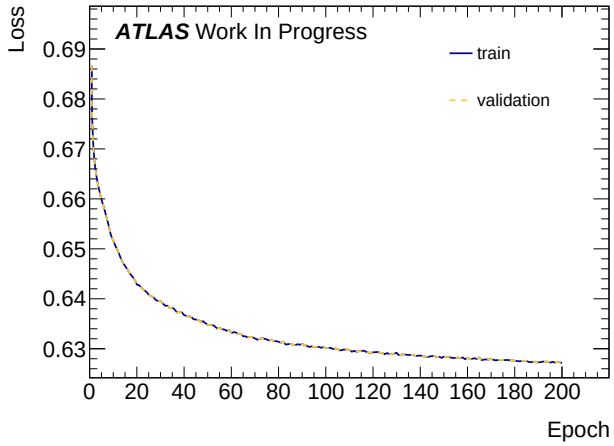

Figure 9.3 *Loss values as a function of epoch when training the CARL neural network on the training and validation samples.*

The loss value as a function of epoch is shown in Figure 9.3 for the training and validation samples. The loss function evaluated on the training sample is within 0.9 % agreement with the validation loss, indicating no overtraining. Additionally, the loss function reaches a plateau at high epoch numbers, indicating the training was sufficiently long for the results to be close to optimal.

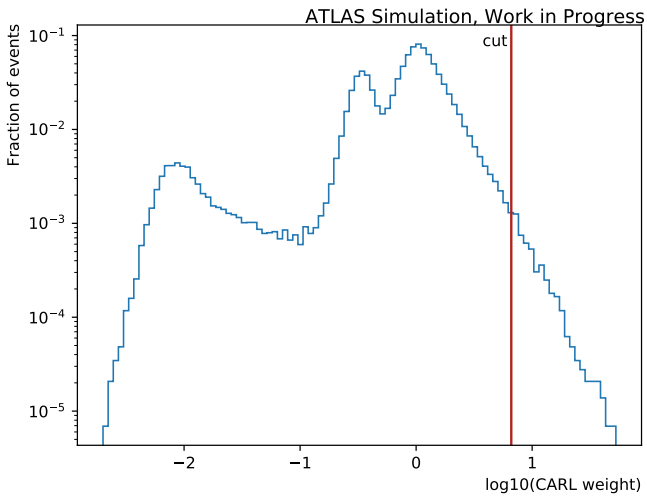

Figure 9.4 *The spread of CARL weights derived by the neural network for the validation samples. The red 'cut' line displays the threshold for weights greater than 5σ from the mean.*

The spread of derived CARL weights applied to 4-flavour events in the validation sample is shown in Figure 9.4. To prevent large weights reducing the statistical

significance of the sample by greatly lessening the contribution of events assigned much smaller weights, a cut is placed on outlier events assigned a weight more than five standard deviations from the mean. This cut removes 0.5 % of events from the validation sample.

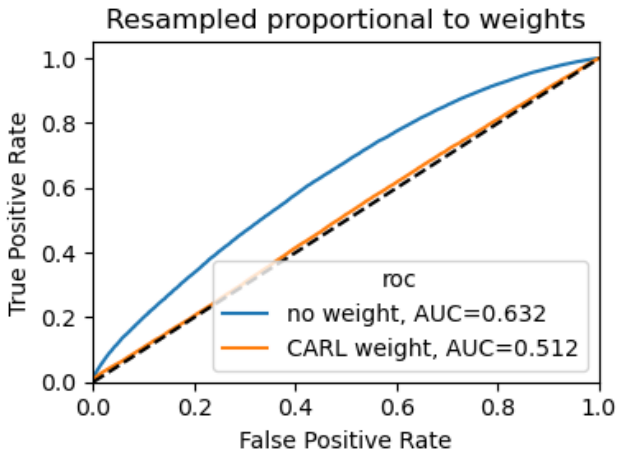

Figure 9.5 *Validation sample ROC curves for the neural network classifier trained to distinguish 4-flavour and 5-flavour generated tHqb events. The blue curve is the performance of the classifier in distinguishing unweighted 4-flavour events, while the orange shows that of the performance on CARL weighted events.*

Figure 9.5 shows ROC curves of a second network trained to distinguish 4-flavour from 5-flavour events for the validation sample. The difference in performance is compared for when the 4-flavour events are unweighted and when the CARL weights are applied. The AUC = 0.512 for the CARL weighted validation sample, which is significantly closer to 0.5 than the AUC = 0.632 for the unweighted events, indicating that the derived CARL weights are having the desired effect.

Reweighting Results in each Variable

The reweighting performance was evaluated with Equation 8.7, using the scores from the unweighted ($\chi^2/NDF_{\text{4-fl}}$) and the CARL weighted ($\chi^2/NDF^{\text{CARL}}_{\text{4-fl}}$) distributions with respect to the target 5-flavour distributions. In addition to the mean value of the $\Delta\chi^2/NDF$ scores from all considered variables, a *weighted mean* was also calculated from the key variables identified in Section 9.2.1 by applying the same weights to the scores in these distributions. The results are shown in Table 9.2.

Table 9.2 *The χ^2/NDF values of the unweighted and CARL weighted 4-flavour variable distributions when compared to the 5-flavour distributions, ordered by $\Delta\chi^2/NDF$.*

Variable	Performance Weight	$(\chi^2/NDF_{\text{4-fl}})$	$(\chi^2/NDF^{\text{CARL}}_{\text{4-fl}})$	$\Delta\chi^2/NDF$	Weighted $\Delta\chi^2/NDF$
$p_T(b)$	2	1773.64	88.59	1685.05	3370.10
$\Delta\eta(tH,b)$	2	840.81	13.76	827.05	1654.10
$\Delta R(tH,b)$	2	490.00	7.12	482.88	965.76
$\theta(t,H)$	2	345.77	8.77	337.00	674.00
$\theta(tH,b)$	2	247.62	10.37	237.25	474.50
$\eta(b)$	2	143.40	3.76	139.64	279.28
$p_T(t)$	1	124.16	5.02	119.13	119.13
$\Delta\eta(t,H)$	2	121.64	2.71	118.93	237.86
m_{tH}	2	29.36	2.19	27.17	54.34
$\eta(t)$	1	24.84	1.89	22.95	22.95
$p_T(em)$	–	36.38	29.27	7.11	–
$p_T(H)$	1	19.67	13.69	5.98	5.98
$E(t)$	–	5.93	0.90	5.03	–
$\eta(q)$	–	3.92	2.00	1.92	–
$E(em)$	–	3.04	1.51	1.53	–
$\eta(H)$	1	2.60	1.94	0.66	0.66
$E(H)$	–	2.61	2.54	0.07	–
$\phi(em)$	–	0.61	0.81	-0.20	–
$\phi(H)$	–	1.09	1.82	-0.73	–
$E(q)$	–	3.03	4.73	-1.70	–
$\phi(b)$	–	0.67	2.74	-2.07	–
$\eta(em)$	–	0.96	5.51	-4.56	–
$\phi(t)$	–	0.95	5.53	-4.58	–
$\phi(q)$	–	0.86	6.80	-5.94	–
$E(b)$	–	24.69	31.81	-7.13	–
$p_T(q)$	–	52.69	105.99	-53.30	–
			Mean	**151.51**	**392.93**

The weighted mean of the $\Delta\chi^2/NDF$ improvements is calculated to be **393**. When considering all variable distributions and giving each an equal consideration, the $\Delta\chi^2/NDF$ improvement mean is found to be **151**.

The variable distributions for those with the four best (top four variables in Table 9.2) and two worst (bottom two variables in Table 9.2) improvements are shown in Figure 9.6.

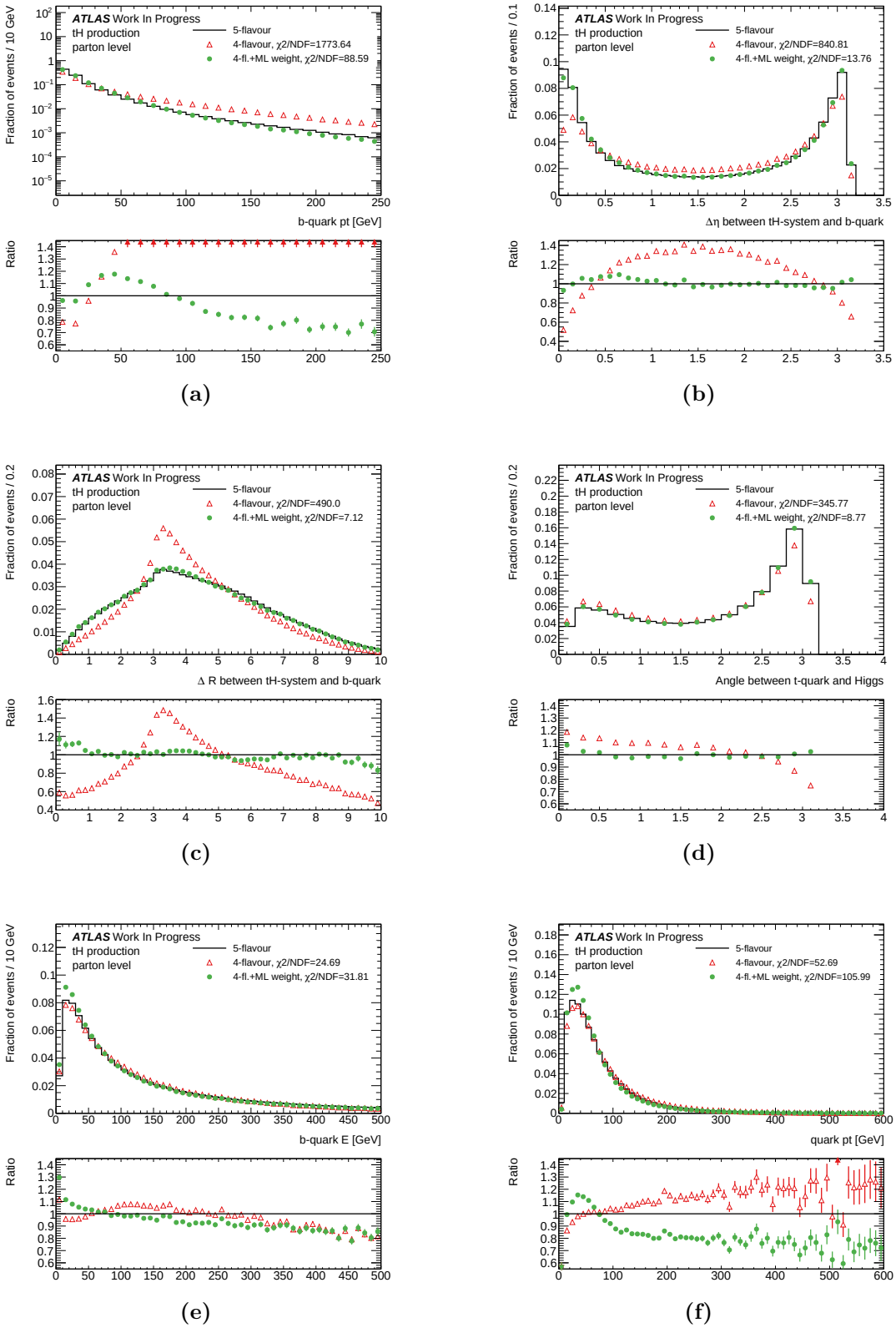

Figure 9.6 *Comparing the distributions of the CARL weighted and unweighted 4-flavour tHqb events to 5-flavour for the variables with the four greatest ((a)–(d)) and two least ((e)–(f)) $\Delta\chi^2/NDF$ improvement scores.*

For $p_T(b)$ in Figure 9.6a, the greatest improvement in χ^2/NDF is shown, but a noticeable shape difference remains after CARL weighting, whereas the distributions of $\Delta\eta(tH, b)$, $\Delta R(tH, b)$, and $\theta(t, H)$ in Figures 9.6b–9.6d show satisfactory closure. On the other hand, a worsening in agreement with the 5-flavour distribution is shown in Figures 9.6f–9.6e when applying the weights. The modelling of the final state light quark kinematics is not a priority in the classification of tH event categories, so the reweighting in Figure 9.6f is considered acceptable.

In Figures 9.6a and 9.6e, the difficulty in reweighting $p_T(b)$ and $E(b)$ partially stems from the b-quark mass. The 4-flavour scheme uses massive b-quarks ($m_b \sim 4.5\,\text{GeV}$), whereas the 5-flavour scheme assumes the b-quarks are massless. The massless b-quark assumption in the 5-flavour scheme is required for them to participate in the parton distribution function [68]. Due to the difference in mass, the exact reweighting of the b-quark four-momentum from 4-flavour to 5-flavour scheme is impossible. This causes the b-quark energies to be mismodelled at low values for the CARL weighted sample, and since most events have low $p_T(b)$ and $E(b)$ then this translates to the mismodelling in the tails of the distributions as well.

Comparison with 1D Reweighting

The performance of a traditional 1D reweighting is evaluated as a comparison for the more novel multivariate CARL method. As the $p_T(b)$ variable distribution exhibits the largest discrepancy between the 4-flavour and 5-flavour event generation schemes, it is used to derive the distribution of 1D weights to be applied. Taking the large statistic 150 000 training samples, a ratio of the 5-flavour, $f_{\text{5-fl}}(p_T(b))$, to the 4-flavour, $f_{\text{4-fl}}(p_T(b))$, $p_T(b)$ distribution is taken,

$$w(p_T(b)) = \frac{f_{\text{5-fl}}(p_T(b))}{f_{\text{4-fl}}(p_T(b))}, \tag{9.1}$$

where $w(p_T(b))$ is the derived weight distribution as a function of $p_T(b)$. This ratio is then rebinned and smoothed to produce the distribution of weights as depicted in Figure 9.7a. The other plots in Figure 9.7 show the performance of this 1D reweighting in three variable distributions.

Figure 9.7b shows that this 1D reweighting achieves excellent closure with the

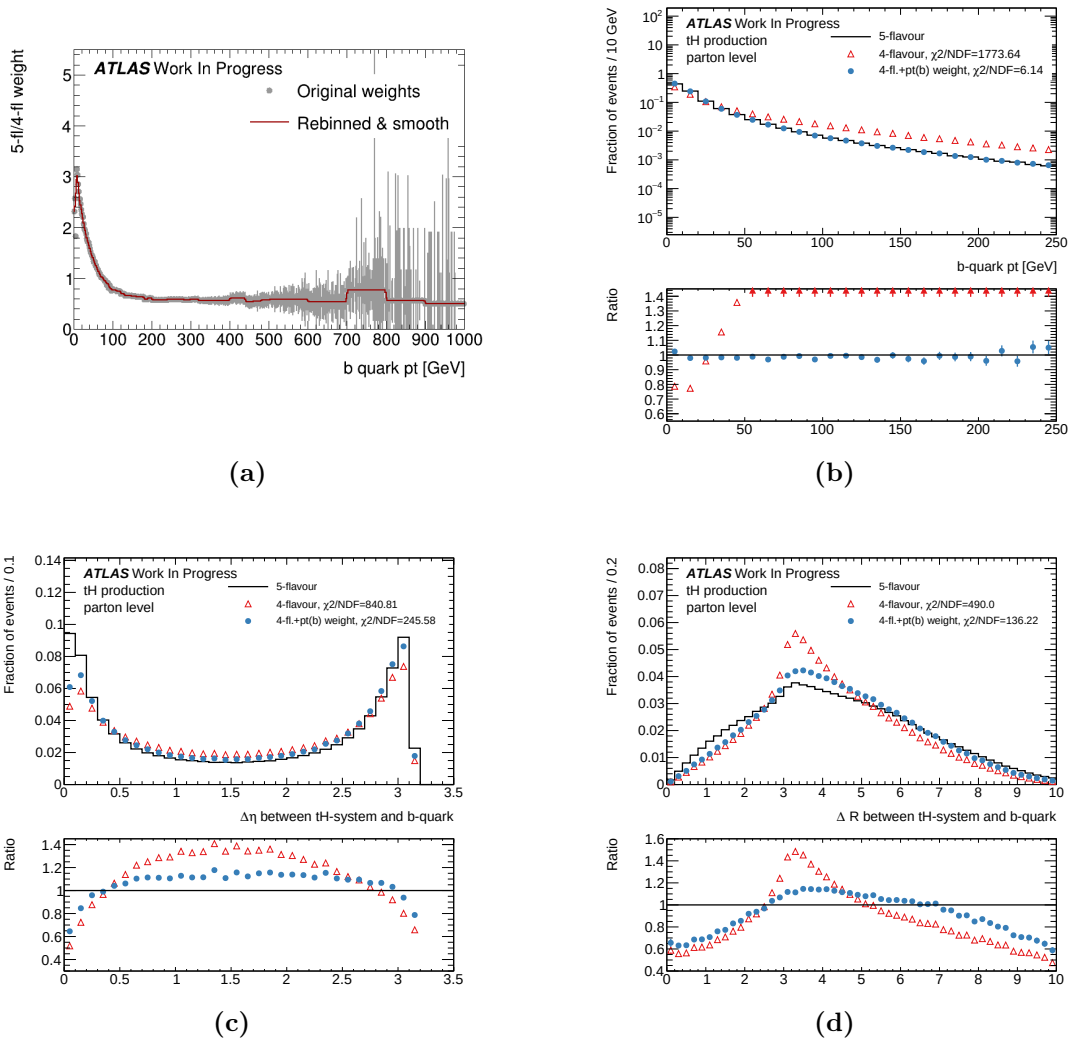

Figure 9.7 *Distribution of 1D weights derived for reweighting 4-flavour generated $tHqb$ events to 5-flavour, and three variable distributions showing the effects of the reweighting.*

5-flavour distribution as expected when using $p_T(b)$ as the reweighting variable. However, Figures 9.7c and 9.7d show a much smaller improvement. When compared with Figures 9.6b and 9.6c from the CARL reweighting, it is seen that the closure from CARL reweighting is significantly better in $\Delta\eta(tH, b)$ and $\Delta R(tH, b)$.

The $tHqb$ traditional 1D reweighting performance weighted mean of the $\Delta\chi^2/NDF$ improvements for the key variables described in Section 9.2.2 is evaluated to be **336**. When considering all variable distributions from Table 9.2 and giving each an equal consideration, the mean of the $\Delta\chi^2/NDF$ improvements is found to be **128**. These improvements are smaller than the weighted (393) and unweighted

(151) improvements obtained with CARL weighting, which demonstrates that the CARL multivariate reweighting method provides superior performance in remodelling the 4-flavour $tHqb$ sample to 5-flavour.

9.3 Effects of $tHqb$ Generation on $H \to \gamma\gamma$ Signal Categorisation

CARL weights were assigned to reconstruction level 4-flavour events using an event weight map to emulate a 5-flavour sample, as described in Section 8.4. When assessing the effect the emulated 5-flavour sample has on the results of the $H \to \gamma\gamma$ analysis when compared to results produced using 4-flavour generated samples, the most important metric is how much the efficiency of passing tH categorisation changes, as described in Section 6.4.1. Categories with a negligible contribution of $tHqb$ events are omitted from this study, as such the considered relevant categories and their abbreviations are:

- `TTH_PTH_0_60__0`: $t\bar{t}H$ ($0 < p_T^H \leq 60\,\text{GeV}$, High-purity),
- `TTH_PTH_0_60__1`: $t\bar{t}H$ ($0 < p_T^H \leq 60\,\text{GeV}$, Med-purity),
- `TTH_PTH_60_120__0`: $t\bar{t}H$ ($60 < p_T^H \leq 120\,\text{GeV}$, High-purity),
- `TTH_PTH_60_120__1`: $t\bar{t}H$ ($60 < p_T^H \leq 120\,\text{GeV}$, Med-purity),
- `TTH_PTH_120_200__0`: $t\bar{t}H$ ($120 < p_T^H \leq 200\,\text{GeV}$, High-purity),
- `TTH_PTH_120_200__1`: $t\bar{t}H$ ($120 < p_T^H \leq 200\,\text{GeV}$, Med-purity),
- `TTH_PTH_200_300__0`: $t\bar{t}H$ ($200 < p_T^H \leq 300\,\text{GeV}$),
- `TTH_PTH_GT300__0`: $t\bar{t}H$ ($p_T^H \geq 300\,\text{GeV}$),
- `THJB__0`: $tHjb$ (High-purity),
- `THJB__1`: $tHjb$ (Med-purity),
- `THJB_minus1`: $tHjb$ ($\kappa_t = -1$),
- `THW`: tHW.

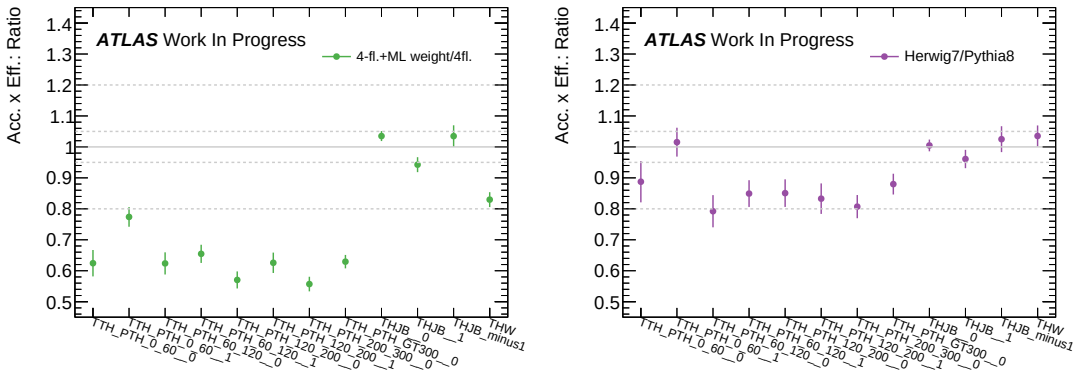

(a) *CARL emulated 5-flavour versus nominal 4-flavour event generation.*

(b) *Herwig 7 versus nominal Pythia 8 showering in $tHqb$ event generation.*

Figure 9.8 *Comparing the event yield (acceptance multiplied by efficiency) as a ratio between two samples for the relevant $H \to \gamma\gamma$ analysis categories to demonstrate the effects of two separate event generator variations. The first dotted band about the ratio value of 1 denotes a variation of 5 %, while the second marks 20 %.*

Figure 9.8a displays event yields as acceptance multiplied by efficiency, calculated as a ratio of the emulated 5-flavour sample to the 4-flavour sample for the relevant analysis categories. The most important categories are `TH*`, while `TTH*` are less so due to fewer selected $tHqb$ events. The `THJB*` categories are enriched in $tHqb$ events and are sensitive to the sign of the top Yukawa coupling, y_t, as described in Section 2.4.2. By defining the ratio $\kappa_t = y_t/y_t^{\mathrm{SM}}$, where y_t^{SM} is the SM predicted value for the top Yukawa coupling, the `THJB__0` and `THJB__1` categories target the Standard Model case by selecting events compatible with $\kappa_t = +1$, whilst the `THJB__minus1` category targets the BSM scenario in which $\kappa_t = -1$. It is evident that the event yields in the `TH*` categories vary by less than 5 % between the CARL emulated 5-flavour sample and the nominal 4-flavour sample.

To demonstrate the scale of effects caused by the 4-flavour/5-flavour variation, a $tHqb$ parton shower modelling systematic is shown in Figure 9.8b. Here, the differences in event yields are caused by using Herwig 7 in place of the Pythia 8 generator used for the nominal sample. In the `THJB*` categories, the differences between the 4-flavour and 5-flavour schemes are found to be of comparable sizes to the differences between Pythia 8 and Herwig 7.

Finally, the effect of the 4-flavour versus 5-flavour $tHqb$ event generation scheme variation on the determination of the value of κ_t is shown in Figure 9.9. It can be observed that the CARL emulated 5-flavour sample differs from the 4-flavour

sample most at low discriminant values in Figures 9.9a–9.9c. This corresponds to signals with a small fraction of the $tHqb$ events. The excess at high discriminant values is partially compensated by the smaller acceptance of the reweighted sample, yielding a less significant change in the event yield of $tHqb$ signal in these categories.

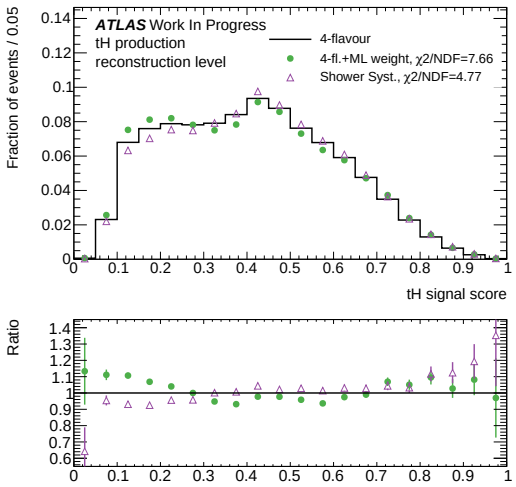

(a) *Neural network discriminant used to select the tH categories.*

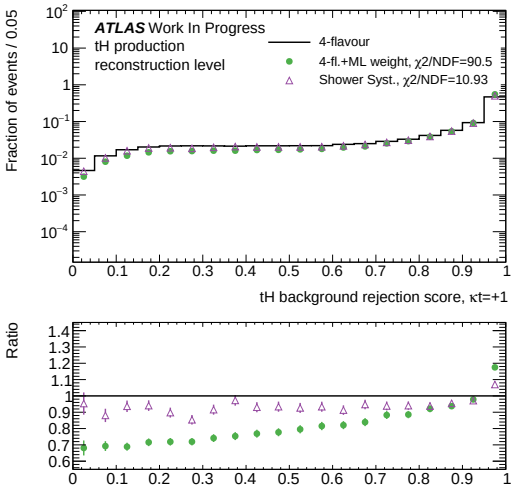

(b) *Non-resonant background rejection discriminant results for the κ_t = +1 category.*

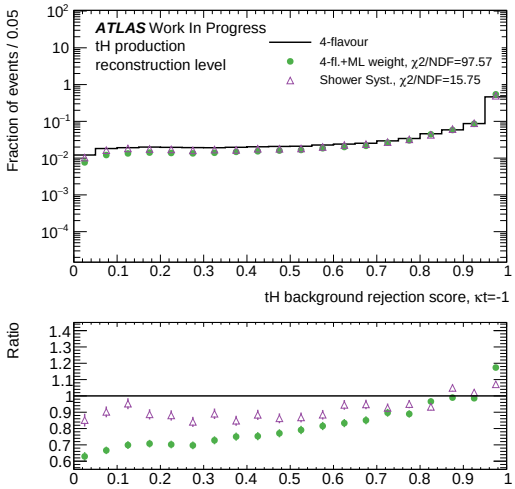

(c) *Non-resonant background rejection discriminant results for the κ_t = -1 category.*

Figure 9.9 *Comparing the effects of the PYTHIA 8 showered CARL emulated 5-flavour event generator scheme ('4-fl.+ML weight') and the HERWIG 7 showered 4-flavour scheme ('Shower Syst.') to the nominal PYTHIA 8 showered 4-flavour scheme ('4-flavour') on the selection of tHqb signal events for κ_t categorisation.*

In this chapter, it was described how to use the CARL reweighting technique from Chapter 8 to emulate a 5-flavour generated sample of $tHqb$ signal events using a 4-flavour sample. This reweighting method was shown to be superior to a traditional reweighting using one dimension for these samples. Assigning CARL weights to 4-flavour events at the reconstruction level showed that the difference in generators does not significantly affect the event yield in tH categories beyond the current systematic uncertainty. This knowledge improves the reliability of estimating the $tHqb$ production cross-section.

References

[61] Lutz Roeder. *Netron - GitHub*. 2021. URL: https://github.com/lutzroeder/netron (visited on 06/08/2021).

[68] Frank Krauss and Davide Napoletano. 'Towards a fully massive five-flavor scheme'. In: *Phys. Rev. D* 98.9 (2018), p. 096002. DOI: 10.1103/PhysRevD.98.096002. arXiv: 1712.06832 [hep-ph].

Chapter 10

Generator Uncertainties for $V\gamma\gamma$ Background Samples

After describing a novel method for estimating event generator uncertainties when modelling the signal shape for $tHqb$ events in Chapter 9, this chapter applies the same multivariate CARL reweighting technique described in Chapter 8 to estimate the generator uncertainty for modelling background shapes. The variation under consideration is the difference in producing $V\gamma\gamma$ background samples for VH measurements in the $H \to \gamma\gamma$ analysis using Sherpa@LO or MadGraph_aMC@NLO event generation.

10.1 $V\gamma\gamma$ Event Generation

As described in Section 6.5.2, simulated $V\gamma\gamma$ events are used to construct the background templates in the VH production mode analysis categories. The classification of VH events in the $H \to \gamma\gamma$ analysis only considers leptonic decays of the vector boson ($Z \to \ell\ell$, $Z \to \nu\nu$, and $W \to \ell\nu$). Hadronic decays of the vector boson ($Z \to q\bar{q}$, and $W \to qq'$) are instead included in the measurement of $qq' \to Hqq'$ processes, as described in Section 6.4. The simulated background samples used in this chapter are composed of $Z\gamma\gamma$ and $W\gamma\gamma$ events, where the photons are not from the decay of a Higgs boson. The vector boson is decayed leptonically, resulting in $\ell\ell\gamma\gamma$ events for $ZH \to \ell\ell\gamma\gamma$ background processes, and $\ell\nu\gamma\gamma$ events for $WH \to \ell\nu\gamma\gamma$ background. The $ZH \to \nu\nu\gamma\gamma$

background modelling uncertainty only has a small impact on the ZH cross-section measurement uncertainty, thus $\nu\nu\gamma\gamma$ samples are not considered.

The $\ell\ell\gamma\gamma$ and $\ell\nu\gamma\gamma$ samples are produced using MadGraph_aMC@NLO and Sherpa@LO. In both cases, the events are generated with up to two extra partons in the matrix element, but MadGraph_aMC@NLO calculates these at NLO accuracy in perturbative QCD and Sherpa@LO calculates to LO. When compared to experimental data, the MadGraph_aMC@NLO setup provides a better description of dijet production in association with the Z boson [69]. The higher accuracy and better agreement with data motivate the consideration of MadGraph_aMC@NLO for $V\gamma\gamma$ production, but it is considerably more computationally intensive to generate such a sample at full statistical power than with nominal Sherpa@LO generation. Using the CARL process described in Chapter 8, the effects of MadGraph_aMC@NLO simulated events on background modelling for $H \to \gamma\gamma$ measurements can instead be assessed using a reweighted larger statistics sample of Sherpa@LO events.

10.2 Derivation of CARL Weights

To reweight Sherpa@LO samples to MadGraph_aMC@NLO, a separate neural network was trained for the $\ell\nu\gamma\gamma$ and for the $\ell\ell\gamma\gamma$ events. The results for training each network are presented in this section.

10.2.1 Training the Neural Network for $\ell\nu\gamma\gamma$ Events

To train the neural network for assigning CARL weights to $\ell\nu\gamma\gamma$ events, input samples were prepared from 80 000 Sherpa@LO and MadGraph_aMC@NLO generated events. These samples were randomly split 4:1 to create the training and validation samples respectively. The training was performed with stable generator level particles and jets.

The variables considered important at the reconstruction level for the generator reweighting were those responsible for event selection, STXS classification, and non-resonant background rejection for each event. The relevant particles for $\ell\nu\gamma\gamma$ events are the leptons and photons that would be expected from the $W \to \ell\nu$ and $H \to \gamma\gamma$ decays of a signal event, as well as jets. The differences between the

SHERPA@LO and MADGRAPH_aMC@NLO samples were determined from the kinematic Lorentz vectors of these individual particles and jets, in addition to the angles between them and the input variables to the multiclass and binary BDTs described in Section 6.4.1. However, due to the low training statistics available for the samples, training a large network was not feasible and the number of input variables was reduced.

Only the variables with a large discrepancy ($\chi^2/NDF > 4$) between the SHERPA@LO and MADGRAPH_aMC@NLO distributions were considered as inputs to the network. The largest discrepancies were found to be for the multi-jet variables, such as the scalar sum of jet transverse momenta and the sum of jet masses. The diphoton invariant mass was also retained as it is essential that its shape is well modelled by the reweighting. This resulted in 15 input variables to train the network:

- the transverse momentum of the leading photon ($p_T(\gamma_1)$), subleading photon($p_T(\gamma_2)$), leading jet ($p_T(j_1)$), diphoton system ($p_T(\gamma\gamma)$), the leading jet and diphoton system ($p_T(j\gamma\gamma)$), and of the reconstructed lepton and missing transverse energy system ($p_T(\ell E_T^{\text{miss}})$);
- the reconstructed invariant mass of the diphoton system ($m_{\gamma\gamma}$), leading jet and diphoton system ($m_{j\gamma\gamma}$), all jets in the event ($m_{\Sigma j}$), and of the lepton and missing transverse energy system ($m_{\ell E_T^{\text{miss}}}$);
- and the number of jets in the event (N_j), rapidity separation of the two leading jets ($\Delta y(j,j)$), the azimuthal angle separation of the two leading jets ($\Delta\phi(j,j)$), the minimum spatial separation between a photon and a jet ($\Delta R(j,\gamma)$), and the scalar sum of the transverse momenta of all jets in the event (H_T).

Optimising Hyperparameters

The network hyperparameters were determined using the process outlined in Section 8.2.1. It was found that the optimal batch size was 2048 events, and the selected initial learning rate was 0.001 decaying to 0.0001 over the course of the training. Table 10.1 gives the results for the tested neural network architectures.

For architectures with fewer than 15 nodes in the first hidden layer, the initial input variables were reduced by removing those that were highly correlated or had

Table 10.1 *The mean Kolmogorov-Smirnov test statistic improvement scores for different neural network architectures. The test improvement scores are given first as an improvement over the input variables of the indicated architecture, and as an improvement over all 15 of the initial training variables in parentheses for the cases where the number of input nodes are reduced. The selected node configuration for the three hidden layers is shown in bold.*

Network Architecture	KS Test Improvement [%]	$\log_{10}$(Spread of Weights)
15, 15, 10	0.49	1.94
15, 12, 9	0.42	1.85
15, 8, 4	0.47	1.51
12, 12, 9	0.49 (0.38)	1.43
12, 9, 6	**0.55 (0.52)**	**1.26**
12, 6, 3	0.46 (0.43)	1.24
9, 9, 6	0.49 (0.42)	1.22
9, 6, 3	0.40 (0.46)	1.32

smaller discrepancies between the SHERPA@LO and MADGRAPH_aMC@NLO distributions. The correlations between variables for the SHERPA@LO sample is shown in Figure 10.1.

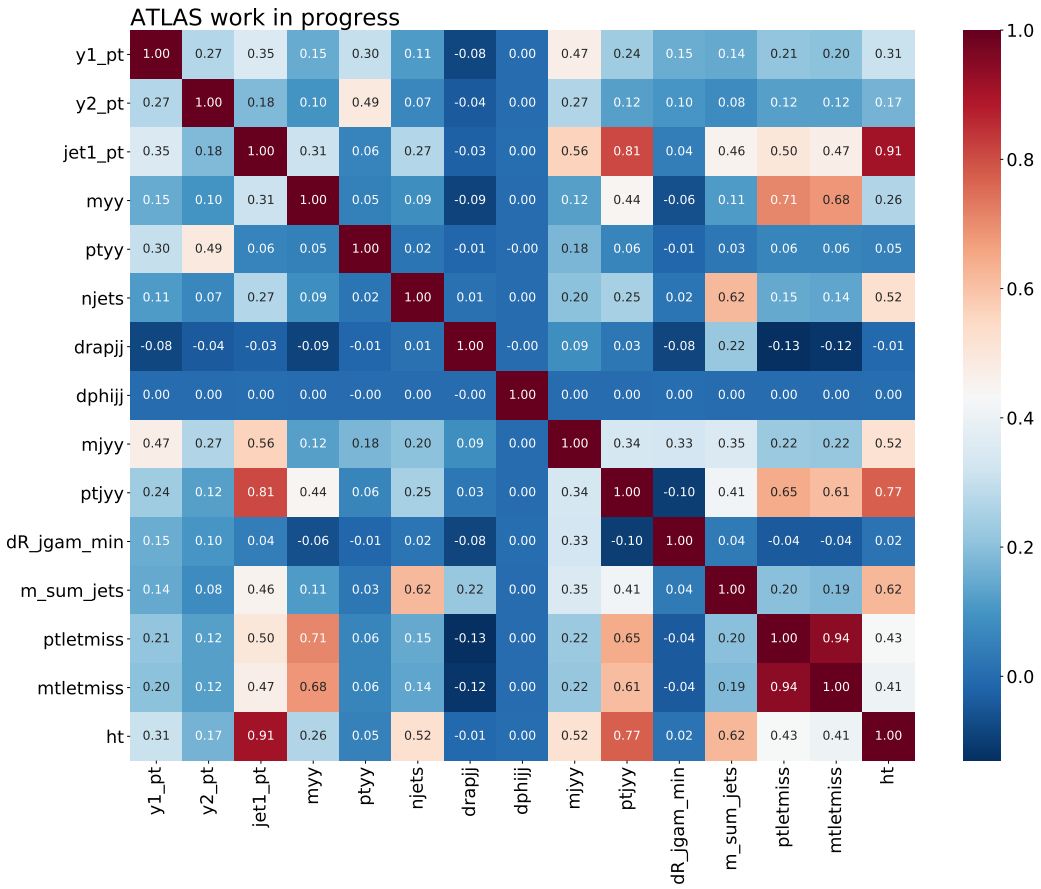

Figure 10.1 *Correlations between training variables for the SHERPA@LO $\ell\nu\gamma\gamma$ sample.*

For the networks shown in Table 10.1 with an initial 12 nodes, the variables dropped were $p_T(\gamma_1)$ due to the small distribution discrepancy, $p_T(j_1)$ due to the high correlation with H_T, and $p_T(\ell E_T^{\text{miss}})$ due to the high correlation with $m_{\ell E_T^{\text{miss}}}$. For the networks with an initial 9 nodes, the variables dropped in addition were $p_T(j\gamma\gamma)$ due to the high correlation with H_T and $m_{\ell E_T^{\text{miss}}}$, $p_T(\gamma\gamma)$ due to the small distribution discrepancy and high correlation with $p_T(\gamma_2)$, and $m_{\Sigma j}$ due to the high correlation with H_T. The average KS test improvement score for these networks is reported in Table 10.1 first as an improvement over the input variables of the indicated architecture, and as an improvement over all 15 of the initial training variables in brackets. Based on these findings, the network architecture of (12, 9, 6) nodes was chosen.

Training Performance

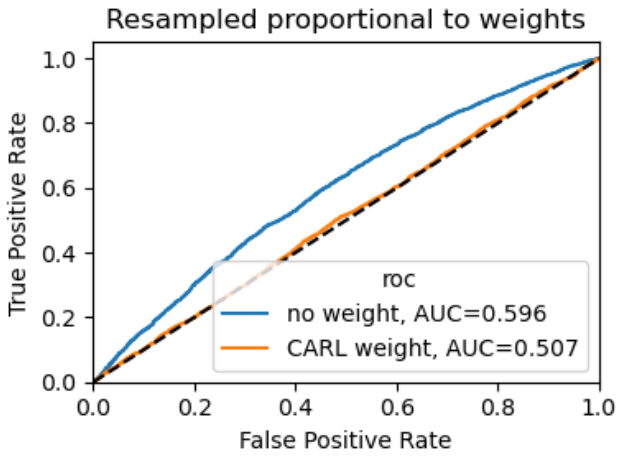

Figure 10.2 *Validation sample ROC curves for the neural network classifier trained to distinguish* Sherpa@LO *and* MadGraph_aMC@NLO *generated* $\ell\nu\gamma\gamma$ *events. The blue curve is the classifier performance in distinguishing unweighted* Sherpa@LO *events, while the orange shows the performance on CARL weighted events.*

The performance of the (12, 9, 6) neural network training was evaluated as described in Section 8.3. Outlier samples comprising around 0.5 % of the input events were trimmed before training. The development of the loss value as a function of training epoch was found to reach a plateau and displayed good agreement between the training and validation functions, indicating there was no overtraining. Additionally, the spread of derived CARL weights assigned to the validation sample was around one order of magnitude, meaning no events required trimming to preserve the statistical significance of the sample.

Figure 10.2 shows ROC curves of a second network trained to distinguish Sherpa@LO from MadGraph_aMC@NLO events for the validation sample. The difference in performance is compared for when the Sherpa@LO events are unweighted and when the CARL weights are applied. The AUC = 0.507 for the CARL weighted validation sample, which is significantly closer to 0.5 than the AUC = 0.596 for the unweighted events, indicating that the derived CARL weights are having the desired effect.

Reweighting Performance

The performance of the CARL reweighting was evaluated using two separate scores: an *exclusive* and an *inclusive* score. The exclusive score considers only the following key variables: $m_{\gamma\gamma}$, which is used in spurious signal fits; the number of jets and $p_T(\gamma\gamma)$, which are used to define the STXS regions; m_{jj} and H_T, as these powerful variables are key to separating VH events from VBF and ggF processes respectively; and the leading jet and lepton transverse momenta. The inclusive score accounts for all variables that determine event selection, STXS classification, and non-resonant background rejection of VH events. The inclusive and exclusive scores are calculated with Equation 8.7, using the scores from the unweighted ($\chi^2/NDF_{\text{Sherpa@LO}}$) and the CARL weighted ($\chi^2/NDF^{\text{CARL}}_{\text{Sherpa@LO}}$) distributions with respect to the target MadGraph_aMC@NLO distributions. The results are shown in Table 10.2.

The $\ell\nu\gamma\gamma$ reweighting exclusive mean of the $\Delta\chi^2/NDF$ improvement is calculated to be **28.84** and the inclusive mean improvement is found to be **7.56**. The variable distributions with the four best (top four variables in Table 10.2) and two worst (bottom two variables in Table 10.2) improvements are shown in Figure 10.3.

Table 10.2 *The χ^2/NDF values of the unweighted and CARL weighted* Sherpa@LO *$\ell\nu\gamma\gamma$ variable distributions when compared to the* MadGraph_aMC@NLO *distributions, ordered by $\Delta\chi^2/NDF$.*

Variable	$(\chi^2/NDF_{\text{Sherpa@LO}})$	$\left(\chi^2/NDF^{\text{CARL}}_{\text{Sherpa@LO}}\right)$	Inclusive $\Delta\chi^2/NDF$	Exclusive $\Delta\chi^2/NDF$
H_T	87.44	12.86	74.58	74.58
N_j	67.90	2.64	65.25	65.25
$p_T(j_1)$	52.62	9.09	43.54	43.54
m_{jj}	21.50	3.39	18.10	18.10
$m_{j\gamma\gamma}$	22.08	6.90	15.18	–
$p_T(j\gamma\gamma)$	16.23	1.24	14.99	–
$\Delta\phi(j,j)$	8.95	2.12	6.84	–
$m_{jj\gamma\gamma}$	8.11	1.68	6.43	–
$\Delta y(j,j)$	6.85	1.69	5.16	–
$p_T(jj)$	5.99	3.31	2.68	–
$\Delta R(\gamma_1,\ell_1)$	3.11	0.94	2.17	–
$p_T(\gamma_2)$	4.63	2.91	1.72	–
$m_{\gamma\gamma}$	3.13	1.65	1.48	1.48
$p_T(\gamma_1)$	3.94	2.50	1.44	–
$\Delta R(j,\gamma)_{\text{min}}$	2.77	2.06	0.71	–
$m_{\ell E_T^{\text{miss}}}$	4.55	3.90	0.66	–
$p_T(jj\gamma\gamma)$	1.93	1.44	0.49	–
$p_T(\ell_1)$	1.35	1.09	0.27	0.27
$\Delta R(\gamma_2,\ell_1)$	1.62	1.38	0.24	–
$\eta(\gamma_2)$	1.34	1.30	0.03	–
$\eta(\ell_1)$	1.42	1.49	-0.06	–
$\Delta\eta(\gamma,\gamma)$	2.06	2.13	-0.07	–
$\eta(\gamma_1)$	1.45	1.59	-0.14	–
$Zepp$	2.67	3.01	-0.33	–
$p_T(\gamma_2)/m_{\gamma\gamma}$	2.74	3.29	-0.54	–
$p_T(\ell E_T^{\text{miss}})$	6.59	7.29	-0.70	–
$\eta(\gamma\gamma)$	1.23	2.08	-0.85	–
$\Delta R(\gamma_1,\gamma_2)$	3.31	4.41	-1.10	–
$p_T(\gamma_1)/m_{\gamma\gamma}$	2.80	4.05	-1.24	–
E_T^{miss}	2.97	4.22	-1.26	–
$p_T(\gamma\gamma)$	2.87	4.20	-1.33	-1.33
$\Delta\eta(jj,\gamma\gamma)$	2.12	4.10	-1.99	–
$m_{\Sigma j}$	27.42	30.15	-2.73	–
		Mean	**7.56**	**28.84**

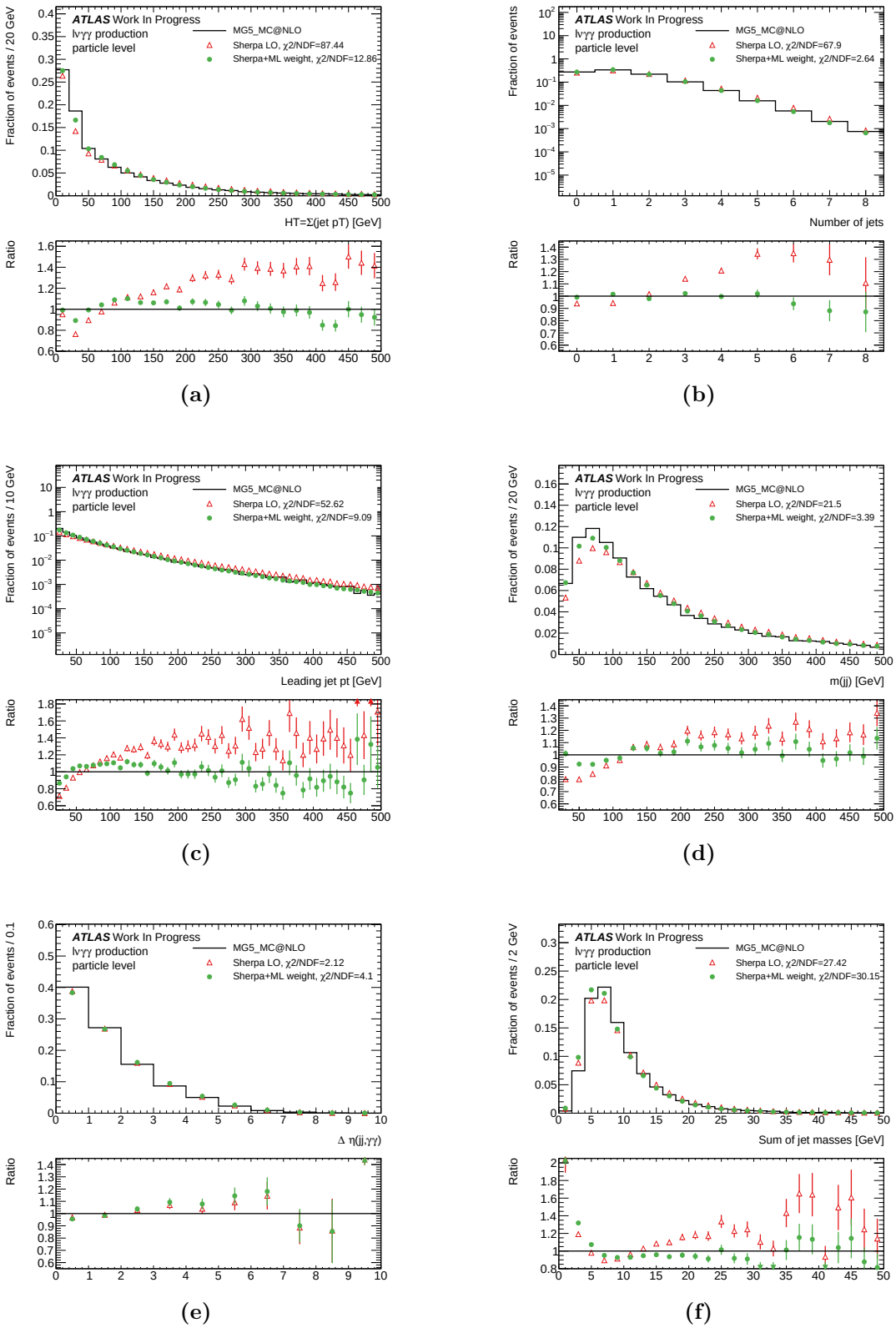

Figure 10.3 *Comparing the distributions of the CARL weighted and unweighted* Sherpa@LO *$\ell\nu\gamma\gamma$ events to* MadGraph_aMC@NLO *for the variables with the four highest ((a)–(d)) and two lowest ((e)–(f)) $\Delta\chi^2/NDF$ improvement scores.*

Comparison with 1D Reweighting

The performance of a traditional 1D reweighting was evaluated as a comparison for the CARL technique. As the N_j variable distribution is critical in defining the analysis STXS regions and exhibits the second largest discrepancy between generator distributions of $\ell\nu\gamma\gamma$ events, it is used to derive the distribution of 1D weights to be applied. Taking a large statistic training sample, a ratio of the MadGraph_aMC@NLO, $f_{\text{MG@NLO}}(N_j)$, to the Sherpa@LO, $f_{\text{SH@LO}}(N_j)$, N_j distribution is taken,

$$w(N_j) = \frac{f_{\text{MG@NLO}}(N_j)}{f_{\text{SH@LO}}(N_j)}, \tag{10.1}$$

where $w(N_j)$ is the derived weight distribution as a function of N_j. The plots in Figure 10.4 show the performance of applying this 1D weight distribution in two variable distributions.

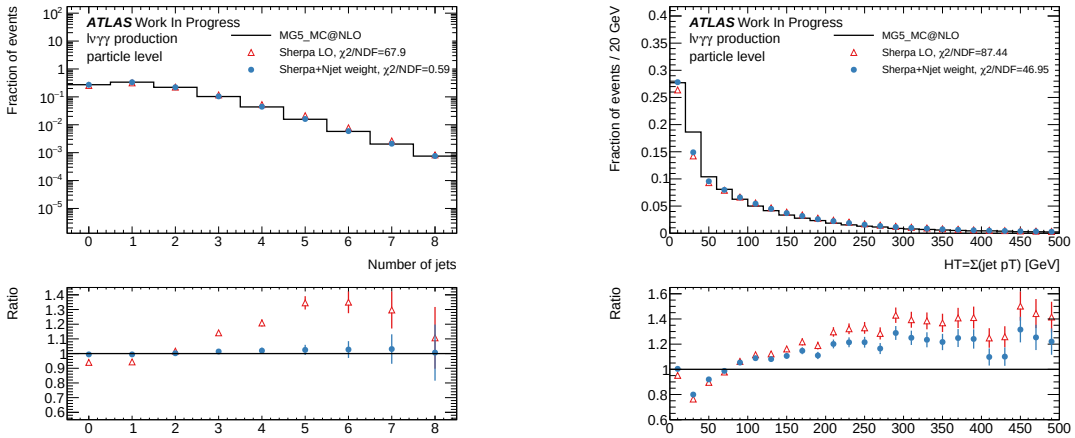

(a) **(b)**

Figure 10.4 *Effects of the one dimensional N_j reweighting of Sherpa@LO $\ell\nu\gamma\gamma$ events to MadGraph_aMC@NLO in N_j and H_T.*

Figure 10.4a shows that this 1D reweighting achieves excellent closure with the MadGraph_aMC@NLO distribution as expected when using N_j as the reweighting variable. However, Figure 10.4b shows signigicantly worse closure in H_T when compared with the CARL technique in Figure 10.3a.

The mean of the exclusive $\Delta\chi^2/NDF$ improvements for the traditional 1D reweighting of $\ell\nu\gamma\gamma$ events was evaluated to be **17.99**, compared to the

multivariate reweighting improvement of 28.84. The inclusive $\Delta\chi^2/NDF$ improvement score mean was found to be **4.35**, compared to the multivariate reweighting improvement of 7.56. The higher improvement scores obtained with CARL multivariate reweighting demonstrates that this method is superior in remodelling the SHERPA@LO $\ell\nu\gamma\gamma$ sample to MADGRAPH_aMC@NLO.

10.2.2 Training the Neural Network for $\ell\ell\gamma\gamma$ Events

The neural network used to derive CARL weights for the $\ell\ell\gamma\gamma$ samples was trained using 12 input variables. These were:

- The transverse momentum of the leading jet ($p_T(j_1)$), the leading lepton ($p_T(\ell_1)$), the reconstructed system of the two leading jets ($p_T(jj)$), and the leading jet and diphoton system ($p_T(j\gamma\gamma)$).
- The invariant mass of the diphoton system ($m_{\gamma\gamma}$), leading jet and diphoton system ($m_{j\gamma\gamma}$), two leading jets (m_{jj}), and the sum of all jets in the event ($m_{\Sigma j}$).
- The number of jets in the event (N_j), the scalar sum of transverse momenta of all jets in the event (H_T), the rapidity separation of the two leading jets ($\Delta y(j,j)$), and the minimum spatial separation between a photon and a jet ($\Delta R(j,\gamma)_{\text{min}}$).

The hyperparameters were optimised using the same process as for the $\ell\nu\gamma\gamma$ network, selecting a (12, 10, 8) hidden layer node architecture, a batch size of 2048 events, and an initial learning rate of 0.001 decaying to 0.0001 by the end of training.

To train the (12, 10, 8) network, input samples were prepared from 150 000 SHERPA@LO and 75 000 MADGRAPH_aMC@NLO events. These samples were randomly split 4:1 to produce the training and validation samples, and outlier events ($\sim$0.7 %) were trimmed before training. The spread of derived CARL weights assigned to the validation sample was around one order of magnitude, meaning no events required trimming to preserve the statistical significance of the sample. In addition, the development of the loss value as a function of training epoch was found to reach a plateau and displayed good agreement between the training and validation functions, indicating that there was no overtraining.

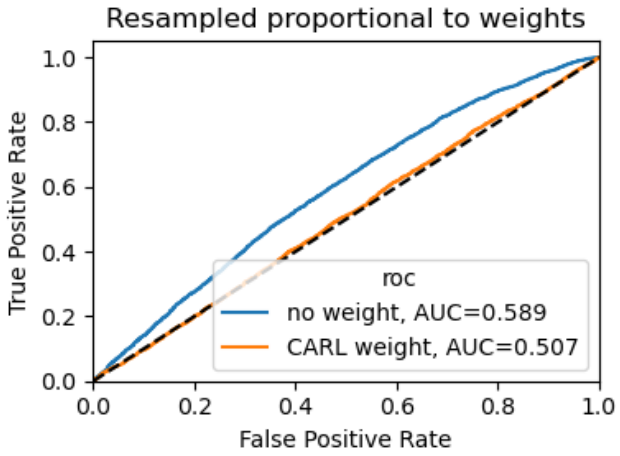

Figure 10.5 *Validation sample ROC curves for the neural network classifier trained to distinguish* Sherpa@LO *and* MadGraph_aMC@NLO *generated* $\ell\ell\gamma\gamma$ *events. The blue curve is the performance of the classifier in distinguishing unweighted* Sherpa@LO *events, while the orange shows that of the performance on CARL weighted events.*

Figure 10.5 shows ROC curves of a second network trained to distinguish Sherpa@LO from MadGraph_aMC@NLO events for the validation sample. The difference in performance is compared for when the Sherpa@LO events are unweighted and when the CARL weights are applied. The AUC = 0.507 for the CARL weighted validation sample, which is significantly closer to 0.5 than the AUC = 0.589 for the unweighted events, again showing that the CARL reweighting performs well overall.

Reweighting Performance

The performance of the CARL reweighting was evaluated using the inclusive and exclusive scores as described in Section 10.2.1. The results are shown in Table 10.3.

The $\ell\ell\gamma\gamma$ reweighting exclusive $\Delta\chi^2/NDF$ improvement mean is calculated to be **27.96** and the inclusive mean improvement is found to be **6.86**. The variable distributions of the four best (top four variables in Table 10.3) and two worst (bottom two variables in Table 10.3) improvements are shown in Figure 10.6.

Table 10.3 *Evaluation χ^2/NDF metrics for the unweighted and CARL weighted* Sherpa@LO *$\ell\ell\gamma\gamma$ variable distributions when compared to the* MadGraph_aMC@NLO *distributions.*

Variable	$(\chi^2/NDF_{\text{Sherpa@LO}})$	$\left(\chi^2/NDF^{\text{CARL}}_{\text{Sherpa@LO}}\right)$	Inclusive $\Delta\chi^2/NDF$	Exclusive $\Delta\chi^2/NDF$
H_T	83.47	12.13	71.34	71.34
N_j	81.10	19.15	61.95	61.95
$p_T(j_1)$	52.67	14.61	38.06	38.06
m_{jj}	27.36	5.72	21.63	21.63
$\Delta\phi(j,j)$	12.08	1.81	10.27	–
$p_T(j\gamma\gamma)$	11.65	2.21	9.44	–
$\Delta y(j,j)$	11.04	2.33	8.71	–
$m_{j\gamma\gamma}$	13.35	5.70	7.65	–
$\Delta R(j,\gamma)_{\text{min}}$	7.03	0.78	6.25	–
$m_{jj\gamma\gamma}$	7.37	4.26	3.11	–
$p_T(\ell_1)$	6.88	4.70	2.18	2.18
$p_T(jj)$	18.13	16.32	1.81	–
$m_{\gamma\gamma}$	2.25	1.39	0.86	0.86
$\Delta R(\gamma_1,\ell_1)$	4.01	3.34	0.67	–
$p_T(\ell\ell)$	2.77	2.32	0.45	–
$\Delta R(\gamma_1,\ell_2)$	2.33	1.88	0.45	–
$\Delta\eta(jj,\gamma\gamma)$	2.92	2.50	0.42	–
$p_T(\gamma_1)$	1.76	1.43	0.33	–
$p_T(\gamma_2)$	1.26	0.97	0.28	–
$p_T(\ell_2)$	2.83	2.66	0.17	–
$\eta(\gamma_1)$	1.12	1.08	0.03	–
$\eta(\ell_1)$	1.43	1.42	0.01	–
$\eta(\gamma\gamma)$	1.09	1.09	0.00	–
$\eta(\gamma_2)$	0.81	0.81	0.00	–
$\Delta R(\gamma_2,\ell_2)$	1.39	1.41	-0.02	–
$\Delta\eta(\gamma,\gamma)$	1.06	1.08	-0.02	–
$\eta(\ell_2)$	3.46	3.52	-0.06	–
$p_T(\gamma_1)/m_{\gamma\gamma}$	1.78	1.94	-0.16	–
$\Delta R(\gamma_2,\ell_1)$	3.50	3.75	-0.26	–
$p_T(\gamma\gamma)$	1.41	1.69	-0.28	-0.28
$p_T(\gamma_2)/m_{\gamma\gamma}$	2.16	2.50	-0.34	–
$\Delta R(\gamma_1,\gamma_2)$	1.53	1.99	-0.45	–
$p_T(jj\gamma\gamma)$	1.68	2.87	-1.19	–
$Zepp$	1.23	3.08	-1.85	–
$m_{\Sigma j}$	33.19	35.39	-2.21	–
		Mean	**6.86**	**27.96**

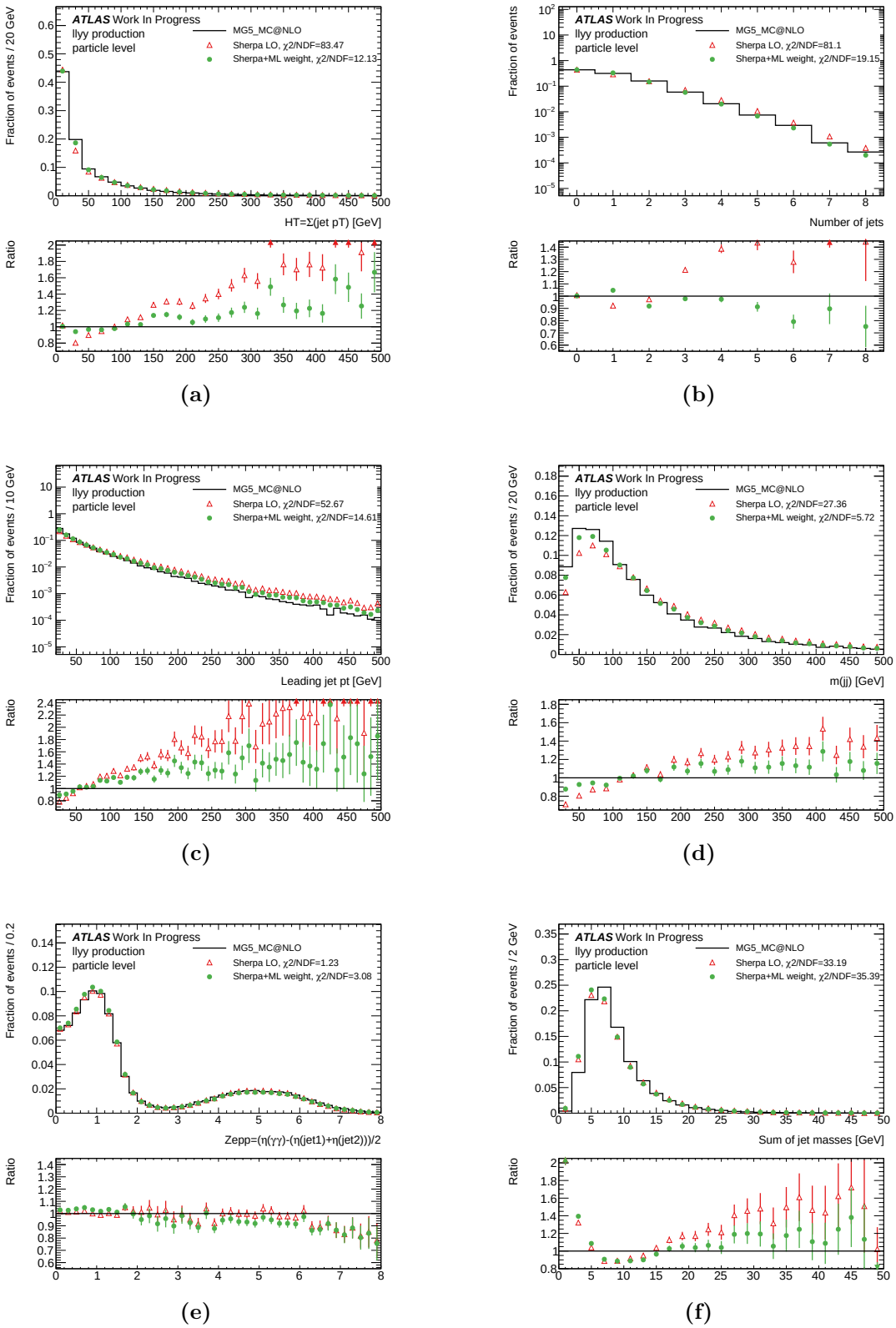

Figure 10.6 *Comparing the distributions of the CARL weighted and unweighted* Sherpa@LO $\ell\ell\gamma\gamma$ *events to* MadGraph_aMC@NLO *for the variables with the four greatest ((a)–(d)) and two least ((e)–(f)) $\Delta\chi^2/NDF$ improvement scores.*

A one dimensional reweighting was performed for the $\ell\ell\gamma\gamma$ samples. The variable selected for the reweighting was again the number of jets and the inclusive and exclusive $\Delta\chi^2/NDF$ improvement scores were calculated, as in the CARL study. The mean of the exclusive $\Delta\chi^2/NDF$ improvements for the traditional 1D reweighting of $\ell\ell\gamma\gamma$ events was evaluated to be **21.68**, compared to the multivariate reweighting improvement of 27.96. The inclusive $\Delta\chi^2/NDF$ improvement score mean was found to be **4.97**, compared to the multivariate reweighting improvement of 6.86. The higher improvement scores obtained with CARL multivariate reweighting demonstrates that this method is superior in remodelling the SHERPA@LO $\ell\nu\gamma\gamma$ sample to MADGRAPH_AMC@NLO.

10.3 Effects of $V\gamma\gamma$ Event Generator on Spurious Signal Estimates

The derived CARL weights were assigned to reconstruction level SHERPA@LO events using an event weight map to emulate a MADGRAPH_AMC@NLO sample, as described in Section 8.4. To assess the effect that using the emulated sample would have on modelling the background, the spurious signal test was performed on templates constructed from the CARL weighted and unweighted events in the relevant categories. The categories and their abbreviations are:

- `QQ2HLNU_PTV_0_75__0`: $qq' \to H\ell\nu$ ($0 < p_T^V \leq 75\,\text{GeV}$, High-purity),
- `QQ2HLNU_PTV_0_75__1`: $qq' \to H\ell\nu$ ($0 < p_T^V \leq 75\,\text{GeV}$, Med-purity),
- `QQ2HLNU_PTV_75_150__0`: $qq' \to H\ell\nu$ ($75 < p_T^V \leq 150\,\text{GeV}$, High-purity),
- `QQ2HLNU_PTV_75_150__1`: $qq' \to H\ell\nu$ ($75 < p_T^V \leq 150\,\text{GeV}$, Med-purity),
- `QQ2HLNU_PTV_150_250__0`: $qq' \to H\ell\nu$ ($150 < p_T^V \leq 250\,\text{GeV}$, High-purity),
- `QQ2HLNU_PTV_150_250__1`: $qq' \to H\ell\nu$ ($150 < p_T^V \leq 250\,\text{GeV}$, Med-purity),
- `QQ2HLNU_PTV_GT250__0`: $qq' \to H\ell\nu$ ($p_T^V \geq 250\,\text{GeV}$, High-purity),
- `QQ2HLNU_PTV_GT250__1`: $qq' \to H\ell\nu$ ($p_T^V \geq 250\,\text{GeV}$, Med-purity),
- `QQ2HLL_PTV_0_75__0`: $qq' \to H\ell\ell$ ($0 < p_T^V \leq 75\,\text{GeV}$, High-purity),
- `QQ2HLL_PTV_0_75__1`: $qq' \to H\ell\ell$ ($0 < p_T^V \leq 75\,\text{GeV}$, Med-purity),

- `QQ2HLL_PTV_75_150__0`: $qq' \to H\ell\ell$ ($75 < p_T^V \leq 150\,\text{GeV}$, High-purity),
- `QQ2HLL_PTV_75_150__1`: $qq' \to H\ell\ell$ ($75 < p_T^V \leq 150\,\text{GeV}$, Med-purity),
- `QQ2HLL_PTV_150_250__0`: $qq' \to H\ell\ell$ ($150 < p_T^V \leq 250\,\text{GeV}$, High-purity),
- `QQ2HLL_PTV_150_250__1`: $qq' \to H\ell\ell$ ($150 < p_T^V \leq 250\,\text{GeV}$, Med-purity),
- `QQ2HLL_PTV_GT250__0`: $qq' \to H\ell\ell$ ($p_T^V \geq 250\,\text{GeV}$).

To obtain the signal shapes and expected signal yields for the spurious signal test, DSCB functions were fitted to the simulated $m_{\gamma\gamma}$ distributions from WH, $q\bar{q} \to ZH$, and $gg \to ZH$ events populating the relevant categories. All of these fits were performed in a range of $110 < m_{\gamma\gamma} < 140\,\text{GeV}$ and normalised to $139\,\text{fb}^{-1}$.

An example of a constructed background template for the CARL weighted and unweighted Sherpa@LO templates is shown alongside the fitted signal model in Figure 10.7 for the `QQ2HLL_PTV_0_75__1` category. In Figure 10.7a, it is shown that MadGraph_aMC@NLO $V\gamma\gamma$ events predict a less steeply falling $m_{\gamma\gamma}$ background distribution.

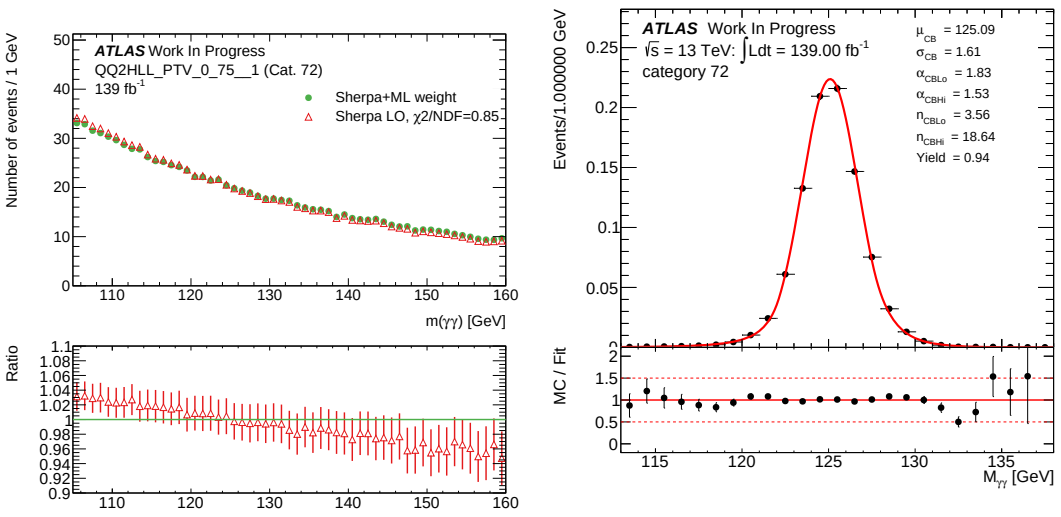

(a) *Background template.* **(b)** *Signal model.*

Figure 10.7 *The background template and fitted signal model constructed from CARL weighted and unweighted Sherpa@LO $V\gamma\gamma$ events for the $qq' \to H\ell\ell$ ($0 < p_T^V \leq 75\,\text{GeV}$, Med-purity) $H \to \gamma\gamma$ analysis category.*

The spurious signal test was performed as described in Section 6.5.3 and the results in each of the relevant categories are presented in the rest of this

section. For these results, QQ2HLNU_PTV_150_250__0, QQ2HLNU_PTV_GT250__0, and QQ2HLL_PTV_75_150__0 could not be fitted due to low statistics and were merged with their lower purity categories.

10.3.1 Fit Results for Free Selection of Functional Form

The selected analytical forms from Table 6.3 for background templates constructed with unweighted and CARL weighted SHERPA@LO events are presented in Table 10.4, alongside the fitted spurious signal yields. The QQ2HLNU_PTV_0_75__0 and QQ2HLL_PTV_GT250__0 category templates failed the spurious signal test for all functional forms and are shown with blank entries. The change in the number of parameters characterising the selected functional form and the relative change in the spurious signal yield proportional to the average yields over both fits, $|S_{\text{spur}}^{\text{CARL}}| / \left\langle |S_{\text{spur}}^{\text{both}}| \right\rangle$, are also shown where

$$\left\langle |S_{\text{spur}}^{\text{both}}| \right\rangle = \frac{1}{2}(|S_{\text{spur}}^{\text{no weights}}| + |S_{\text{spur}}^{\text{CARL}}|), \tag{10.2}$$

$|S_{\text{spur}}^{\text{no weights}}|$ is the spurious signal yield from the unweighted background template, and $|S_{\text{spur}}^{\text{CARL}}|$ is the yield from the CARL weighted template. A value of $|S_{\text{spur}}^{\text{CARL}}| / \left\langle |S_{\text{spur}}^{\text{both}}| \right\rangle = 1$ would be obtained in the case of no difference between the unweighted and weighted spurious signal yields.

Table 10.4 *The results of the spurious signal test for background templates constructed with unweighted and CARL weighted SHERPA@LO events.*

Category	Sherpa@LO			CARL Weighted Sherpa@LO (Emulating MadGraph_aMC@NLO)			Comparison	
	Function	N_{pars}	$\lvert S_{\text{spur}}\rvert$	Function	N_{pars}	$\lvert S_{\text{spur}}\rvert$	$\lvert S_{\text{spur}}^{\text{CARL}}\rvert / \left\langle \lvert S_{\text{spur}}^{\text{both}}\rvert \right\rangle$	ΔN_{pars}
QQ2HLNU_PTV_0_75__0	–	–	–	–	–	–	–	–
QQ2HLNU_PTV_0_75__1	PowerLaw	1	0.86	PowerLaw	1	1.03	1.09	0
QQ2HLNU_PTV_75_150__0	Bern5	5	53.90	Bern3	3	265.00	1.66	-2
QQ2HLNU_PTV_75_150__1	PowerLaw	1	1.30	Exp	1	1.42	1.04	0
QQ2HLNU_PTV_150_250__0+1	PowerLaw	1	204.00	Exp	1	0.42	0.00	0
QQ2HLNU_PTV_GT250__0+1	Bern5	5	0.72	Bern3	3	0.44	0.76	-2
QQ2HLL_PTV_0_75__0	PowerLaw2	3	965.00	PowerLaw	1	387.00	0.57	-2
QQ2HLL_PTV_0_75__1	ExpPoly2	2	3.18	ExpPoly2	2	3.80	1.09	0
QQ2HLL_PTV_75_150__0+1	ExpPoly3	3	0.66	PowerLaw2	3	0.30	0.63	0
QQ2HLL_PTV_150_250__0	ExpPoly2	2	326.00	ExpPoly3	3	418.00	1.12	1
QQ2HLL_PTV_150_250__1	Bern4	4	1.09	Bern3	3	1.01	0.96	-1
QQ2HLL_PTV_GT250__0	–	–	–	–	–	–	–	–

Taking the mean over all categories, the relative change in the spurious signal yield is $|S_{\text{spur}}^{\text{CARL}}| / \left\langle |S_{\text{spur}}^{\text{both}}| \right\rangle = 0.89 \pm 0.44$. Additionally it is noted that the CARL weighted templates emulating the effects of MADGRAPH_AMC@NLO generated $V\gamma\gamma$ events select a lower order functional form. A lower order form

was chosen for four cases out of 10, while the same order was chosen for five categories.

10.3.2 Fit Results for Forced Exponential Form

Table 10.5 *The results of the spurious signal test considering only an exponential form fit for background templates constructed with unweighted and CARL weighted* Sherpa@LO *events.*

Category	Sherpa@LO	CARL Weighted Sherpa@LO (Emulating MadGraph_aMC@NLO)	Comparison
	$\lvert S_{\text{spur}}\rvert$	$\lvert S_{\text{spur}}\rvert$	$\lvert S_{\text{spur}}^{\text{CARL}}\rvert / \left\langle \lvert S_{\text{spur}}^{\text{both}}\rvert \right\rangle$
QQ2HLNU_PTV_0_75__0	0.79	184.00	1.99
QQ2HLNU_PTV_0_75__1	2.51	2.57	1.01
QQ2HLNU_PTV_75_150__0	336.00	702.00	1.35
QQ2HLNU_PTV_75_150__1	1.58	1.42	0.95
QQ2HLNU_PTV_150_250__0+1	410.00	0.42	0.00
QQ2HLNU_PTV_GT250__0+1	353.00	772.00	1.37
QQ2HLL_PTV_0_75__0	635.00	797.00	1.11
QQ2HLL_PTV_0_75__1	7.49	7.84	1.02
QQ2HLL_PTV_75_150__0+1	97.90	330.00	1.54
QQ2HLL_PTV_150_250__0	974.00	572.00	0.74
QQ2HLL_PTV_150_250__1	1.49	1.43	0.98
QQ2HLL_PTV_GT250__0	855.00	861.00	1.00

To evaluate results for the categories for which the spurious signal test failed, and to obtain a more objective comparison of the changes in spurious signal yield, the tests were run again but where only an exponential functional form was considered. These results are shown in Table 10.5.

Taking the mean over all categories, the relative change in the spurious signal yield is $|S_{\text{spur}}^{\text{CARL}}| / \left\langle |S_{\text{spur}}^{\text{both}}| \right\rangle = 1.09 \pm 0.48$.

10.3.3 Implications of Results

The impact of modelling the $V\gamma\gamma$ background with MadGraph_aMC@NLO rather than Sherpa@LO is of particular interest since the former is expected to provide a better description of the data. However, Figure 10.8 shows that the differences between the two generators is small in comparison with current data discrepancies. The background composition for VH processes is uncertain, as evident from the 0-jet bin discrepancy in Figure 10.8a, and whilst this is the case neither generator can be excluded.

It is found that the generators differ in several important distributions for $H \to \gamma\gamma$ measurements of the VH production process, such as the N_j distribution

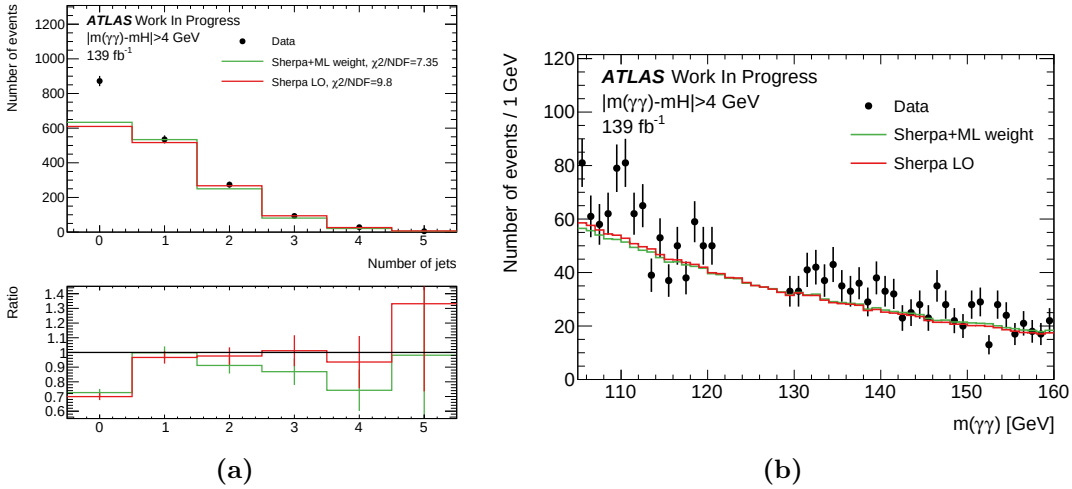

(a) **(b)**

Figure 10.8 *Comparing CARL weighted* Sherpa@LO *(emulating* MadGraph_aMC@NLO*) generated $V\gamma\gamma$ event distributions in N_j and $m_{\gamma\gamma}$ to those for unweighted Monte Carlo events and data.*

and variables used in the classification and background rejection BDTs. This indicates that the $V\gamma\gamma$ generator modelling uncertainties should be considered when constructing the classification and background rejection networks, if they are to perform optimally.

In the VH categories, MadGraph_aMC@NLO predicts a less steeply falling $m_{\gamma\gamma}$ distribution compared to Sherpa@LO, as shown in Figure 10.7a. However, the spurious signal test is found to be robust to this change, demonstrating that the spurious signal yields obtained for samples emulating MadGraph_aMC@NLO are consistent with Sherpa@LO samples within one standard deviation. Therefore, no spurious signal uncertainty due to the difference between MadGraph_aMC@NLO and Sherpa@LO is required in addition to that in current measurements of the $H \to \gamma\gamma$ channel.

In this chapter, it was described how to use the CARL reweighting technique from Chapter 8 to emulate a MadGraph_aMC@NLO generated sample of $\ell\nu\gamma\gamma$ and $\ell\ell\gamma\gamma$ background events using a Sherpa@LO sample. This reweighting method was shown to be superior to a traditional reweighting in one dimension for these samples. Assigning CARL weights to Sherpa@LO events at the reconstruction level showed that the difference in generators is not large when compared to the discrepancy between data and the simulated background templates, and the effects on the spurious signal yield are consistent with current systematic uncertainties. However, a number of key variables display large divergences

between the generators, highlighting the need to consider the $V\gamma\gamma$ generator modelling uncertainty when constructing classification and background rejection networks in the $H \to \gamma\gamma$ analysis. This research is the last study to be presented, and Chapter 11 will conclude the thesis.

References

[69] The ATLAS Collaboration. 'Measurement of the cross-section for electroweak production of dijets in association with a Z boson in pp collisions at $\sqrt{s} = 13$ TeV with the ATLAS detector'. In: *Physics Letters B* 775 (Dec. 2017), pp. 206–228. ISSN: 0370-2693. DOI: 10.1016/j.physletb.2017.10.040.

Chapter 11

Conclusions and Outlook

Exploration of Higgs boson to diphoton decays is still proving to be an exceptionally powerful channel for improving measurements of the Standard Model parameters at ATLAS. A measurement of the production cross-section multiplied by the branching ratio was presented and found to be $(\sigma \times B_{\gamma\gamma})_{\text{obs}} = 127 \pm 10$ fb. The importance of the systematic uncertainties on this measurement were highlighted, and emphasis was placed on understanding and reducing them.

The measurement dependence on the construction of physics model representations from simulated events was accentuated, and the endeavour to maintain the statistical significance of these Monte Carlo samples has been explained. The upgrade of FastCaloSim was illustrated, highlighting a new feature to emulate complex detector geometry features in the LAr calorimeters without sacrificing simulation speed. FastCaloSim is critical in producing the increasing sizes of simulated samples that ATLAS will require for future high luminosity datasets.

A method for determining the effects of statistical fluctuations in simulated event distributions on results of the spurious signal test was described. This method was used to determine the number of simulated $\gamma\gamma$ background events that would be required to adequately model the background shape in $H \to \gamma\gamma$ measurement categories. It was concluded that the background sample used in a legacy analysis required an increase by a factor of 7.20 to pass the spurious signal test in the current analysis iteration for all categories with a 95 % confidence level. Apropos of this result, the allocation of resources for the production of an additional 0.5 billion $\gamma\gamma$ events was granted to the analysis group, substantially reducing the measurement uncertainty. The described method could be taken

further to evaluate other effects than sample size on the background modelling uncertainty. For instance, by investigating the impact the photon energy resolution systematic uncertainty has on the shape of background templates, one could obtain information on how the spurious signal result varies.

A technique for the multivariate CARL reweighting of samples produced by different generators was presented, which allowed for the emulation of variant generator settings without requiring dedicated simulation samples to evaluate the effects on the measurement. The technique was applied to determine the ramifications of using a 5-flavour scheme in place of the nominal 4-flavour scheme for generating $tHqb$ signal events. The knowledge of this generator variation uncertainty improves the reliability of estimating the $tHqb$ production cross-section.

The CARL reweighting technique was subsequently implemented to ascertain the impact of using MadGraph_aMC@NLO in place of the nominal Sherpa@LO generator when producing background $V\gamma\gamma$ events. The CARL weights were propagated to the reconstruction level to create templates in the relevant categories and to retrieve estimates of the spurious signal yield to determine the effects on the background modelling uncertainty. Across all relevant categories, the generator variation was shown to differ by levels consistent with the current background modelling uncertainty. Several key variables for the event classification and background rejection exhibit large differences between Sherpa@LO and MadGraph_aMC@NLO. This indicates that the $V\gamma\gamma$ generator modelling uncertainties should be considered when constructing the classification and background rejection networks, if they are to perform optimally.

List of Figures

List of Tables

Bibliography

[1] The ATLAS Collaboration. 'Observation of a new particle in the search for the Standard Model Higgs boson with the ATLAS detector at the LHC'. In: *Physics Letters B* 716.1 (Nov. 2012), pp. 1–29. ISSN: 0370-2693. DOI: 10.1016/j.physletb.2012.08.020.

[2] The CMS Collaboration. 'Observation of a new boson at a mass of 125 GeV with the CMS experiment at the LHC'. In: *Physics Letters B* 716.1 (Sept. 2012), pp. 30–61. ISSN: 0370-2693. DOI: 10.1016/j.physletb.2012.08.021.

[3] F. Englert and R. Brout. 'Broken Symmetry and the Mass of Gauge Vector Mesons'. In: *Phys. Rev. Lett.* 13 (9 Aug. 1964), pp. 321–323. DOI: 10.1103/PhysRevLett.13.321.

[4] Peter W. Higgs. 'Broken Symmetries and the Masses of Gauge Bosons'. In: *Phys. Rev. Lett.* 13 (16 Oct. 1964), pp. 508–509. DOI: 10.1103/PhysRevLett.13.508.

[5] G. S. Guralnik, C. R. Hagen and T. W. B. Kibble. 'Global Conservation Laws and Massless Particles'. In: *Phys. Rev. Lett.* 13 (20 Nov. 1964), pp. 585–587. DOI: 10.1103/PhysRevLett.13.585.

[6] D. de Florian et al. *Handbook of LHC Higgs Cross Sections: 4. Deciphering the Nature of the Higgs Sector*. CERN Yellow Reports: Monographs CERN-2017-002-M. Oct. 2016. DOI: 10.23731/CYRM-2017-002.

[7] The ATLAS Collaboration. *Observation of $H \to b\bar{b}$ decays and VH production with the ATLAS detector*. Tech. rep. ATLAS-CONF-2018-036. Geneva: CERN, July 2018. URL: https://cds.cern.ch/record/2630338.

[8] The ATLAS Collaboration. 'Combined measurements of Higgs boson production and decay using up to 80 fb^{-1} of proton-proton collision data at $\sqrt{s} = 13$ TeV collected with the ATLAS experiment'. In: *Phys. Rev. D* 101.arXiv:1909.02845 (Sept. 2019), 012002. 48 p. DOI: 10.1103/PhysRevD.101.012002.

[9] The ATLAS Collaboration. 'Observation of Higgs boson production in association with a top quark pair at the LHC with the ATLAS detector'. In: *Phys. Lett. B* 784.arXiv:1806.00425 (June 2018), 173–191. 19 p. DOI: 10.1016/j.physletb.2018.07.035.

[10] Sarah Fields and Lexi Carver. 'Analyzing the LHC Magnet Quenches'. In: *Multiphysics Simulation: An IEEE Spectrum Insert 2017* (Oct. 2017), pp. 6–9.

[11] Oliver Sim Brüning et al. *LHC Design Report*. CERN Yellow Reports: Monographs. Geneva: CERN, 2004. DOI: 10.5170/CERN-2004-003-V-1.

[12] The ATLAS Collaboration et al. 'The ATLAS Experiment at the CERN Large Hadron Collider'. In: *JINST* 3 (2008). Also published by CERN Geneva in 2010, S08003. 437 p. DOI: 10.1088/1748-0221/3/08/S08003.

[13] The ALICE Collaboration. 'The ALICE experiment at the CERN LHC. A Large Ion Collider Experiment'. In: *JINST* 3 (2008), S08002. DOI: 10.1088/1748-0221/3/08/S08002.

[14] The LHCb Collaboration. 'The LHCb Detector at the LHC'. In: *JINST* 3.LHCb-DP-2008-001 (2008), S08005. DOI: 10.1088/1748-0221/3/08/S08005.

[15] The CMS Collaboration. 'The CMS experiment at the CERN LHC. The Compact Muon Solenoid experiment'. In: *JINST* 3 (2008), S08004. DOI: 10.1088/1748-0221/3/08/S08004.

[16] STFC. *CERN Accelerator Complex*. 2016. URL: https://stfc.ukri.org/research/particle-physics-and-particle-astrophysics/large-hadron-collider/cern-accelerator-complex/ (visited on 29/11/2019).

[17] J. Wenninger. 'LHC status and performance'. In: *PoS(CHARGED2018)001* 339 (Feb. 2019). DOI: 10.22323/1.339.0001.

[18] The ATLAS Collaboration. *LuminosityPublicResultsRun2*. 2019. URL: https://twiki.cern.ch/twiki/bin/view/AtlasPublic/LuminosityPublicResultsRun2 (visited on 04/12/2019).

[19] Izaak Neutelings. *TikZ.net - CMS coordinate system*. June 2017. URL: https://tikz.net/axis3d_cms/ (visited on 04/12/2021).

[20] Laurent Chevalier. 'Muon Detection'. In: ESIPAP 2015 - Module 1 - Physics of particle and astroparticle detectors (European Scientific Institute - Archamps, France). Feb. 2015. URL: https://indico.cern.ch/event/366272/contributions/1781565/.

[21] The ATLAS Collaboration. *Track Reconstruction Performance of the ATLAS Inner Detector at* $\sqrt{s} = 13$ *TeV*. Tech. rep. ATL-PHYS-PUB-2015-018. Geneva: CERN, July 2015. URL: https://cds.cern.ch/record/2037683.

[22] Christian Wolfgang Fabjan and F Gianotti. 'Calorimetry for Particle Physics'. In: *Rev. Mod. Phys.* 75.CERN-EP-2003-075 (Oct. 2003), 1243–1286. 96 p. URL: https://cds.cern.ch/record/692252.

[23] Heinrich J. Voelk and Konrad Bernloehr. 'Imaging Very High Energy Gamma-Ray Telescopes'. In: *Exper. Astron.* 25 (2009), pp. 173–191. DOI: 10.1007/s10686-009-9151-z. arXiv: 0812.4198 [astro-ph].

[24] CERN. *Worldwide LHC Computing Grid Tier Centres*. 2020. URL: https://wlcg-public.web.cern.ch/tier-centres (visited on 02/02/2020).

[25] Joao Pequenao and Paul Schaffner. 'A computer generated image representing how ATLAS detects particles'. Jan. 2013. URL: https://cds.cern.ch/record/1505342.

[26] Kyungeon Choi. *Tracking and Vertexing with the ATLAS Inner Detector in the LHC Run-2*. Tech. rep. ATL-PHYS-PROC-2017-075. Geneva: CERN, June 2017. DOI: 10.1007/978-981-13-1316-5_75.

[27] R Frühwirth. 'Application of Kalman filtering to track and vertex fitting'. In: *Nucl. Instrum. Methods Phys. Res., A* 262.HEPHY-PUB-503 (June 1987), 444. 19 p. URL: https://cds.cern.ch/record/178627.

[28] Federico Meloni. *Primary vertex reconstruction with the ATLAS detector*. Tech. rep. ATL-PHYS-PROC-2016-163. 12. Geneva: CERN, Oct. 2016. DOI: 10.1088/1748-0221/11/12/C12060.

[29] Sebastian Heer. *The secondary vertex finding algorithm with the ATLAS detector*. Tech. rep. ATL-PHYS-PROC-2017-195. Geneva: CERN, Oct. 2017. DOI: 10.22323/1.314.0762.

[30] The ATLAS Collaboration. *Electron and photon reconstruction and performance in ATLAS using a dynamical, topological cell clustering-based approach*. Tech. rep. ATL-PHYS-PUB-2017-022. Geneva: CERN, Dec. 2017. URL: https://cds.cern.ch/record/2298955.

[31] Matteo Cacciari, Gavin P Salam and Gregory Soyez. 'The anti-ktjet clustering algorithm'. In: *Journal of High Energy Physics* 2008.04 (Apr. 2008), pp. 063–063. DOI: 10.1088/1126-6708/2008/04/063.

[32] Steven Schramm. *ATLAS Jet Reconstruction, Calibration, and Tagging of Lorentz-boosted Objects*. Tech. rep. ATL-PHYS-PROC-2017-236. Geneva: CERN, Nov. 2017. URL: https://cds.cern.ch/record/2291608.

[33] The ATLAS Collaboration. 'Measurements of b-jet tagging efficiency with the ATLAS detector using $t\bar{t}$ events at $\sqrt{s} = 13$ TeV'. In: *JHEP* 08.arXiv:1805.01845 (May 2018), 089. 49 p. DOI: 10.1007/JHEP08(2018)089.

[34] The ATLAS Collaboration. 'Performance of missing transverse momentum reconstruction with the ATLAS detector using proton–proton collisions at $\sqrt{s} = 13$ TeV'. In: *The European Physical Journal C* 78.11 (Nov. 2018). ISSN: 1434-6052. DOI: 10.1140/epjc/s10052-018-6288-9.

[35] G Weidenspointner M G Pia. 'Monte Carlo Simulation for Particle Detectors'. In: *CERN Council Open Symposium on European Strategy for Particle Physics* (2012). arXiv: 1208.0047 [comp-ph].

[36] RL Harrison. 'Introduction to Monte Carlo Simulation'. In: *AIP Conference Proceedings* 1204 (2010), pp. 17–21.

[37] The ATLAS Collaboration. 'The ATLAS Simulation Infrastructure'. In: *European Physics Journal C* 70 (2010), pp. 823–874. arXiv: 1005.4568 [ins-det].

[38] Jana Schaarschmidt. *The new ATLAS Fast Calorimeter Simulation*. Tech. rep. ATL-SOFT-PROC-2017-005. Geneva: CERN, Jan. 2017. URL: https://cds.cern.ch/record/2240206.

[39] C Ay et al. 'Monte Carlo generators in ATLAS software'. In: *Journal of Physics: Conference Series* 219.3 (Apr. 2010), p. 032001. DOI: 10.1088/1742-6596/219/3/032001.

[40] Elmar Ritsch. 'ATLAS Detector Simulation in the Integrated Simulation Framework applied to the W Boson Mass Measurement'. Presented 27 Feb 2015. Dec. 2014. URL: https://cds.cern.ch/record/2221649.

[41] ATLAS Collaboration et al. *The simulation principle and performance of the ATLAS fast calorimeter simulation FastCaloSim*. Tech. rep. ATL-PHYS-PUB-2010-013. Geneva: CERN, Oct. 2010. URL: https://cds.cern.ch/record/1300517.

[42] The Geant4 Collaboration. 'Geant4 – a simulation toolkit'. In: *Nuclear Instruments and Methods in Physics Research Section A: Accelerators, Spectrometers, Detectors and Associated Equipment* 506.3 (2003), pp. 250–303. ISSN: 0168-9002. DOI: 10.1016/S0168-9002(03)01368-8.

[43] The Geant4 Collaboration. *Geant4: A Simulation Toolkit*. 2020. URL: https://www.geant4.org/geant4/ (visited on 17/04/2020).

[44] K Edmonds et al. *The Fast ATLAS Track Simulation (FATRAS)*. Tech. rep. ATL-SOFT-PUB-2008-001. ATL-COM-SOFT-2008-002. Geneva: CERN, Mar. 2008. URL: https://cds.cern.ch/record/1091969.

[45] A Salzburger, S Todorova and M Wolter. *The ATLAS Tracking Geometry Description*. Tech. rep. ATL-SOFT-PUB-2007-004. ATL-COM-SOFT-2007-009. Geneva: CERN, June 2007. URL: https://cds.cern.ch/record/1038098.

[46] Hasib Ahmed. 'Fast Simulation in ATLAS'. WorkShop on Efficient Computing for High Energy Physics. 2020. URL: https://indico.ph.ed.ac.uk/event/66/contributions/826/.

[47] The ATLAS Collaboration. *Performance of the Fast ATLAS Tracking Simulation (FATRAS) and the ATLAS Fast Calorimeter Simulation (FastCaloSim) with single particles*. Tech. rep. ATL-SOFT-PUB-2014-001. Geneva: CERN, Mar. 2014. URL: https://cds.cern.ch/record/1669341.

[48] The ATLAS Collaboration. *AtlFast3: the next generation of fast simulation in ATLAS*. Tech. rep. CERN-EP-2021-174. Geneva: CERN, Sept. 2021. URL: http://cds.cern.ch/record/2780174.

[49] Ian Jolliffe. 'Principal Component Analysis'. In: *International Encyclopedia of Statistical Science*. Ed. by Miodrag Lovric. Berlin, Heidelberg: Springer Berlin Heidelberg, 2011, pp. 1094–1096. ISBN: 978-3-642-04898-2. DOI: 10.1007/978-3-642-04898-2_455.

[50] Flavia Dias. *The new ATLAS Fast Calorimeter Simulation*. Tech. rep. ATL-SOFT-PROC-2016-008. Geneva: CERN, Oct. 2016. URL: https://cds.cern.ch/record/2228659.

[51] The ATLAS Collaboration. *ATLAS calorimeter performance: Technical Design Report*. Technical design report. ATLAS. Geneva: CERN, 1996. URL: https://cds.cern.ch/record/331059.

[52] Douglas C. Montgomery and George C. Runger. *Applied Statistics and Probability for Engineers*. John Wiley and Sons, Inc., 2003, p. 104. ISBN: 978-0-471-20454-1.

[53] The ATLAS Collaboration. *Measurement of the properties of Higgs boson production at $\sqrt{s}$=13 TeV in the $H \to \gamma\gamma$ channel using 139 fb^{-1} of pp collision data with the ATLAS experiment*. Tech. rep. ATLAS-CONF-2020-026. Geneva: CERN, Aug. 2020. URL: https://cds.cern.ch/record/2725727.

[54] The ATLAS Collaboration. *Measurements of Higgs boson properties in the diphoton decay channel using 80 fb^{-1} of pp collision data at $\sqrt{s}$ = 13 TeV with the ATLAS detector*. Tech. rep. ATLAS-CONF-2018-028. Geneva: CERN, July 2018. URL: https://cds.cern.ch/record/2628771.

[55] The ATLAS Collaboration. *Measurements and interpretations of Higgs-boson fiducial cross sections in the diphoton decay channel using 139 fb^{-1} of pp collision data at $\sqrt{s}$ = 13 TeV with the ATLAS detector*. Tech. rep. ATLAS-CONF-2019-029. Geneva: CERN, July 2019. URL: https://cds.cern.ch/record/2682800.

[56] Rachel Jordan Hyneman. 'Measuring Higgs Boson Couplings, including to the Top Quark, in the Diphoton Decay Channel with Run 2 Data Collected by the ATLAS Detector'. Presented 04 Feb 2020. URL: https://cds.cern.ch/record/2712576.

[57] Leonora Vesterbacka and Stephen Jiggins. *CARL-Torch - GitHub*. 2020. URL: https://github.com/leonoravesterbacka/carl-torch (visited on 24/08/2021).

[58] Gilles Louppe, Kyle Cranmer and Juan Pavez. *carl: a likelihood-free inference toolbox*. Mar. 2016. URL: https://dx.doi.org/10.5281/zenodo.47798 (visited on 24/08/2021).

[59] Adam Paszke et al. 'PyTorch: An Imperative Style, High-Performance Deep Learning Library'. In: *Advances in Neural Information Processing Systems 32*. Ed. by H. Wallach et al. Curran Associates, Inc., 2019, pp. 8024–8035. URL: https://papers.neurips.cc/paper/9015-pytorch-an-imperative-style-high-performance-deep-learning-library.pdf.

[60] Kyle Cranmer, Juan Pavez and Gilles Louppe. *Approximating Likelihood Ratios with Calibrated Discriminative Classifiers*. 2016. arXiv: 1506.02169 [stat.AP].

[61] Lutz Roeder. *Netron - GitHub*. 2021. URL: https://github.com/lutzroeder/netron (visited on 06/08/2021).

[62] Vinod Nair and Geoffrey E. Hinton. 'Rectified Linear Units Improve Restricted Boltzmann Machines'. In: ICML'10. Haifa, Israel: Omnipress, 2010, pp. 807–814. ISBN: 9781605589077.

[63] Jun Han and Claudio Moraga. 'The Influence of the Sigmoid Function Parameters on the Speed of Backpropagation Learning'. In: *Proceedings of the International Workshop on Artificial Neural Networks: From Natural to Artificial Neural Computation*. IWANN '96. Berlin, Heidelberg: Springer-Verlag, 1995, pp. 195–201. ISBN: 3540594973.

[64] Shie Mannor, Dori Peleg and Reuven Rubinstein. 'The Cross Entropy Method for Classification'. In: *Proceedings of the 22nd International Conference on Machine Learning*. ICML '05. Bonn, Germany: Association for Computing Machinery, 2005, pp. 561–568. ISBN: 1595931805. DOI: 10.1145/1102351.1102422.

[65] Sashank J. Reddi, Satyen Kale and Sanjiv Kumar. 'On the Convergence of Adam and Beyond'. In: *International Conference on Learning Representations*. 2018. URL: https://openreview.net/forum?id=ryQu7f-RZ.

[66] I.M. Chakravarti, R.G. Laha and J. Roy. *Handbook of Methods of Applied Statistics*. Handbook of Methods of Applied Statistics Vol. 1. John Wiley and Sons, 1967, pp. 392–394. URL: https://books.google.co.uk/books?id=IdI-AAAAIAAJ.

[67] Michael L. Meistrell. 'Evaluation of neural network performance by receiver operating characteristic (ROC) analysis: examples from the biotechnology domain'. In: *Computer Methods and Programs in Biomedicine* 32.1 (1990), pp. 73–80. ISSN: 0169-2607. DOI: 10.1016/0169-2607(90)90087-P.

[68] Frank Krauss and Davide Napoletano. 'Towards a fully massive five-flavor scheme'. In: *Phys. Rev. D* 98.9 (2018), p. 096002. DOI: 10.1103/PhysRevD.98.096002. arXiv: 1712.06832 [hep-ph].

[69] The ATLAS Collaboration. 'Measurement of the cross-section for electroweak production of dijets in association with a Z boson in pp collisions at $\sqrt{s} = 13$ TeV with the ATLAS detector'. In: *Physics Letters B* 775 (Dec. 2017), pp. 206–228. ISSN: 0370-2693. DOI: 10.1016/j.physletb.2017.10.040.